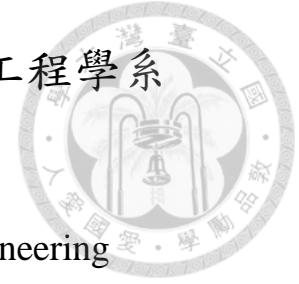國立臺灣大學生農學院生物產業機電工程學系

碩士論文

Department of Bio-Industrial Mechatronics Engineering

College of Bioresources and Agriculture

National Taiwan University

Master Thesis

對稱電極與指叉狀晶片電化學阻抗模型建立與適體感測應用

Electrochemical Impedance Modeling of Symmetric Electrodes and Interdigitated Array Chips for Aptasensing Applications

賴知佑

Chih-Yu Lai

指導教授：陳林祈 博士

Advisor: Lin-Chi Chen, Ph.D.

中華民國 108 年 7 月

July 2019

誌謝

時光飛逝，遙想大三進實驗室，曾對眼前一片迷茫的我，轉眼間四年已過，將面對下一段挑戰。研究如人生，這段路途時而艱辛、時而喜悅，如此珍貴的經歷無以言喻，於回憶的畫本上描繪雋永的色澤。

感謝陳林祈老師多年來的教導，除了許多的想法與建議，還提供我空間得以發展許多感興趣的研究，讓我有自信拓展不同的領域，更鼓勵我參與許多國內外研討會，讓我體會學術界的深廣並開拓我的視野。感謝陳倩瑜老師於升大三至大三時在生醫資訊方面和機器學習方面技能的增長，還有在相關競賽上學長們的協助。感謝侯詠德老師於大二下教授生化概論以及給我的肯定，帶領我踏入一個全新的領域。感謝口試委員何國川老師、周家復老師、鄭宗記老師及魏培坤老師撥冗參與碩論口試，肯定我的研究以及給予多方面的建議，感謝數不清引導我至今的師長。

感謝噹噹帶領我做許多實驗與製程技術，每當有疑問時總是能一起討論個水落石出。感謝登凱在生化技術上的指點與建議，總讓我感覺中研院比想像中還更熟悉！感謝誠專、Ella、珮瑋、修瑋、靜容、婉茹、裕夫、奇翰、伊敏、柔宣、禮丞、惟甄、唯里、聖丰及亭萱所有學術上的支持與研究上的鼓勵，帶給我多采多姿的實驗室生活。感謝實驗室每一位學長姐與學弟妹，給予403實驗室豐富歡樂的氣氛。

我想要特別感謝我的家人與惟甄，在風雨交加的夜晚，你們帶給我希望與關懷，讓我知道我並不孤單，且世上是有如此溫暖與美好。尚未到這趟旅程的終點，我將攜帶滿滿回憶前往下一站，期望能將所獲所學啟發無數殷勤弟子，奉獻予公益、回饋予社會。

i

摘要

　　腫瘤標誌之偵測與抑制成為近年癌症預防及治療的新趨勢，此類標誌常利用操作簡易及低成本之電化學阻抗頻譜法(electrochemical impedance spectroscopy，簡稱 EIS)、配合靈敏度及專一性高的適體感測(aptasensing)技術進行量測，於近年之生物分析應用蓬勃發展。然而三極式電化學系統之微小化面臨設計與製程複雜、高成本與低製作良率等問題，且近年廣泛應用於電化學感測技術之二極式指叉狀電極(interdigitated array electrodes，簡稱 IDA electrodes)因幾何特性複雜，尚未有根據其帶寬(bandwidth)與間距(gap width)推導其擴散阻抗(diffusion impedance)之文獻。因此本論文以對稱二極式阻抗感測模型之建立為主軸，推導不同幾何之指叉狀電極擴散阻抗公式，發展對稱二極式電極等效電路模型並進行阻抗式適體感測，主要以兩個部分進行探討並分述如下：第一部分著重於指叉狀電極擴散阻抗的理論推導與驗證。利用共形變換(conformal mapping)及圓柱有限長度近似方法(cylindrical finite length approximation)推導不同幾何之指叉狀電極擴散阻抗積分型公式解，並且套用在現今之指叉狀電極電化學系統中。此部分之研究導出能夠針對不同電極帶寬、間距、擴散係數…等參數而直接計算出其擴散阻抗之理論公式，九種不同帶寬與間距之指叉狀電極利用微製程技術製作而成。時間相依(time-dependent)二維擴散之模擬結果證實理論中假想等濃度邊界的存在與理論之可行性，理論所計算之 0Hz 擴散阻抗與前人研究所推導之極限電流計算公式的倒數有高度線性相關($R^2 = 0.992$)，實驗所得極限電流倒數與計算之 0Hz 擴散阻抗具高度相關性($R^2 = 0.970$)，所推導的公式能夠精準預測其電化學阻抗頻譜量測結果($R^2 \geq 0.948$)，且已驗證可透過此理論進行等效電路匹配(equivalent circuit fitting)並成功預測其電極幾何。此部分可提供指叉狀電極於低頻量測區間阻抗變化之解釋，有助於相關領域之學者對於此種系統的擴散行為更進一步的認知與等效電路模型之建立。第二部分推導對稱二極式電極等效電路模型並利用標準金電極(standard Au electrode，簡稱 SGE)及
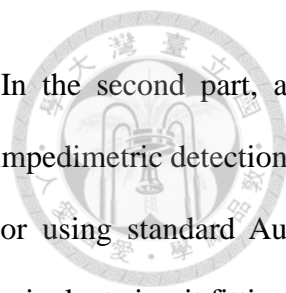
指叉狀電極驗證模型可行性與應用於凝血酶(thrombin)及腫瘤標誌 MUC1 之量測。若利用單一 Randles 電路進行對稱電極系統之等效電路匹配，則其參數 R_{ct} 與 R_s 會是實際值的兩倍、Q_0 與 Y_0 會是實際值的一半、且 n 會與實際值相同。此理論利用兩種不同幾何之對稱電極晶片進行驗證，應用於適體感測器之初步概念驗證利用凝血酶(thrombin)作為感測標的且 K_D 為 129.4nM。MUC1 與其硫醇基修飾過之 DNA 適體(5'SH-$(CH_2)_6$-S2.2)透過三極式適體感測器量測之 K_D 為 15.11nM，根據專一性結合模型計算之最大阻抗變化(B_{max})為 7.91kΩ，接著發現 MUC1 之對稱二極式適體感測器量測之 K_D 為 15.92nM 且 B_{max} 為 17.08kΩ，此兩組 K_D 結果相近，而 B_{max} 約為兩倍關係，與推導的模型所得到的結果一致，證明此理論模型應用於生物感測的正確性。利用指叉狀電極製作的凝血酶適體感測器，其電化學阻抗頻譜結果可利用第一部分根據理論所製作的等效電路匹配程式得到準確的參數，且此感測器具有可重複測量六次之再生性(regenerability)以及專一性(specificity)。對稱二極式金電極系統簡單、低成本與適體之高度穩定性極有助於商業化過程之大量生產與客製化。藉由上述之研究成果，期望在未來可利用指叉狀電極進行微小化發展並應用於相關醫療診斷，更甚能實現於個人化醫療與定點照護中。

關鍵字：指叉狀電極、電化學阻抗頻譜、有限擴散、對稱電極、適體感測

Abstract
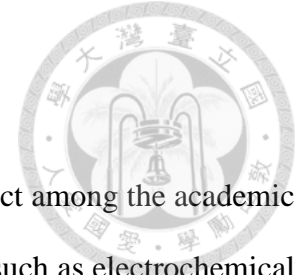
The inhibition of tumor markers has been a popular research object among the academic society. They are often detected using simple and low-cost techniques such as electrochemical impedance spectroscopy (EIS), which aptamers are occasionally used as the sensing element for achieving high sensitivity and selectivity. This integrated method has flourished in recent years. However, for electrochemical methods, a three electrode setup faces fabrication complexity, high cost and low yield rates during miniaturization. Two electrode impedimetric detection using interdigitated array (IDA) electrodes also faces a problem. Due to its geometry, there hasn't been any studies that derive its diffusion impedance according to different bandwidths and gap widths. Therefore, this study makes a basis on impedimetric modeling of symmetric two electrode systems. The first part focuses on the derivation and verification of an integral form of solution for IDA diffusion impedance. Conformal mapping and cylindrical finite length approximation methods are used in theory. Simulations are performed for confirming assumptions such as the imaginary constant concentration boundary (ICCB). Nine electrodes of different bandwidths and gap widths are fabricated with their heights and symmetric electrochemical characteristics verified. The calculated zero-frequency impedance showed high correlation with the reciprocal of limiting current calculated from previous studies ($R^2 = 0.992$) and from chronoamperometry experiments ($R^2 = 0.970$). Further evidence for the correctness of theory is established due to the fact that experimental EIS data and calculated impedances are highly consistent ($R^2 \geq 0.948$ for real and imaginary part). This sheds some light on explaining the phenomenon of diffusion impedance using IDA electrodes in the low frequency spectrum. An equivalent circuit fitting program succeeded to accurately fit the EIS data and parameters such as the ratio of electrode bandwidth to gap width and diffusion coefficient can also be obtained by fitting the data from a single EIS experiment. This can aid

researchers in relevant fields model their systems more accurately. In the second part, a symmetric equivalent circuit model is developed, and it is applied it for impedimetric detection of thrombin and a tumor marker MUC1 with a fabricated aptasensor using standard Au electrodes (SGE) and IDA chips. If a single Randles circuit is used for equivalent circuit fitting on a symmetric electrode system, R_{ct} and R_s would be double the real value, Q_0 and Y_0 would be half the real value, and n would be the same. This relationship is proven using experimental data from two kinds of micro-fabricated symmetric electrode chips. Thrombin is used for the proof of concept and a K_D of 129.4nM is obtained using the symmetric electrode setup. MUC1 is detected by the thiolated S2.2 aptamer using a three electrode setup and the K_D is 15.11nM. The calculated max binding value (B_{max}) according to one-site specific binding model is 7.91kΩ. Using a two electrode setup, the K_D is 15.92nM and the B_{max} is 17.08kΩ. The calculated K_D values for two and three electrode setups are consistent, and the ratio between B_{max} is about 2, which corresponds to the developed model. This proves the correctness of the model applied for bio-detection. IDA chips are used for aptasensor fabrication for thrombin detection. The program designed in the first part is used for circuit fitting of EIS data, and accurate parameters are obtained. This sensor has the regenerability for six times of detection and the specificity is also confirmed. Symmetric Au electrode systems have simple and low fabrication cost characteristics. Its integration with highly stable aptamers can contribute to mass production and customization in product commercialization. According to the above results, the author anticipates future developments in relevant medical diagnosis and point-of-care applications.
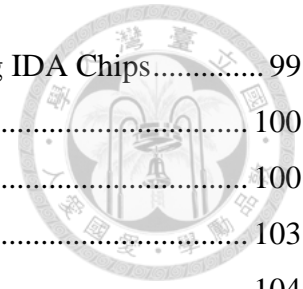

Keywords: interdigitated array (IDA) electrodes, electrochemical impedance spectroscopy (EIS), finite diffusion, symmetric electrodes, aptasensing
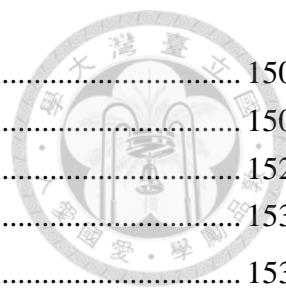
Table of Contents

List of Figures

List of Tables

Frequent Abbreviations

WE: working electrode

CE: counter electrode

RE: reference electrode

EIS: electrochemical impedance spectroscopy

CV: cyclic voltammetry

CA: chronoamperometry

IDA: interdigitated array

SER: series (used for explaining electrode geometry)

ICCB: imaginary constant concentration boundary

CPE: constant phase element

MSE: mean square error

SGE: standard Au electrode

RT: room temperature

DIW: deionized water

MCH: 6-mercaptohexanol

MUC1: mucin-1

BSA: bovine serum albumin

HSA: human serum albumin

LOD: limit of detection

Major Symbols

w_e: electrode bandwidth ([=] m)

w_g: the gap width between two band electrodes ([=] m)

w: unit cell width ($= w_e + w_g$)

N: total number of bands in an IDA electrode (dimensionless)

y_{ICCB}: corresponding point of x_e (a certain point on the electrode) on the ICCB ([=] m)

$L_d(x_e)$: diffusion length at a certain point (x_e) on the electrode ([=] m)

Y_0: proportional coefficient for diffusion impedance element ([=] $s^{1/2}/\Omega$)

R_{ct}: charge transfer resistance ([=] Ω)

R_s: solution resistance ([=] Ω)

C_{dl}: double layer capacitance ([=] F or s/Ω)

Q_{dl} (or Q_0): CPE for double layer capacitance ([=] s^n/Ω)

n: exponent for CPE (dimensionless) (※Not to be confused with number of electrons.)

Z_W: Warburg diffusion impedance ([=] Ω)

Z_I or $Z_{diff-IDA}$: IDA diffusion impedance ([=] Ω)

S: weighted sum of squares of error ([=] Ω) (※One of many definitions of S.)

E_{init}: initial voltage (DC voltage applied between WE and RE, [=] V)

K_D: dissociation constant ([=] M)

B_{max}: max change of R_{ct} caused by binding ([=] Ω)

Chapter 1 Introduction

1.1 Preface

A bio-detection system is involved with one or several detection techniques such as such as optical, electrochemical and mechanical detection methods and the correspondent equipment and material. Electrochemical techniques are advantageous compared with others within bio-detection methods due to its low-cost and easy-to-integrate features. There is also no need for complex signal transduction processes because the subsequent data acquisition unit after the sensing event can usually directly attain an electrical signal (A.J. Bard and Faulkner, 2000).

Electrochemical impedance spectroscopy (EIS) is a powerful electrochemical method for bio-analyte detection in affinity-based biosensors and can be integrated into miniaturized devices due to its label-free and sensitive characteristics (Daniels and Pourmand, 2007). This trait is attractive because electrodes can easily be fabricated into a miniaturized device which the sample usage can be lowered down to a few micro-liters. Among various electrode configurations, interdigitated array (IDA) electrodes are symmetric electrodes and have the advantages of enhanced sensitivity, increased active area and miniaturized sizes (Mazlan et al., 2017). They have been widely used in various applications (Yan et al., 2011). Their steady-state current and concentration behaviour

1

have been extensively researched using analytical and numerical approaches (Aoki et al., 1988).

Aptamers are artificially synthesized DNA or RNA that can be selected *in vitro*. This is another growing field of interest for the affinitive and selective tendency towards their target (Hianik and Wang, 2009). Their robustness allows them to survive harsh conditions and remain functional over an extended period of time (Y. C. Lim et al., 2010). This important feature can contribute to the bio-detection system, permitting them to be immobilized as sensing elements on a biosensor chip (aptasensors), packed up in miniaturized chips and delivered to remote regions. Researches on aptasensors using IDA electrode chips along with EIS bio-detection has recently gained high popularity due to several combined advantages (Arya et al., 2018; Ding et al., 2017; Zhurauski et al., 2018). These chips have a large potential in the development of portable, real-time, multiplex and smart device integrated sensing applications.

1.2 Research Motivation

Novel sensing architectures are presented frequently without having a strong and powerful enough model in accordance to their detection methods. This may lead to valuable resources being eventually abandoned due to the lack of ability for its interpretation.

Taking EIS detection of IDA electrodes for example, the periodic-steady-state diffusion impedance of IDA electrodes has never been tackled using an analytical approach. A Warburg element is still often used in equivalent circuit modeling of EIS data. However, it fails at low frequencies due to the arising steady-state current (Allen J. Bard et al., 1986; Niwa et al., 1990). In order to obtain a general method for interpreting EIS data using an IDA electrode, a model must be constructed to better evaluate the diffusion phenomenon exhibited. If that is achieved, then parameters such as w_g (gap width) or w_e (electrode bandwidth) can be accurately determined.

For miniaturization of electrochemical systems, symmetric electrode setups are often used due to its fabrication simplicity and high yield rate. The shape of EIS plots using these setups are known to be identical to a typical three electrode setup, and thus a single Randles circuit can be used for equivalent circuit fitting. However, to the best of the author's knowledge, there hasn't been any study that derives the relationship between

3

the parameters of the fitted data and the real parameters if a symmetric Randles circuit in series is used. In order to find the real parameters of a symmetric electrode setup using a single Randles circuit, a relationship must be established.
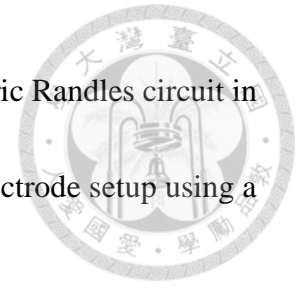
To sum up, the thesis is divided into two parts. The former part aims to develop a theory for finding a solution to model the diffusion impedance of IDA electrodes. The solution can be degraded for calculating the limiting current, and an equivalent circuit element is constructed for fitting the EIS data obtained. The latter part focuses on impedimetric aptasensing using symmetric electrodes. The parameter relationship between a single and symmetric Randles circuit is derived and verified, and is used in application for detection of thrombin and the tumor marker mucin-1 (MUC1).

4

1.3   Research Aims

This research is dedicated to modeling IDA and other symmetric electrodes which can for be applied for impedimetric aptasensing of proteins including tumor markers. For derivation of the diffusion impedance of IDA electrodes, not only can the theory help researchers fit their data and obtain parameters more accurately, but also assist them understand the underlying phenomenon more correctly. For relationship establishment of parameters between a single Randles circuit and symmetric electrode setups, it can simplify the fitting model used for characterization. For fabrication of impedimetric aptasensor, it has label-free and simple advantages, and can be monitored during each stage. The individual objectives for this thesis are listed as below:

1. Solution derivation for the diffusion impedance of IDA electrodes.

2. Equivalent circuit fitting using the IDA diffusion element.

3. Relationship establishment of Randles circuit parameters between three and symmetric electrode setups.

4. Impedimetric aptasensor fabrication using symmetric SGEs.

5. Fabrication of a regenerable and target specific impedimetric aptasensor using IDA electrodes.

1.4 Research Framework

This thesis consists of theoretical and applied stages. Due to incomplete fundamentals for impedimetric biosensors using symmetric electrodes, the derivations for the IDA diffusion impedance and the symmetric equivalent circuit analyzing method is carried out. Moreover, the IDA diffusion impedance is firsthand derived, and is used to make complete the theory of symmetric equivalent circuits, which derives the relationship of Randles circuit parameters between three and two symmetric electrode setups. The theory thereafter is applied for MUC1 detection using an impedimetric aptasensor made from symmetric electrodes. Parameters of two and three electrode setups for MUC1 detection are compared to verify the derived relationship, and specificity between the aptamer and target is also confirmed using a two electrode setup. At last, the two theories are used for analysis of an impedimetric aptasensor fabricated on IDA chips for thrombin detection. The whole framework is architected as in Figure 1-1.

6
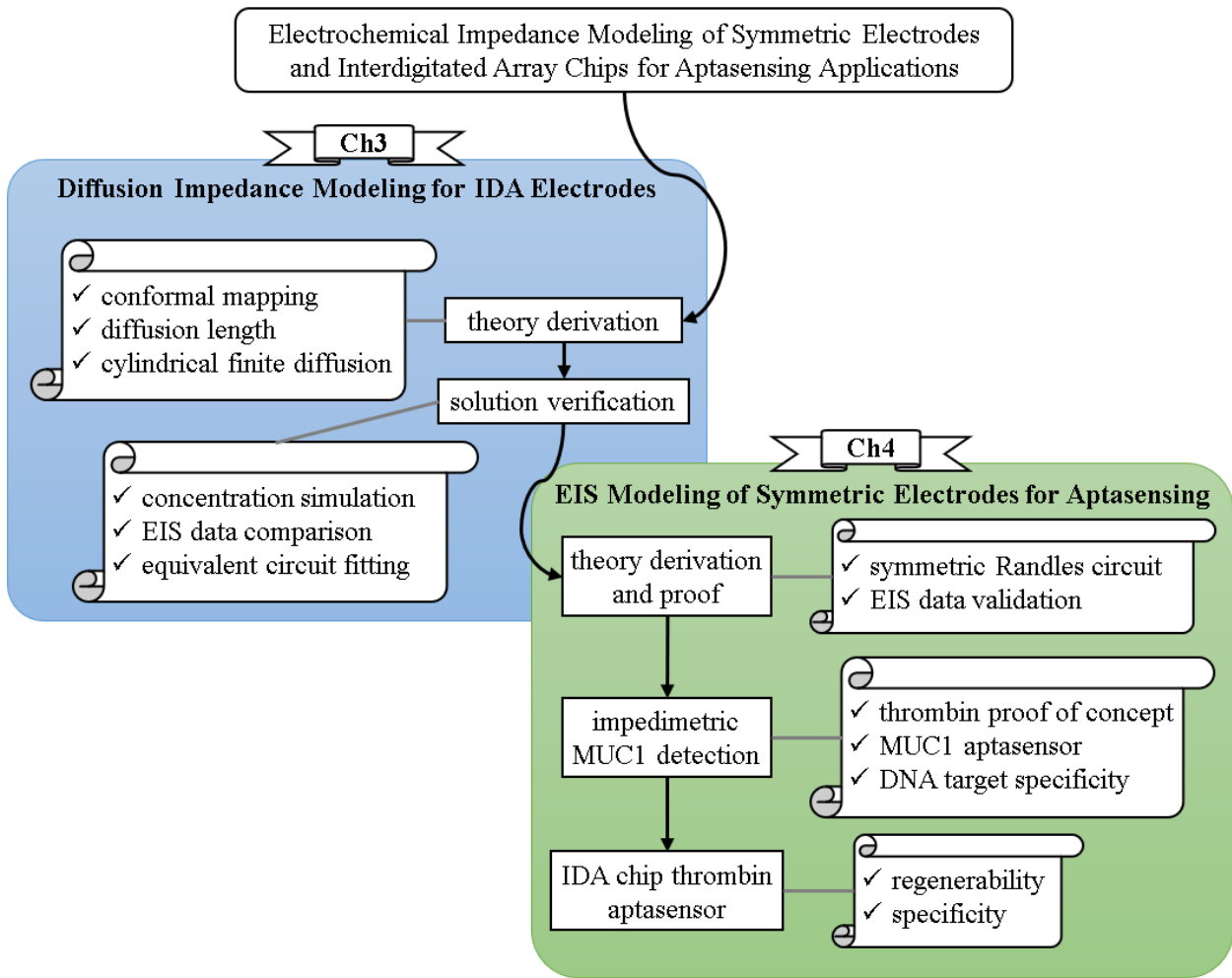
Figure 1-1 The research framework for this thesis.

Chapter 2 Literature Review

2.1 EIS in Affinity-Based Biosensors

Affinity-based biosensors are analytical devices which can characterize the interactions between a bio-analyte and its corresponding recognition element with the dissociation constant (K_D) serving as an important parameter for comparing the affinity strengths (Rogers, 2000). Electrochemical biosensors have been developed and studied for several decades and have prospered in a variety of different sensing methods (e.g. potentiometric (Ivnitskii and Rishpon, 1994; Marchenko et al., 2015), amperometric (Arslan et al., 2011; Romero et al., 2010), conductive (Chaubey and Malhotra, 2002)) and applications (Grieshaber et al., 2008; Thévenot et al., 2001). In the following section, electrochemical impedance spectroscopy (EIS) is briefly introduced and its applications in affinitive detection are discussed.

8

2.1.1 A Brief Introduction of EIS

The impedance of an electronic component is measured by applying a sinusoidal voltage wave across its two end points and measuring the resulting sinusoidal current wave. By complex analysis, the absolute impedance ($|Z|$) is calculated by dividing the amplitude of the voltage wave by that of the current and the phase angle (Φ) is calculated from the phase shift between the two waves. By changing the frequency (ω) of the applied voltage, the calculated absolute impedance and phase angle may also vary. A Bode plot can be drawn by plotting the absolute impedance or the phase angle with frequency. Still, a Nyquist plot can be drawn by calculating the real and imaginary part of impedance ($\text{Re}(Z)$ and $\text{Im}(Z)$) and plotting them onto a complex plane (Hambley, 2011).

Bode plots and Nyquist plots are essential for interpreting and analyzing bio-reactions using EIS. In affinity-based impedimetric biosensors, bio-recognition elements, which can be antibodies (Daniels and Pourmand, 2007), RNA (Y. C. Lim et al., 2010), DNA (Radi et al., 2005) … etc., are immobilized onto the electrode surface and can specifically react with the bio-analyte. Upon reaction, electrochemical impedimetric properties may change and can be successfully detected by EIS. Redox species (e.g. $Fe(CN)_6^{3-/4-}$) can be added to increase the faradaic current across the electrode surface to increase sensitivity, while there are other capacitive biosensors which measure only the non-faradaic current induced at the electrode surface.

9

2.1.2 EIS Applied in Affinity-Based Measurements

Impedimetric affinitive sensing methods including EIS are label-free, which means the sample doesn't need to undergo certain modifications for detection (Daniels and Pourmand, 2007). They are also non-destructive compared with other electrochemical techniques due to the small voltage amplitude applied on the electrochemical cell, while others including cyclic voltammetry (CV) or chronoamperometry (CA) may harm the electrode surface by significantly polarizing it (Groeber et al., 2015).

A method for K_D measurement using EIS is by immobilizing the recognition element onto an electrode surface and afterwards making it contact with different concentrations of the target analyte in a solution containing redox species (e.g. $Fe(CN)_6^{3-}$ $^{/4-}$). The charge transfer resistance (R_{ct}) will be affected by interactions between the recognition element and the analyte. Thus, by plotting the charge transfer resistance difference (ΔR_{ct}) to analyte concentration, the K_D value can be calculated using Langmuir isotherm binding models (Daniels and Pourmand, 2007).

The electrochemical setup of an EIS measurement is a direct influence to the equivalent circuit used in data fitting for obtaining component values including R_{ct} (Yuan et al., 2010). For the before-mentioned K_D measurement, a three electrode setup can be used to achieve accurate control of potential and the Randles circuit is typically

10

implemented as the equivalent circuit (Chesney, 1996). Usually, the control of potential over the working electrode (WE) isn't critical, so a two electrode setup can also be implemented in EIS by connecting the counter (CE) and reference (RE) electrode. In two electrode setups, a voltage across the WE and CE/RE is applied (Cho et al., 2009).

To sum up, applications of EIS in K_D measurement are simple, rapid, label-free, low-cost, non-destructive and sometimes even reusable (Radi et al., 2005), which is a very favorable subject regarding point-of-care needs (Rasooly, 2006; Rasooly and Jacobson, 2006; J. Wang, 2006).
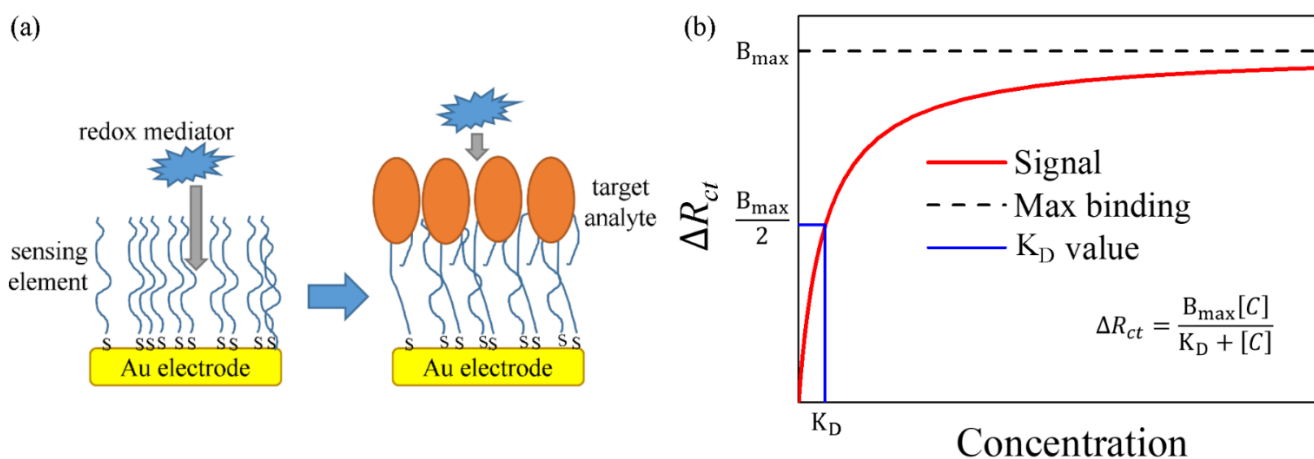
Figure 2-1 (a) Redox mediator (species) associated binding event and its (b) ΔR_{ct} vs concentration signal relationship on an Au electrode.

11

2.2 Impedimetric Biosensors using IDA Electrodes

2.2.1 A Brief Introduction of IDA Electrodes

Electrochemical devices using interdigitated array (IDA) electrodes are gaining wide interest and are being extensively studied in a variety of fields (Mazlan et al., 2017; Yan et al., 2011). These devices can be miniaturized on chips, have low fabrication costs, are simple to handle and have largely improved sensitivities (Barnes et al., 2012). In the past few decades, they have been applied in voltammetric (Y. Xu et al., 2016), amperometric (Weng et al., 2019), capacitive (L. Wang et al., 2017) and impedimetric (de la Rica et al., 2006; Valera et al., 2007) sensing methods.

An IDA electrode consists of a pair of electrode with numerous microarray bands interlocked (Barnes et al., 2012). Usually, each electrode band and the gap between then have the same width, making it symmetric. In electrochemical experiments using an IDA electrode, two electrode setups are often used by connecting the WE to one side and the CE/RE electrode to the other (Yan et al., 2011). In this configuration, the potential of the WE cannot be controlled easily and the CE/RE acts as a pseudo reference. This makes interpretation of CV data somehow more difficult than typical three-electrode setups. However, if equal concentration of both a certain pair of redox species is added, there might be a consequence that the standard potential of both electrodes are the same (Weng

12

et al., 2019). This is a particularly obvious advantage for impedance biosensors: There is no need to further add a voltage bias between the two electrodes. One only need to apply an oscillating small voltage at 0V bias to obtain impedance data and he or she can be sure that both the electrode potentials shift to exactly the standard potential of the reaction of the redox species.

IDA electrodes have been widely used for impedimetric bio-detection. The gap width has shown to have a significant effect on the sensitivity of these kinds of impedimetric biosensors. The smaller the width, the larger the impedimetric response (Y. Wang et al., 2012). Very low limit of detection have been also reported (Shoute et al., 2018). The concentration of the bio-analyte can shift the properties of the solution (e.g. the solution resistance (R_s) or the dielectric capacitance (C_{di})). They can also be bound to the sensing element immobilized on the electrode, varying R_{ct} or the double layer capacitance (C_{dl}) (Yan et al., 2011). They have also been integrated with different applications including microfluidic systems.

13

2.2.2 Issues in Low Frequency Domain
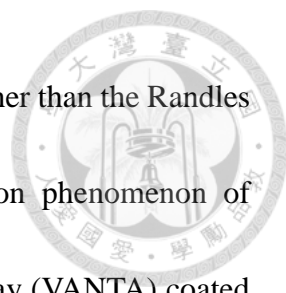
A problem of using IDA electrodes for impedimetric detection arises in the low frequency region. Due to its geometry, redox species finitely diffuse between two lateral electrode bands. The semi-infinite diffusion assumption used for common three-electrode systems is invalid and the Warburg element used for modeling of these systems would fail (Allen J. Bard et al., 1986; Niwa et al., 1990). Moreover, it is clear that a non-zero limiting current (or steady-state current) will exist in an IDA electrode system (Aoki et al., 1988). From the above reasons, it can be sure that as the frequency decreases, the imaginary part of impedance would also eventually approach zero. This would consequently result in a bending of impedance towards the real axis at low frequencies in a typical Nyquist plot (cf. section 3.1). Therefore, an element for calculating the diffusion impedance of IDA electrodes must be developed for modeling of such phenomenon. The appearance of this bending phenomenon at low frequencies can be found by simply performing EIS on a bare IDA electrode with both redox species present.

Unfortunately, there are barely any studies that directly confront this issue and propose an adequate or general solution. In order to find the exact value of diffusion impedance, 2D time-dependent partial differential equations are needed to be solved along with heterogeneous boundary conditions at the electrode surface (A.J. Bard and

14

Faulkner, 2000). This makes it almost impossible to find the exact solution. Even if the periodic-steady-state solution are to be derived, it could be expected that the function would become too complicated for practical implementation.
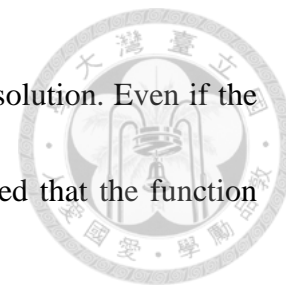
Several appearances resembling the finite diffusion phenomenon of IDA electrodes have occurred in previous published literatures. Lu et al. fabricated an IDA electrode olfactory biosensor for detecting interactions between odorant-binding proteins (OBPs) and different semiochemicals emitted from host plants (Lu et al., 2015). The impedance spectra of the bare electrode clearly exhibited the diffusion nature of an IDA electrode, which is, the decrease of phase angle at low frequencies (Figure 2-2e). However, when the electrode is immobilized, the R_{ct} became large and dominated over diffusion effects. In that way, the diffusion impedance could be neglected and it would make little difference whether or not to use a Warburg element. Chiriacò et al. developed a flow-injection impedimetric immunosensor using IDA electrodes for detection of cholera toxin (Chiriaco et al., 2011). Despite the large R_{ct}, down bending of impedances in their Nyquist plots (Figure 2-2b) can merely be seen. Zhurauski et al. developed an affimer-functionalized IDA electrode-based biosensor for detection of Her4, a protein tumor biomarker (Zhurauski et al., 2018). Though no bending of impedance can be seen in the Nyquist plot of their blank electrode, the phase angle is obviously lower than the typical

15

45° of Warburg elements (Figure 2-2c). Different kinds of circuits other than the Randles circuit are also used for explanation of the phase angle depletion phenomenon of impedances. Ding et al. grew vertically aligned carbon nanotube array (VANTA) coated IDA electrodes for detection of human cancerous inhibitor PP2A (CIP2A) (Ding et al., 2018). Their equivalent circuit consists of a geometric capacitance induced constant phase element (CPE) and R_{ct} in parallel, another CPE and R in parallel representing film and solution interface, and a R_s in series (Figure 2-2a). That interpretation for the film and solution interface is questioned because at low frequencies, the impedance for the CPE might become so large that the current only passes through R, making the CPE lose its effect. Another reason is that the shape of the imperfect semi-circle on the right of Fig. 4b and S2a in their work appears to be made up of something else caused by another phenomenon. Ohno et al. utilized IDA electrodes for immunosensing of human immunoglobulin A (IgA) (Ohno et al., 2013). They assumed that the organic layer formed on the IDA electrode can be divided into the interfacial and inner part. These two parts respectively result in one semi-circle composed of a parallel R_{ct} and C_{dl}, and another imperfect semi-circle composed of a parallel CPE and constant resistance (R_α) (Figure 2-2d). Wang et al. developed an IDA electrode based immunosensor for detection of avian influenza virus H5N1 (R. Wang et al., 2009). Their Nyquist diagram clearly showed down

16
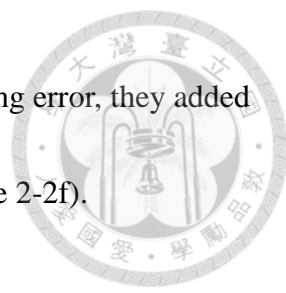
bending of impedances at low frequencies. For correction of the fitting error, they added

another capacitor and resistor in parallel to the original model (Figure 2-2f).
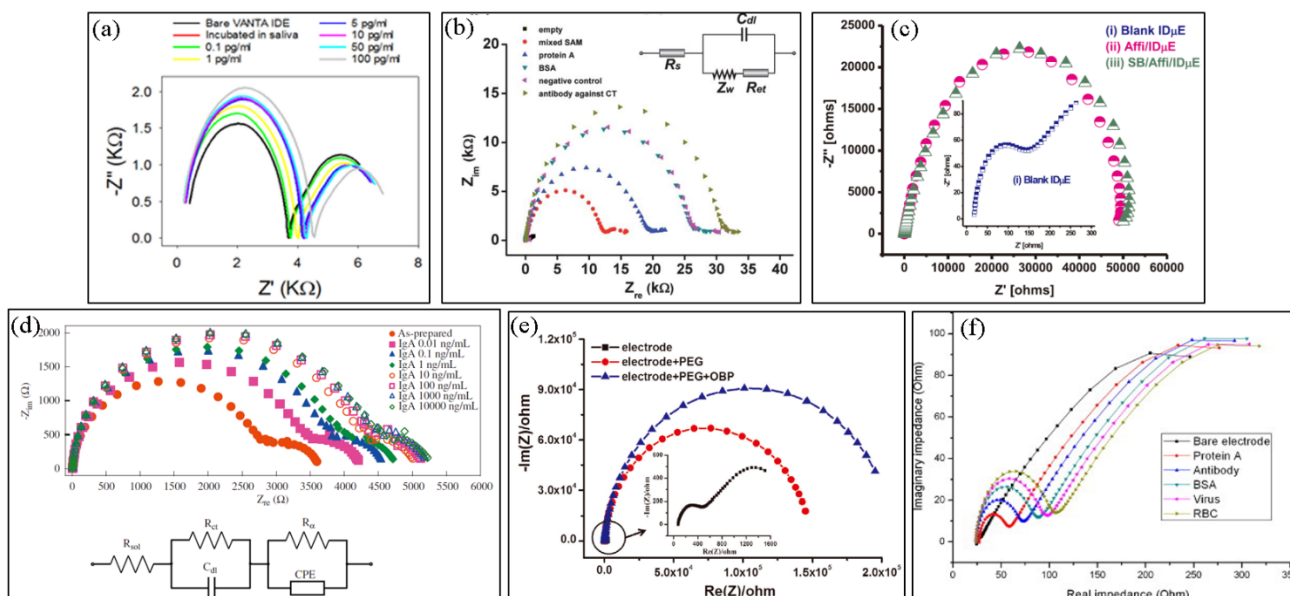
Figure 2-2 Studies exhibiting IDA diffusion phenomenon. (a) (Ding et al., 2018) (b) (Chiriaco et al., 2011) (c) (Zhurauski et al., 2018) (d) (Ohno et al., 2013) (e) (Lu et al., 2015) (f) (R. Wang et al., 2009).

2.3 Equivalent Circuit Fitting for Symmetric Electrode Systems

Symmetric electrochemical systems implement a two electrode setup with the WE and CE/RE having the same material and are often used in energy-storage systems (L. Zhang et al., 2016). These systems are also used in impedimetric bio-sensing applications, where electrodes of different geometries such as IDA electrodes can be used. However, for equivalent circuit fitting of these systems with redox species present, two Randles circuit in series must be used for characterizing the system parameters because both electrodes are involved in reaction. This might cause overfitting of parameters and may slow down the fitting process. A way to solve this problem is to set equal parameter values between the two circuits, so that the number of parameters should equal to a single Randles circuit. Should the fitting results be effective if one used only a single Randles circuit in symmetric systems? Previous literatures on bio-detection using IDA electrodes have shown it is possible (Yan et al., 2011). However, a detailed derivation of why it can be done hasn't yet been carried out. In Chapter 4, the relationship of Randles circuit parameters (e.g. R_{ct} or R_s) between three and symmetric electrode setups is derived. Using this relationship, one is able to calculate parameters of symmetric setups by using a single Randles circuit.

18

2.4 Miniaturized Electrochemical Systems

Electrochemical methods may seem attractive, but when dealing with samples which are mostly liquid, one has to prepare bulky containers with large volumes of test buffers for the electrochemical setup. Moreover, over dilution of a sample into the bulk solution may result in a low detection signal, making accurate data acquisition hard to perform. Regarding point-of-care diagnostics, measurements using bulky systems such as a typical three electrode electrochemical setup are almost impossible to accomplish. Portable and miniaturized sensing devices and methods must be developed in order to cater to the market and medical needs such as home applications or on-site measurements (da Silva et al., 2017; Vashist, 2017). Microfluidic systems also take up the role of achieving several features in a miniaturized system. Here the advantages of miniaturized electrochemical systems and problems that will be faced in practical implementation are discussed.

2.4.1 Implementation Issues of Two and Three Electrode Setups

A miniaturized electrochemical system manipulates small volumes of fluids in order to let them react, mix up, flow through, enter, leave or stay at a certain place in a formulated manner. The geometry is constrained to approximately sub-millimeter range, enabling it to deal with samples with little volume and environments where detection scales are crucial (Kirby, 2010). The development of these biosensors is a technology that exhibit low cost and integrable natures (Punter-Villagrasa et al., 2017; J. Wang, 2006). They could also employ other features like microfluidic real-time detection (D. Zhang et al., 2016), multiplex (Pursey et al., 2017) and smart phone controlled applications (Jiang et al., 2014; Zhang et al., 2015). Asymmetric and symmetric two electrode setups are often embedded within these sensors.

While potent as it seems, a typical three electrode setup is hard to implement in a miniaturized system due to its complexity, design difficulties and low yield rate. The serious obstacles limit its ability for further miniaturization and integration developments in point-of-care applications. In microfabrication, a two electrode setup is more simple, easy to fabricate and can be made more robust. The configuration of the WE and the CE/RE can be categorized as asymmetric and symmetric. Asymmetric electrodes such as an Au WE and Pt CE/RE are simple in analysis but more complicated in fabrication (T.

20

Lim et al., 2017), while symmetric electrodes are of the opposite (Chiriaco et al., 2011).

Two electrode setups are more difficult to interpret compared with three electrode setups

since the current flows through both the CE and RE, resulting in a voltage drop on the RE

that may lead to serious inaccurate control of potential, thus the signal may rather be

compositions of reactions of both the WE and CE/RE.
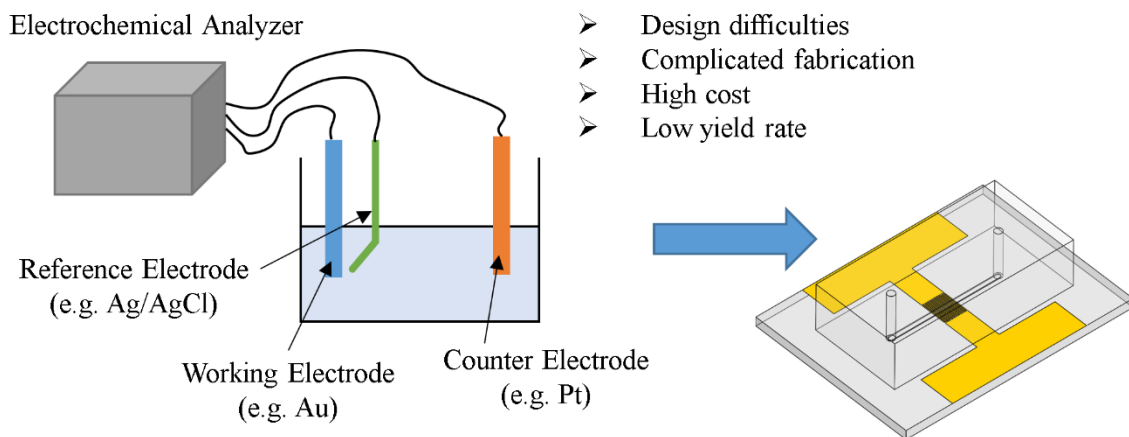
Figure 2-3 Issues in three electrode system miniaturization.

2.4.2 Miniaturized Impedimetric Detection Systems

EIS takes the advantage of two electrode miniaturized systems since only a small

voltage amplitude would be applied ($< 50mV$), which results in little penetrating current

that runs through the RE. Nevertheless, three electrode setups can also be applied. Three

electrode setups are stable in potential control and only the WE is concerned for analysis,

making it easier to interpret. However, the fabrication process usually faces obstacles

since different materials are needed to be evaporated or coated onto the electrode surface.

Moreover, in order to arrange the different electrode materials using metal heat or

electron-beam evaporation, alignment of photomasks must be accurate in order to obtain

product parameter reproducibility, which would be quite a tough skill to master in

microfabrication and requires precise machinery.

On the other hand, symmetric two electrode setups are a lot easier to fabricate and

can be reproduced easily even with simple manually controlled aligners during

microfabrication process, though potential control in these systems may shift and analysis

of electrochemical data would most likely be the summation of the WE and CE/RE.

Microfluidic impedimetric two electrode setup studies have also been published in recent

years with wide ranges of applications. There are three electrode setups though not as

widely discussed as two electrode setups. Subjects using three electrode setups include

22

cell detection (Manczak et al., 2016), while others using two electrode setups also involve

disease diagnosis (T. Lim et al., 2017), virus detection (Lum et al., 2015), microparticle

sensing (Z. Zou et al., 2008) … etc.

Publications comparing recent studies using microfluidic or microelectrode

impedimetric chips are systematically listed in Table 2-1. Parameters such as electrode

geometry, independent variables, electrode material, location (in solution or on electrode)

and detection of limit (LOD) are compared.
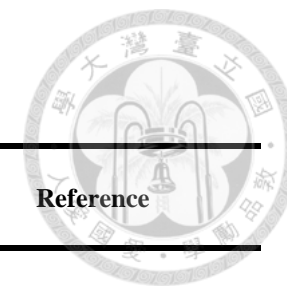
Table 2-1 Comparison of microfluidic and microelectrode impedimetric chip systems.

Electrode material (main / adhesive layer)	Independent variable or principle	Location	Electrode geometry	LOD	Reference
Au/Cu (0.15/35μm)	concentration of Cry1Ab/aptamer immobilized on magnetic beads	in solution	circular plate	15pM	(Jin et al., 2017)
Au/Ti (200/15 nm)	bacteria concentration	in solution	interdigitated array	10cells/mL	(Jiang et al., 2014)
Au/Ti (100/10 nm)	NaCl concentration between electrodes	in solution	rod	0.1μM	(Ashish et al., 2011)
Au/Ti/W (100/10/10 nm)	thrombin/aptamer concentration immobilized on magnetic beads	in solution	interdigitated array	10pM	(Y. Wang et al., 2014)
Au/COC (100nm / NA)	dielectrophoresis aroused microparticle entrapment	around electrode	interdigitated array	NA	(Z. Zou et al., 2008)
Au/Ti (150/5 nm)	ssDNA base pairing	on electrode	interdigitated array	NA	(Nadja E Solis-Marcano, 2016)
Au/Ti (80/20 nm)	DNA/miRNA Hybridization	on electrode	circular plate	1pM	(Capaldo et al., 2016)
Au/COC (50nm / NA)	concentration of IgG1/Protein A binding	on electrode	rectangular	NA	(Vandenryt et al., 2013)
Au	concentration of cholera toxin/antibody binding	on electrode	interdigitated array	10pM	(Chiriaco et al., 2011)
Au/Ti (100/10 nm)	concentration of myoglobin/antibody binding	on electrode	board	NA	(Tweedie et al., 2006)
Au/Cr (200/10 nm) Au/COC (100nm / NA)	concentration of IgG/antibody binding	on electrode	interdigitated array	NA	(Zhiwei Zou et al., 2007)
Au/Cr (200/5 nm)	concentration of IgE/antibody binding	on electrode	square	0.1nM	(D. Xu et al., 2005)
Au/Cr (80/20 nm)	concentration of thrombin/aptamer binding	on electrode	interdigitated array	NA	This research
Au/Cr (80/20 nm)	concentration of MUC1/aptamer binding	on electrode	interdigitated array	NA	This research (Appendix)

24

2.5 Affinity-Based Detection using Aptasensors

Aptamers are artificially synthesized DNA or RNA that can be selected *in vitro* to obtain affinity and selectivity to its binding target such as proteins, ions, small molecules, cells or viruses and have emerged as an innovative interest of study in the past two decades (Keefe et al., 2010; Zhou and Rossi, 2016). In order for aptamers to specifically bind to a target analyte, a technique called systematic evolution of ligands by exponential enrichment (SELEX) can be implemented, which is a molecular biological method for the evolution of aptamers (Tuerk and Gold, 1990).

DNA aptamers are robust and stable due to its constructive nature compared with antibodies and can also serve as the recognition element in affinity-based biosensors (Hianik and Wang, 2009; Y. C. Lim et al., 2010). Impedimetric aptasensors are biosensors that use aptamers as the sensing element for detecting a specific analyte and use EIS for target measurement. Radi et al. took the lead of designing and developing a reusable impedimetric aptasensor that can detect thrombin (Radi et al., 2005). The thrombin binding aptamers are thiolated at 3' end, which lets them form a self-assembled monolayer (SAM) on a smooth, clean Au electrode surface when being immobilized (Vericat et al., 2010), and $Fe(CN)_6^{3-/4-}$ is used as the redox species for EIS measurement.

25
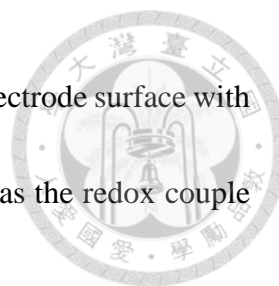
The general process for thiolated aptamer immobilization on an Au electrode surface with 6-mercaptohexanol (MCH) as the blocking reagent and $Fe(CN)_6^{3-/4-}$ as the redox couple (species) is illustrated in Figure 2-4.
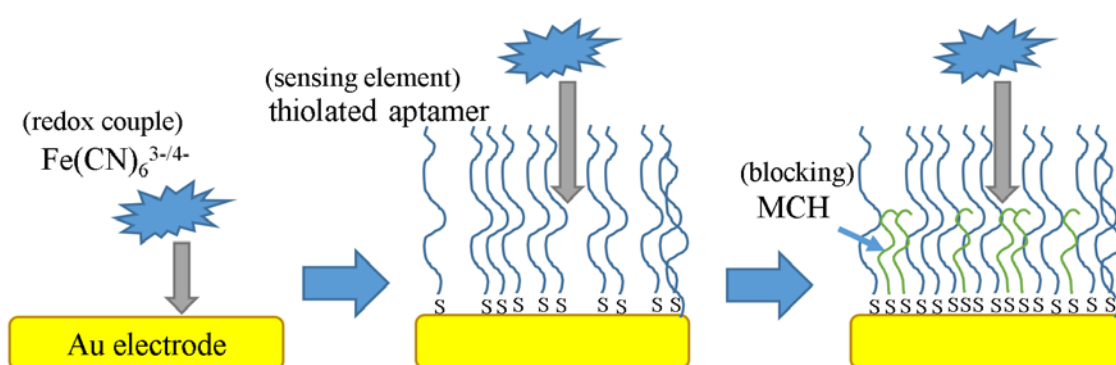
Figure 2-4 Typical process for aptamer immobilization on Au electrodes.

Liu et al. realized a sensitive impedimetric MUC1 aptasensor by immobilizing a partially complementary S2.2 aptamer sequence onto an Au electrode using thiol-gold interaction followed by partial base pairing of S2.2 sequences that are immobilized on gold nanoparticles (Figure 2-5). Different concentrations of MUC1 in the solution competed with the complementary S2.2 and broke apart the partial base pairing, resulting in a decreasing R_{ct} value as the MUC1 concentration increases (Liu et al., 2015). There are also other label-free impedimetric aptasensors that are dedicated to pathogen detection (Brosel-Oliu et al., 2018; Reich et al., 2017), food safety (Malvano et al., 2017) and other biomarkers (Jolly et al., 2015).
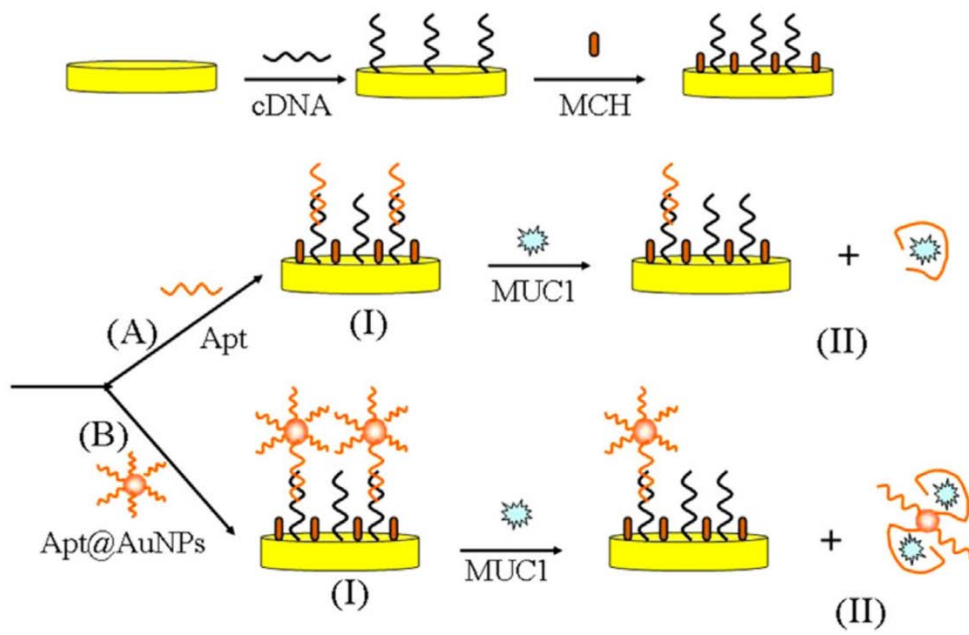
Figure 2-5 Schematic representation of the electrochemical aptasensor for the detection of MUC1 (Liu et al., 2015).
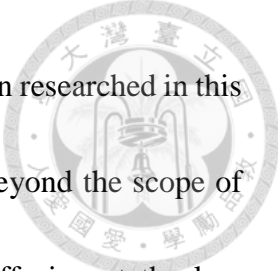
Chapter 3 Diffusion Impedance Modeling for IDA Electrodes

3.1 Brief Introduction

In the present study, an integral equation for approximating the diffusion impedance of an IDA electrode is proposed. To the best of the author's knowledge, this is the first approach for derivation of its diffusion impedance regarding relevant parameters such as the electrode bandwidth (w_e) and gap width (w_g). Conformal mapping methods for calculating the finite diffusion length of every point on the electrode and cylindrical finite diffusion approximations in a differential area are implemented. The solution is able to calculate IDA diffusion impedances of different geometries and frequencies, constructed into an element for equivalent circuit fitting, and even degenerated to obtain the limiting current. A command line program for calculating the IDA diffusion impedance is provided in supplementary material. This can help researchers model their IDA electrode system more accurately for a variety of applications.

To make a clearer view of the finite diffusion phenomenon using IDA electrodes, an experimental EIS data is demonstrated in Figure 3-1 (solid triangles). At high frequencies, an imperfect semi-circle can be seen. This is caused by faradaic charge transfer processes on non-uniform metal surfaces, which the surface roughness or other

28

factors can be accounted for (Lasia, 2002). Extensive studies have been researched in this

area (Mulder et al., 1990; Orazem and Tribollet, 2011), which are beyond the scope of

this work. Therefore, this work focuses on the phenomenon of diffusion at the low

frequency area. (For the double layer capacitance, a constant phase element (CPE or Q)

in place of a capacitor (C) is used. Q_{dl} is a common element for equivalent circuit fitting

when using a Randles circuit (Shoar Abouzari et al., 2009).) At low frequencies, a

decrease of phase angle can be seen, making the impedance bend towards the real axis.

This is caused by finite diffusion of redox species between the electrodes. The whole

spectrum is fitted using the Randles circuit with a Warburg element modeling the

diffusion impedance (Figure 3-1 top-left subfigure), but failed to achieve a good enough

result (Fig. S1 hollow triangles). Obviously, there are large errors between the real and

fitted value of certain parameters such as the charge transfer resistance (R_{ct}) or double

layer capacitance (Q_{dl}). The problem of erroneous fitting can be fixed if a frequency range

where the diffusion effect doesn't exist is arbitrarily selected. Also, if the R_{ct} had been

bigger, the significance of the diffusion impedance would be smaller and can eventually

be neglected. However, neither can provide methods for parameterizing the diffusion

nature within these systems. If a more general equivalent circuit element for replacing the

Warburg element is needed to obtain accurate enough results, then a theory should be

developed for calculating the diffusion impedance of an IDA electrode. There are three

29
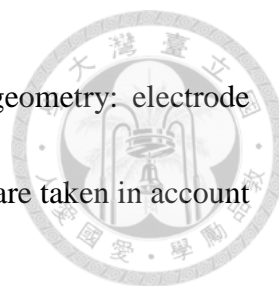
unique parameters in a symmetric IDA electrode with a certain geometry: electrode

bandwidth (w_e), gap width (w_g) and length of electrode (l). All these are taken in account

for the derivation of the theory.
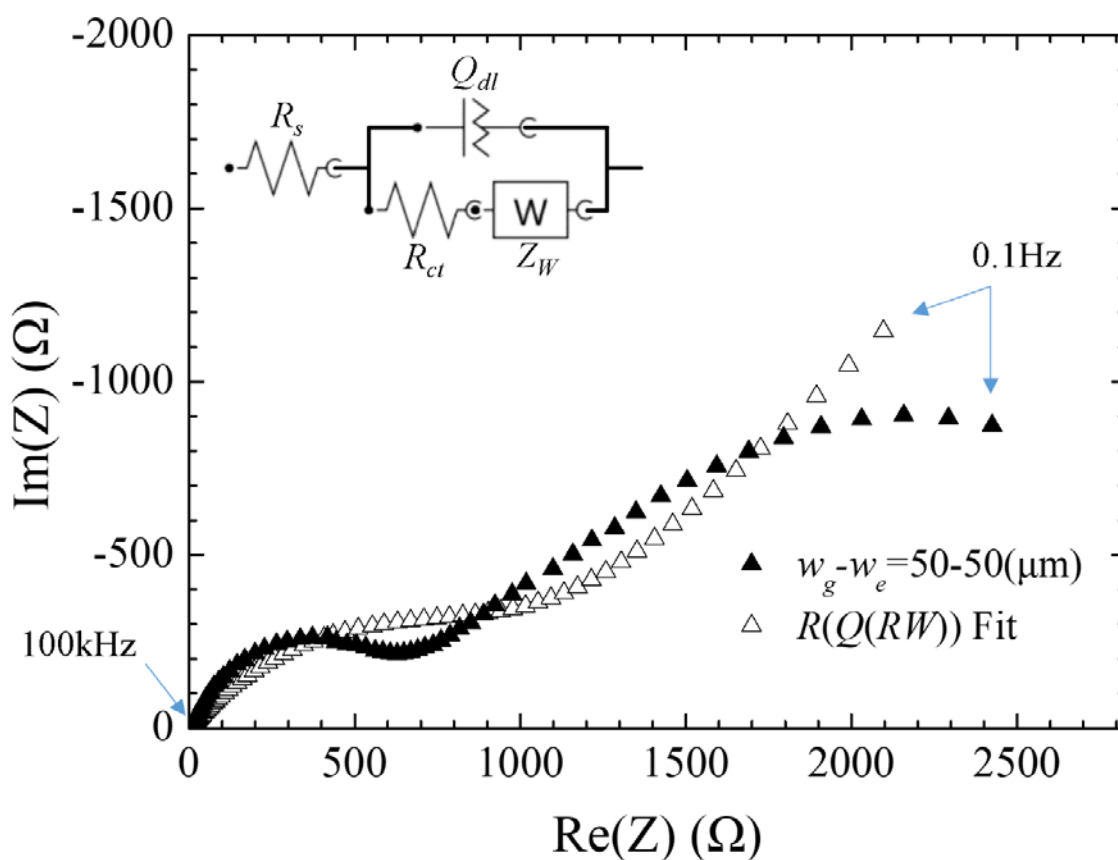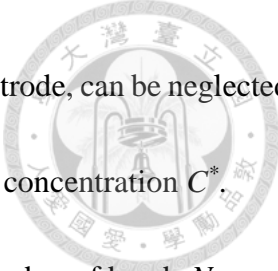
Figure 3-1 Nyquist plot of EIS data of a bare Au IDA electrode (▲) and its fitted data (△). The electrode bandwidth (w_e) and gap width (w_g) are 50μm. The equivalent circuit used is shown at the upper left corner, which is a Randles circuit that uses a constant phase element (CPE or Q) for modeling the double layer capacitance. The solution contains 0.1M KCl and 5mM $Fe(CN)_6^{3-/4-}$. The frequency range of the data is 10^{-1}~10^5Hz.

30

3.2 Theory

The goal of this theory is to derive a solution for approximating the diffusion

impedance of an IDA electrode. The electrode is assumed to have a gap width of w_g and

a common bandwidth of w_e. In the first section of this theory, the unit cell is introduced

for simplification of calculations. An imaginary constant concentration boundary inside

the cell is deduced, and redox species can diffuse between this boundary and the electrode.

In the second section, the equations for calculating finite diffusion lengths of every point

on the electrode is derived. In the third section, cylindrical finite diffusion approximations

are performed within a differential area of the diffusion path. By combining these

derivations, an integral form of solution is presented. One is able to calculate the diffusion

impedance of an IDA electrode with arbitrarily defined w_e and w_g at any frequency. In the

fourth section, the solution is transformed into a dimensionless form, yielding two unique

dimensionless parameters and another commonly known parameter. This form can be

used in equivalent circuit fitting, which the parameters can be predicted from a single EIS

experimental data. In the last section, a limiting case of the diffusion impedance with

geometrical parameters is explored and the reduced impedance equation is deduced. For

derivation of this theory, the following assumptions are made:

31

I.   Edge effects, either at the horizontal or vertical edge of the IDA electrode, can be neglected.

II. Both redox species have the same diffusion coefficient D and bulk concentration C^*.

III. The pair of electrodes have a common bandwidth w_e and a total number of bands N.

IV. The concentration throughout has reached a periodic-steady-state, which can be expressed as a phasor $\widetilde{C}$ (Lasia, 2002).

V.   The solution above the electrode extends infinitely.

VI. The height of the electrode is sufficiently small and can be assumed as zero.

VII. Due to the small voltage amplitude applied, presence of supporting electrolyte and static measurements, migration and convection effects are neglected.

3.2.1 Unit Cell and Imaginary Constant Concentration Boundary (ICCB)

The unit cell is a well-known representation for calculation simplification of IDA electrode geometries (Aoki et al., 1988; Bhuiyan et al., 2015; Morita et al., 2014). In brief, it consists of two halves of a pair of electrode band and the above semi-infinite strip of solution (Figure 3-2a). The cell width w has the relationship:

$$w = w_e + w_g \tag{1}$$

By neglecting edge effects (assumption I), the relationship between the impedance of an IDA electrode and its corresponding unit cell is

32
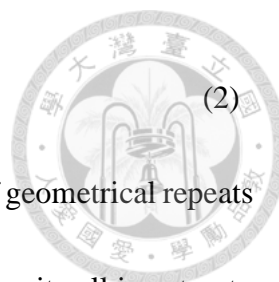
$$Z_{diff-IDA} = \frac{Z_{unit\ cell}}{N} \tag{2}$$

, which is quite obvious because the whole electrode can be thought of geometrical repeats

of N unit cells. For the convenience of the following derivations, the unit cell is put onto

a complex plane (z-plane), where the left boundary is on Re(z) = 0 and the right boundary

is on Re(z) = w. The reaction is identical at every point along any axis perpendicular to

this plane.

(a) (b)
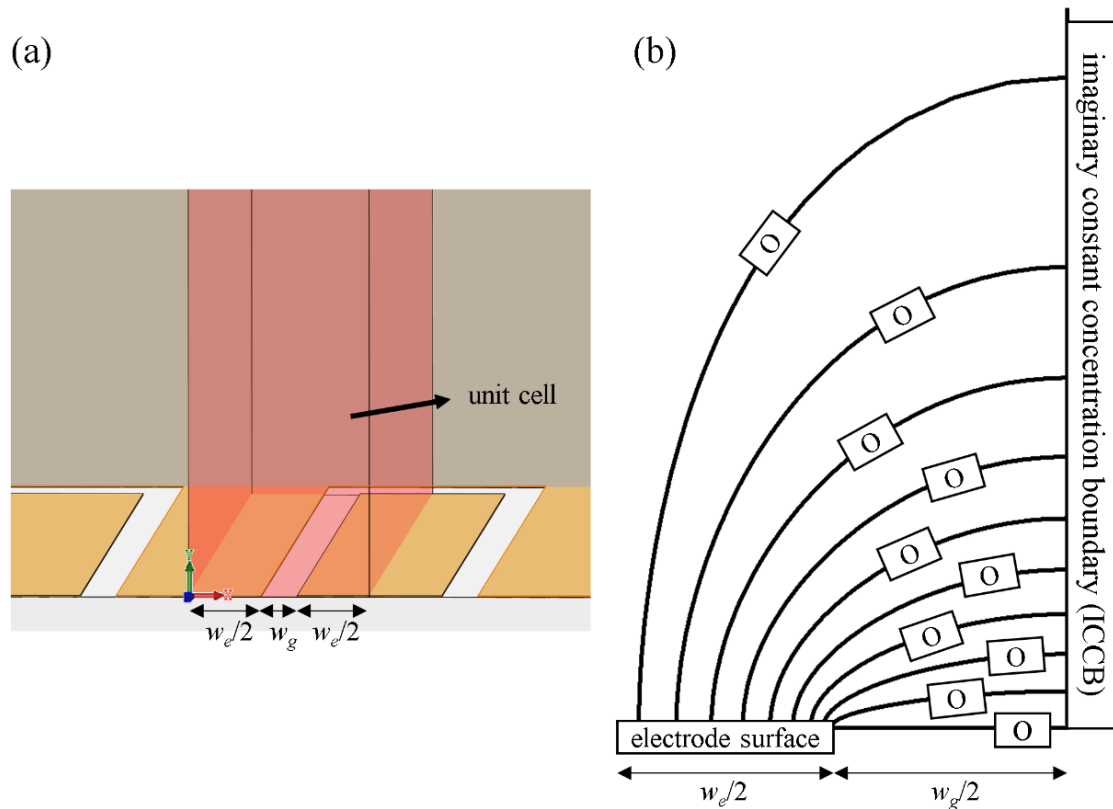
Figure 3-2 (a) Geometric definition of a unit cell (red translucent region). (b) Open finite-length diffusion elements link between the ICCB and the electrode surface within the left half of a unit cell.
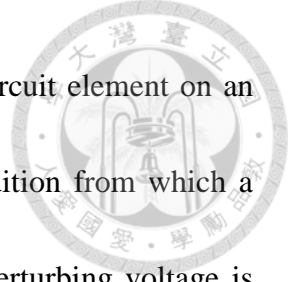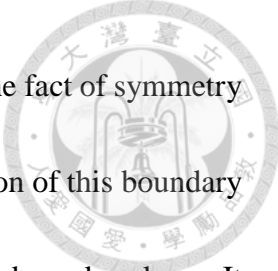
If one considers the possibility of applying any equivalent circuit element on an IDA electrode, there exists a problem that no clear boundary condition from which a certain redox concentration can be defined. However, if a small perturbing voltage is applied between the two electrodes of a symmetric IDA electrode, the potential should be equally distributed among the two electrodes (Chen and Ho, 2001). Moreover, by assumption II, the oxidization rate at a certain point on one electrode should equal the reduction rate of the other electrode at the point symmetrical about the line $\text{Re}(z) = w/2$. This leads to the result of the concentration change of oxidized species ($\Delta C_O = C_O - C^*$) and reduced species ($\Delta C_R = C_R - C^*$) being symmetrical about $\text{Re}(z) = w/2$ everywhere at any time. Also, the increase of oxidized species should equal the decrease of reduced species at any point on the electrode. Therefore, due to geometrical symmetry, it can be conceived that at any point z within the unit cell,

$$\Delta C_O(z) = \Delta C_R(w - z) = -\Delta C_R(z) \tag{3}$$

Substituting the definition of ΔC_O and ΔC_R, one can obtain

$$C_O(z) + C_O(w - z) = 2C^* \ \text{ and } \ C_R(z) + C_R(w - z) = 2C^* \tag{4}$$

According to eqn. (4), it can be derived that $C_O = C_R = C^*$ at $\text{Re}(z) = w/2$. This can be thought of as a fixed concentration boundary condition for diffusion impedance calculation of the unit cell, and is named the imaginary constant concentration boundary (abbreviated as the ICCB). Note that a detailed derivation for proving the existence of the

34

ICCB is not given. Eqn. (3) is merely a strong intuitive guess due to the fact of symmetry existing in the unit cell. Therefore, simulations are done for verification of this boundary (cf. section 3.4.3). The behavior here is actually identical to that of a boundary layer. It can be imagined that there are numerous diffusion impedance elements, each connecting one point on the ICCB and another point on the electrode (Figure 3-2b). By solving every one of them and putting them in parallel connection, the diffusion impedance of the unit cell can be calculated. However, for obtaining the diffusion impedance, the finite diffusion length at any arbitrarily selected point should be determined. This is detailed in the next section.

3.2.2 Finite Diffusion Length Derivation

In this section, the left half of a unit cell is focused on. It is clear that redox species should diffuse between the ICCB and the electrode. However, do they stay within a fixed path? What is the path? Or does the forward and backward path differ, forming some sort of loop? Aoki et al. showed that for steady-state conditions, the concentration gradient can be determined by applying conformal mappings to the unit cell on the z-plane (Aoki et al., 1988). In this way, the limiting current can be accurately approximated at different ratios of w_e and w_g. Therefore, the author considers it sufficient that by according to their methods, calculations in periodic-steady-state should be accurate to a certain degree. (For

35
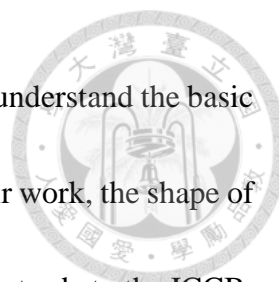
in-depth comprehension in this section, readers are recommended to understand the basic

concepts detailed in Aoki et al.'s work beforehand.) According to their work, the shape of

the diffusion path is assumed to be a quarter of an ellipse from the electrode to the ICCB.

Applying to this work, this means for an arbitrarily chosen point on the electrode $(x_e, 0)$,

there is a corresponding point for diffusion on the ICCB $(w/2, y_{ICCB})$. The finite diffusion

length of a certain point on the electrode $(0 \leq x_e \leq w_e/2)$ is defined as $L_d(x_e)$. Figure

3-3 depicts the diffusion path of a certain point on the electrode within a unit cell. Next,

the method for calculating y_{ICCB} from x_e is detailed.
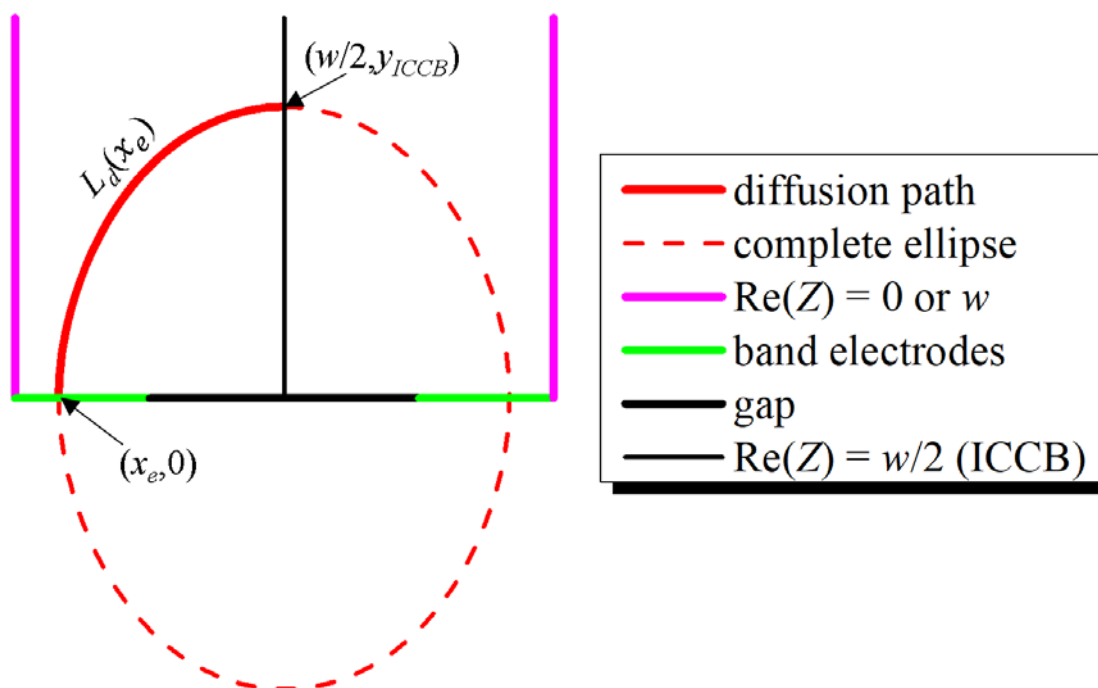
Figure 3-3 Path of redox species that finitely diffuse between the ICCB and the electrode within a unit cell. The finite diffusion length at x_e is determined by the elliptic arc length.
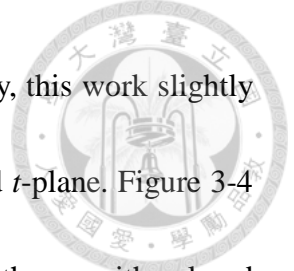
For the sake of simplicity and with the advantage of symmetry, this work slightly

modified the mapping equation derived by Aoki et al. between z and t-plane. Figure 3-4

illustrates the conformal mapping of $z \to t \to u$ plane applied in this theory with colored

contour lines and points A to F attempting to correspond them more clearly. The

transformation equations are

$$t = -\frac{1}{k}\cos\frac{z}{w}\pi \tag{5}$$

$$u = F(\sin^{-1} t \,|m) \tag{6}$$

, where $k = \cos(w_e\pi/(2w))$, $m = k^2$ and $F(\phi|m)$ is the incomplete elliptic integral of the

first kind (Sexton, 2012).

$$F(\phi|k^2) = F(\phi|m) = \int_0^\phi \frac{d\theta}{\sqrt{1 - m\sin^2\theta}} \tag{7}$$

(Note that any point (a, b) on the complex plane can also be written as a + bi.) The two

half electrode band surfaces are face-to-face on the u-plane, with the left electrode center

$B_z(0, 0)$ corresponding to $B_u(-K(m), K(1 - m))$ and the right electrode center $E_z(w, 0)$

corresponding to $E_u(K(m), K(1 - m))$, where $K(m)$ is the complete elliptic integral of

the first kind (Calixto et al., 2010). (Note that there appears to be notational variants for

the definition of elliptic integrals.)

$$K(k^2) = K(m) = \int_0^{\frac{\pi}{2}} \frac{d\theta}{\sqrt{1 - m\sin^2\theta}} \tag{8}$$

All vertical lines on the z-plane will eventually converge to $A_u = F_u(0, K(1 - m))$ as

$\text{Im}(z) \to \infty$. The only two lines remaining straight and in the same direction on all planes

37
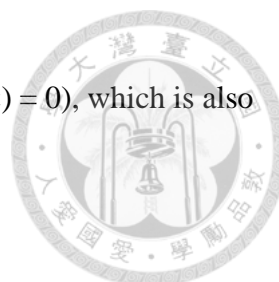
are $\overline{CD}$ and the middle vertical line (Re(z) = $w/2$, Re(t) = 0 and Re(u) = 0), which is also

the ICCB.
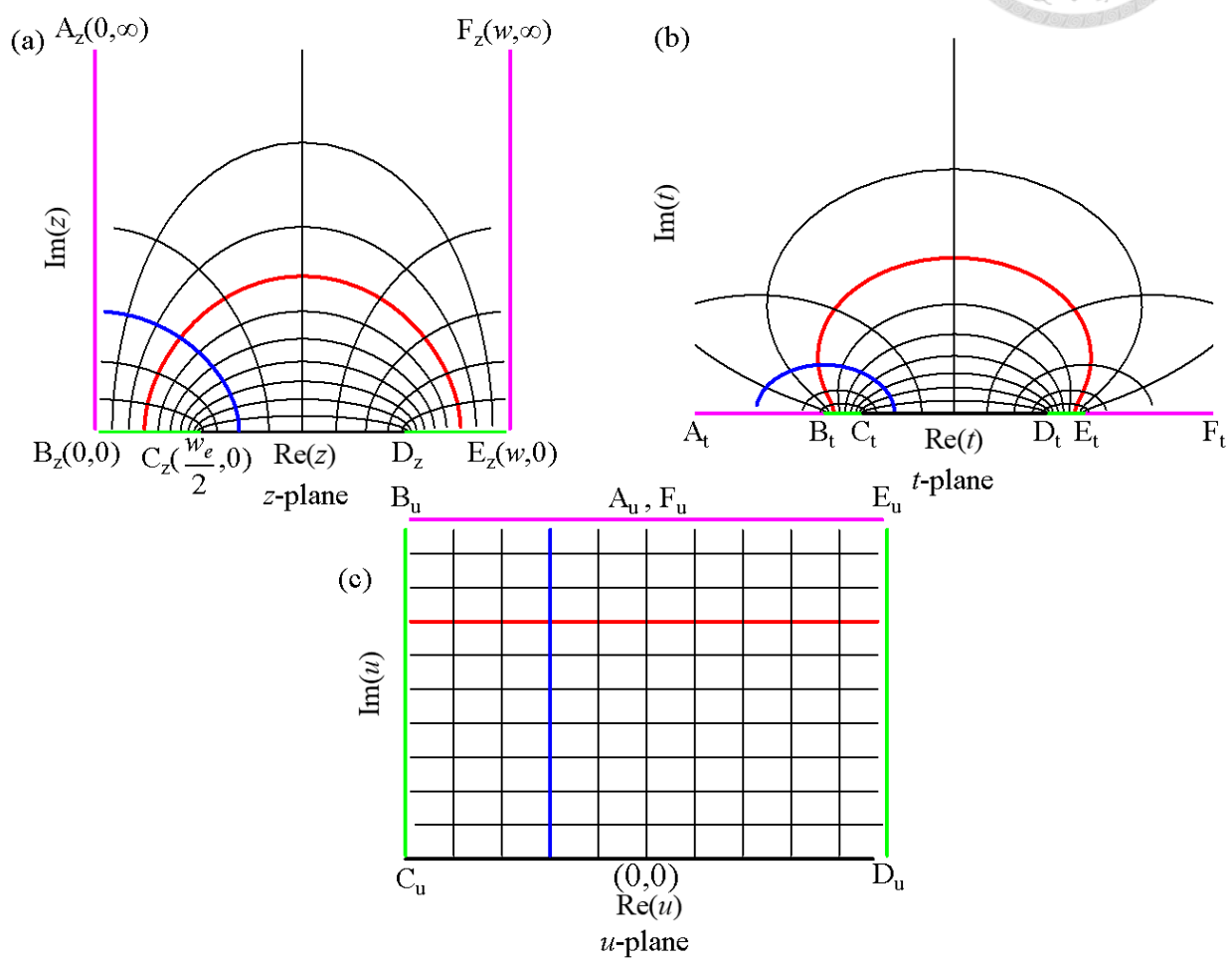
Figure 3-4 The conformal mapping of the (a)z, (b)t and (c)u plane applied in this theory.

From Figure 3-4c, the point on the electrode and its corresponding point on the

ICCB have the same imaginary part (denoted as β here) on the u-plane. Therefore, y_{ICCB}

can be found by conformal mapping of (x_e, 0) on the z-plane to ($-K(m)$, β) on the u-plane,

then mapping of (0, β) on the u-plane back to ($w/2$, y_{ICCB}) on the z-plane. According to

eqn. (5) and (6), β and y_{ICCB} satisfy the relationships

38

$$-K(m) + \beta i = F\left(\sin^{-1}\left(-\frac{\cos(x_e\pi/w)}{k}\right)\middle| m\right) \tag{9}$$

and

$$\frac{w}{2} + y_{ICCB}i = \frac{w}{\pi}\cos^{-1}\left(-k \cdot \mathrm{sn}(\beta i, m)\right) \tag{10}$$

where $\mathrm{sn}(u,m) = \mathrm{sn}(u,k^2)$ is the Jacobi elliptic function, which is defined as the

inverse of the incomplete elliptic integral of the first kind (Abramowitz, 1974).

$$\mathrm{sn}(u,m) = \sin\phi \quad \text{with} \quad u = F(\phi|m) \tag{11}$$

The calculation of y_{ICCB} can be greatly simplified using transformations and

simplifications (Sexton, 2012; Wolfram Research, ©1998–2019a, ©1998–2019b):

$$y_{ICCB} = \frac{w}{\pi}\ln\left(\sqrt{s^2 - 1} + s\right) \tag{12}$$

where

$$s = \frac{\sin\left(\frac{w_e\pi}{2w}\right)}{\sin\left(\frac{x_e\pi}{w}\right)} \tag{13}$$

A detailed derivation from eqn. (10) to (12) is presented in supplementary material

(section S.1). Note that at this point, one can already obtain y_{ICCB} from x_e using eqn. (12)

and (13). At last, $L_d(x_e)$ can be derived from the length of the semi-major and semi-minor

axis, with either one of their lengths being y_{ICCB} and the other one being $w/2 - x_e$:

$$L_d(x_e) = \left(\frac{w}{2} - x_e\right)E\left(1 - \frac{y_{ICCB}^2}{\left(\frac{w}{2} - x_e\right)^2}\right) \tag{14}$$

where $E(m)$ is the complete elliptic integral of the second kind (Calixto et al., 2010; Sexton,

2012).

$$E(m) = \int_0^{\frac{\pi}{2}} \sqrt{1 - m \sin^2 \theta} \, d\theta \qquad (15)$$
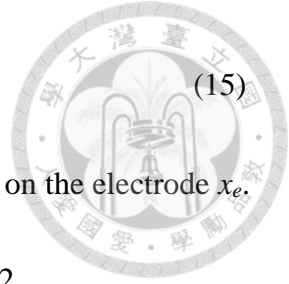
Figure 3-5 plots the finite diffusion length $L_d(x_e)$ against the position on the electrode x_e.

Reasonably, $L_d(x_e) \to \infty$ when $x_e \to 0$ and $L_d(x_e) = w_g/2$ when $x_e = w_e/2$.
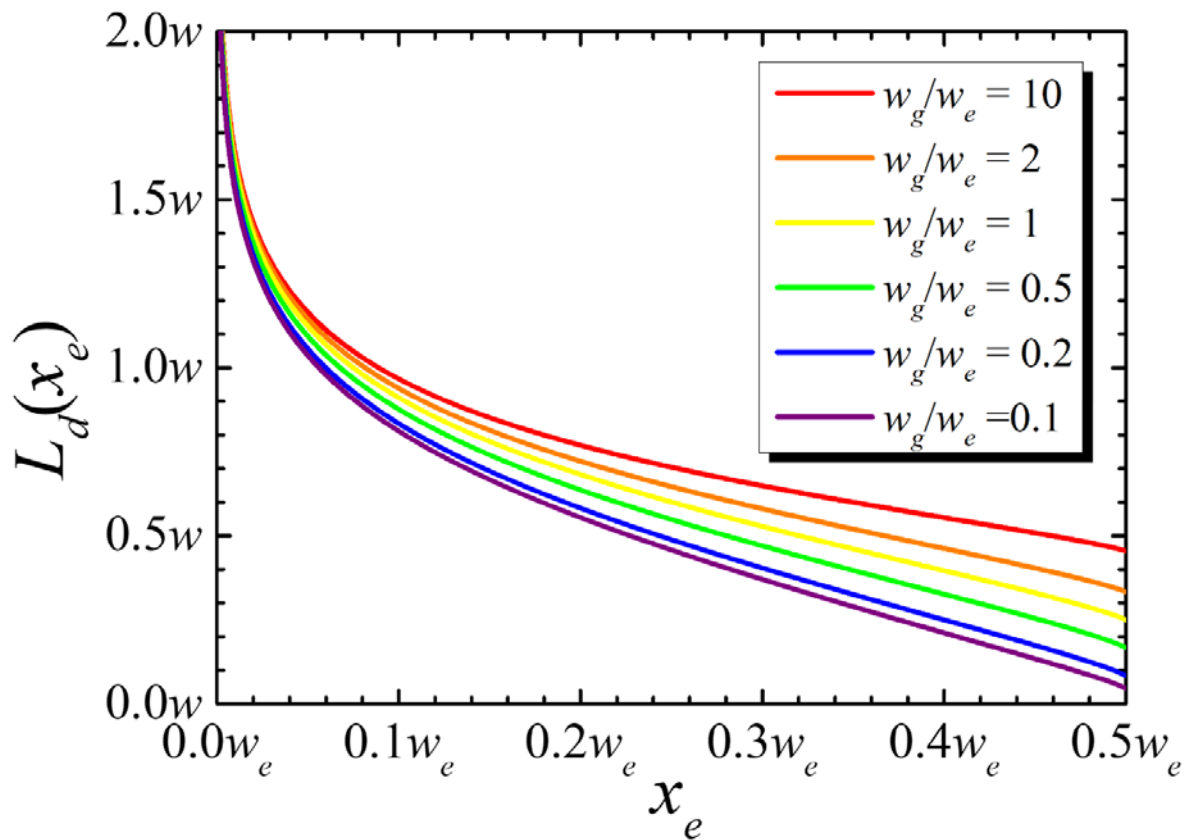
Figure 3-5 The finite diffusion length against the position on the electrode.

3.2.3 Cylindrical Finite Diffusion Inside Differential Area

The path of redox species diffusing between the ICCB and the electrode is hypothesized and calculated in the previous section. The next step is to find the specific impedance ([=] $\Omega \cdot m^2$) of a certain point on the electrode. Though the end points of any paths defined previously are always one-on-one, their differential areas are not the same. A way for acknowledging this is that the ICCB in a unit cell has infinite length extending upwards, while the electrode has only a length of $w_e/2$. In other words, for a differential length on the electrode (dx_e), its corresponding differential length on the ICCB ($-dy_{ICCB}$) isn't the same. (A minus sign is needed because as x_e becomes larger, y_{ICCB} should become smaller.) Thus, it is unable to implement the 1D finite diffusion element under this geometry.

The approach is to approximate the diffusion process using the finite cylindrical symmetry diffusion impedance derived by Jacobsen et al. (Jacobsen and West, 1995), which the specific impedance is calculated as

$$\hat{Z}_{diff-cyl} = \frac{2RT}{n^2 F^2 \sqrt{D} C^* \sqrt{j\omega}} \cdot \frac{I_0(z_\delta)K_0(z_0) - K_0(z_\delta)I_0(z_0)}{I_0(z_\delta)K_1(z_0) + K_0(z_\delta)I_1(z_0)} \tag{16}$$

where R is the gas constant, T is the temperature, n is number of electrons transferred per reaction, F is the Faraday constant, ω is the angular frequency, $j = i = \sqrt{-1}$, $I_\alpha(z_x)$ and $K_\alpha(z_x)$ (with $x = 0$ or δ and $\alpha = 0$ or 1) are the modified Bessel functions of the first and second kind (Sexton, 2012), and z_δ and z_0 are functions of r_δ and r_0, which are the radius

41
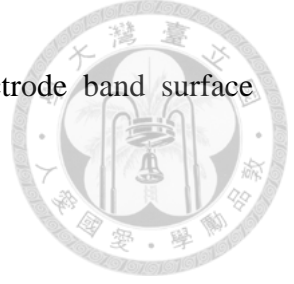
of the finite diffusion boundary layer and the radius of the electrode band surface

respectively. The relationship between z_x and r_x is

$$z_x = r_x \sqrt{\frac{j\omega}{D}} \tag{17}$$

This conversion between z_x and r_x is necessary for solving the cylindrical diffusion

impedance. For any differential area on the electrode (ldx_e), where l is the electrode length,

there must be a corresponding area where the redox species diffuse from at the ICCB (–

ldy_{ICCB}). Due to the fact that dx_e and $-dy_{ICCB}$ are small, one can approximate dx_e as the

length of a circular arc of radius r_0, and $-dy_{ICCB}$ as the length of another circular arc of

radius r_δ. Redox species diffuse a finite length of L_d between these two arcs, so L_d must

equal $r_\delta – r_0$. In other words, the small differential area within a specific diffusion path

can be approximated as having the shape of a sector of a cylinder. Figure 3-6 illustrates

the geometry with the gray area as the diffusion region of redox species. Accordingly, r_0

and r_δ have the following property:

$$r_0 = \frac{L_d}{\frac{-dy_{ICCB}}{dx_e} - 1} \tag{18}$$

and

$$r_\delta = r_0 + L_d \tag{19}$$

where

$$\frac{-dy_{ICCB}}{dx_e} = \cot\left(\frac{x_e \pi}{w}\right) \frac{s}{\sqrt{s^2 - 1}} \tag{20}$$

can be derived from finding the derivative of eqn. (12) with respect to x_e (A detailed

42
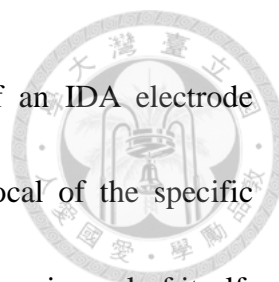
derivation is in section S.1). The overall diffusion impedance of an IDA electrode ($Z_{diff-IDA}$) can therefore be calculated by integrating the reciprocal of the specific impedance of every point on the electrode of an unit cell, taking the reciprocal of itself, and then multiplying by $2/lN$. The 2 in the numerator is because two finite diffusion impedances link in series between the left and right electrode band within a unit cell.

$$Z_{diff-IDA} = \frac{2}{lN \int \frac{1}{\hat{Z}_{diff-cyl}} dx_e}$$

$$= \frac{4RT}{lNn^2F^2\sqrt{D}C^*\sqrt{j\omega}} \left(\int_0^{\frac{w_e}{2}} \left(\frac{I_0(z_\delta)K_0(z_0) - K_0(z_\delta)I_0(z_0)}{I_0(z_\delta)K_1(z_0) + K_0(z_\delta)I_1(z_0)} \right)^{-1} dx_e \right)^{-1} \qquad (21)$$

Here, $L_d(x_e)$ can be calculated from eqn. (12) ~ (14), and z_δ and z_0 can be calculated from eqn. (17) ~ (20).
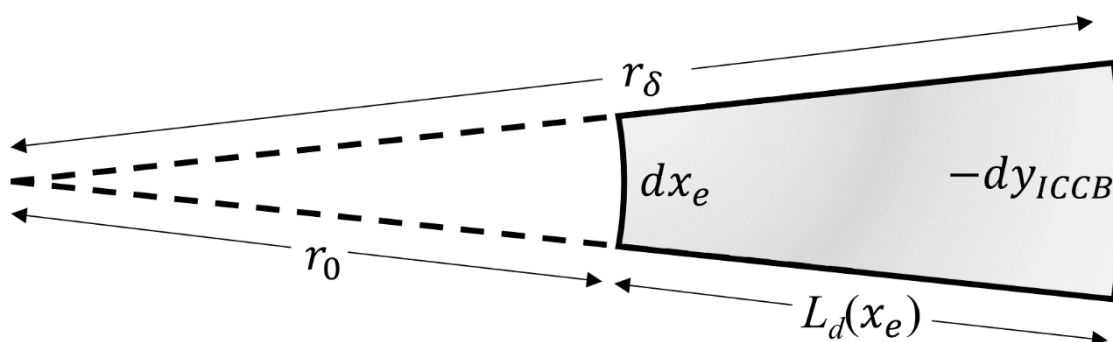
Figure 3-6 The diffusion region (gray area) of redox species between a certain length derivative of a point on the electrode (dx_e) and its corresponding length derivative on the ICCB ($-dy_{ICCB}$).
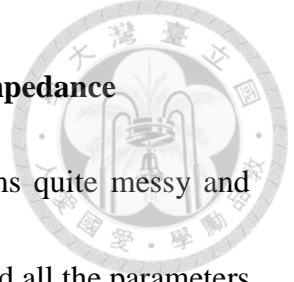
3.2.4 Dimensionless and Parameterized Form of IDA Diffusion Impedance

The IDA diffusion impedance in the form of eqn. (21) seems quite messy and complicated, having a total of nine parameters. It is impossible to find all the parameters using experimental EIS data. For example, l and N only contribute to the magnitude of impedance, so it is not feasible to find them individually. This makes eqn. (21) useless in fitting. For solving these problems, the equations are rearranged into a dimensionless form which yields only three parameters that can later on be constructed into an element for equivalent circuit fitting.

The dimensionless form of $L_d(x_e)$ in eqn. (14) is tackled first. In Figure 3-5, one can set $x_e' = x_e/w$ and $L_d'(x_e') = L_d(x_e)/w$, and obtain the same figure by changing the ticks correspondingly. More precisely, $L_d'(x_e')$ can be calculated as

$$L_d'(x_e') = L_d(x_e)/w = \left(\frac{1}{2} - x_e'\right) E\left(1 - \frac{(y_{ICCB}')^2}{\left(\frac{1}{2} - x_e'\right)^2}\right) \tag{22}$$

where y_{ICCB}' is the dimensionless form of y_{ICCB} and is defined as $y_{ICCB}' = y_{ICCB}/w$. It is obvious that s can be calculated by x_e' and $w_e'(= w_e/w)$. Moreover, the dimensionless form of r_0 and r_δ can be defined as

$$r_0' = r_0/w = \frac{L_d'}{\frac{-dy_{ICCB}}{dx_e} - 1} \tag{23}$$

and

$$r_\delta' = r_\delta/w = r_0' + L_d' \tag{24}$$

44

So z_x can be calculated as

$$z_x = r_x' \sqrt{j \frac{w^2 \omega}{D}}$$ (25)

where another dimensionless parameter $w^2\omega/D$ is found, which is actually the dimensionless frequency. To this point, none of the values in eqn. (21) has yet been replaced, but some of their calculation methods have changed.

A function is defined for calculating the Bessel functions inside the integral, which corresponds to the dimensionless portion of the specific impedance of cylindrical finite diffusion.

$$Cyl\left(x_e', \frac{w_e}{w}, \frac{w^2\omega}{D}\right) = \frac{I_0(z_\delta)K_0(z_0) - K_0(z_\delta)I_0(z_0)}{I_0(z_\delta)K_1(z_0) + K_0(z_\delta)I_1(z_0)}$$ (26)

The coefficient Y_0, which is the magnitude of the admittance at $\omega = 1$ rad/s for the Warburg element (A.J. Bard and Faulkner, 2000), can be used for further simplification of eqn. (21).

$$\frac{1}{Y_0} = \frac{2RT}{n^2 F^2 A \sqrt{D} C^*} = \frac{4RT}{lN w_e n^2 F^2 \sqrt{D} C^*}$$ (27)

Note that the 4 in the numerator comes from the fact that the total area of either side of an IDA electrode is only $A = lNw_e/2$. The integral can also be written in dimensionless form. At last, eqn. (21) can be rewritten in a more compact and arranged form.

$$Z_{diff-IDA} = \frac{1}{Y_0\sqrt{j\omega}} \frac{w_e}{w} \left(\int_0^{\frac{1}{2}\frac{w_e}{w}} Cyl\left(x_e', \frac{w_e}{w}, \frac{w^2\omega}{D}\right)^{-1} dx_e' \right)^{-1}$$ (28)

This can be interpreted as a Warburg element with a reshaping factor, with the first fractional part $(1/Y_0\sqrt{j\omega})$ yielding a 45° line but the other dimensionless part distorting

45
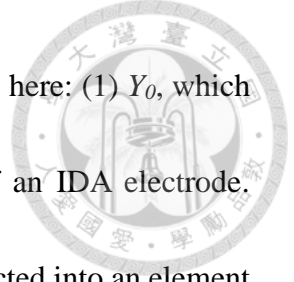
this line at all frequencies. Moreover, there are only three parameters here: (1) Y_0, which affects the magnitude of impedance. (2) w_e/w: the shape factor of an IDA electrode. (3) $w^2\omega/D$: the dimensionless frequency applied. This can be constructed into an element for circuit fitting of the IDA diffusion impedance.

3.2.5 Limiting Cases with Geometrical Parameters

It is rather obvious that when w becomes large enough and at the same time w_g/w_e is not too big nor too small, the IDA electrode would behave like ordinary planer electrodes. Even if they are coplanar, the finite diffusion length at every point on the electrode ($L_d(x_e)$) would be so long that the semi-infinite diffusion assumption can be applied. This means eqn. (28) can be reduced to the Warburg element. Considering eqn. (25), if w is large enough, then z_x should be large regardless of the other parameters. The modified Bessel functions in eqn. (26) can be calculated from asymptotic expansions, where the argument z is large (Sexton, 2012).

$$I_\alpha(z) \cong \frac{e^z}{\sqrt{2\pi z}}\left(1 - \frac{4\alpha^2 - 1}{8z} + \frac{(4\alpha^2 - 1)(4\alpha^2 - 9)}{2!\,(8z)^2} - \cdots\right) \tag{29}$$

$$K_\alpha(z) \cong \sqrt{\frac{\pi}{2z}}\,e^{-z}\left(1 + \frac{4\alpha^2 - 1}{8z} + \frac{(4\alpha^2 - 1)(4\alpha^2 - 9)}{2!\,(8z)^2} + \cdots\right) \tag{30}$$

Now if z is really large, all the terms inside the parentheses except the 1 can all be approximated as 0 in eqn. (29) and (30). Eqn. (26) thus reduces to

$$\frac{I_0(z_\delta)K_0(z_0) - K_0(z_\delta)I_0(z_0)}{I_0(z_\delta)K_1(z_0) + K_0(z_\delta)I_1(z_0)} \cong \frac{\dfrac{e^{z_\delta}}{\sqrt{2\pi z_\delta}}\sqrt{\dfrac{\pi}{2z_0}}\,e^{-z_0} - \sqrt{\dfrac{\pi}{2z_\delta}}\,e^{-z_\delta}\dfrac{e^{z_0}}{\sqrt{2\pi z_0}}}{\dfrac{e^{z_\delta}}{\sqrt{2\pi z_\delta}}\sqrt{\dfrac{\pi}{2z_0}}\,e^{-z_0} + \sqrt{\dfrac{\pi}{2z_\delta}}\,e^{-z_\delta}\dfrac{e^{z_0}}{\sqrt{2\pi z_0}}} = \tag{31}$$

46

$$\frac{e^{z_\delta - z_0} - e^{z_0 - z_\delta}}{e^{z_\delta - z_0} + e^{z_0 - z_\delta}} = \tanh(z_\delta - z_0) = \tanh\left((r'_\delta - r'_0)\sqrt{j\frac{w^2\omega}{D}}\right) = \tanh\left(L'_d\sqrt{j\frac{w^2\omega}{D}}\right) \cong 1$$

, which is reasonable because when w is large, every point on the electrode should approximately have the same specific impedance. This is because when $L_d(x_e)$ is comparatively large, the path between the ICCB and the electrode within a differential area should behave more like 1D semi-infinite diffusion (cf. Figure 3-6). At last, eqn. (28) is reduced to

$$Z_{diff-IDA} = \frac{2}{Y_0\sqrt{j\omega}} \qquad (32)$$

, where the 2 in the numerator is due to the nature of two-electrode setup (Weng et al., 2019). This means the plot should exhibit a 45° line as long as ω is big enough and the above assumptions are met. For example, let $w_g = w_e = 1$mm and $D = 6\times10^{-10}$m^2/s, for a frequency range from 100kHz to 0.1Hz, the plot would highly resemble a 45° line. There are certainly other limiting cases. For instance, if $w_e/w \rightarrow 1$, the diffusion path can be imagined to approximate a 90° arc of a circle and $-dy_{ICCB}/dx_e \rightarrow 1$. However, such applications of those cases are limited due to increased fabrication complexity or other issues.
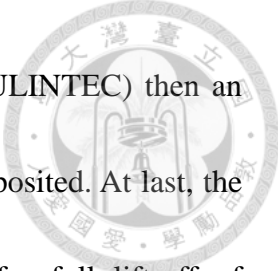
3.3 Materials and Methods

3.3.1 Reagents and Materials

All reagents such as $K_3Fe(CN)_6$, $K_4Fe(CN)_6$ and KCl are purchased from Sigma-Aldrich. Other organic solvents like ethanol, acetone, and isopropyl alcohol are obtained from HSIN MING chemical instruments co., LTD (Taipei, Taiwan). The materials and reagents used for the device construction are obtained from commercial sources as follows: glass slide (FEA, 1"×3", 1–1.2mm thickness); Au slugs, Cr pieces and crucible (Guv Team International, Taiwan); S1813 photoresist (SHIPLEY); glass photomask (NCHU, Taiwan); TMAH (Sigma); PDMS (BingBond, Taiwan).

3.3.2 Design and Fabrication

9 types of IDA electrode configurations: w_g-w_e = (1) 100-100, (2) 100-50, (3) 100-25, (4) 50-100, (5) 50-50, (6) 50-25, (7) 25-50, (8) 5-100 and (9) 2-100(μm) are designed. The electrodes are fabricated on a glass slide by a standard photolithography and deposition process. First, the glass slides are cleaned with acetone, isopropyl alcohol, ddH$_2$O sonication, and dried by N$_2$ and 120°C hotplate. Second, the positive photoresist S1813 is coated on the cleaned glass slides by spin coating at 1000rpm for 20s and 4000rpm for 60s then soft baked at 115°C for 2min. Third, the cured photoresist is exposed to UV light (15mW/cm^2) for 10s and immediately developed in TMAH for 1min.

48

Fourth, the developed chips are put into an E-beam evaporator (FULINTEC) then an adhesive layer of Cr (20nm) and electrode material Au (80nm) is deposited. At last, the chips are immersed in acetone overnight, sonicated in acetone for full lift-off of photoresist, washed with ddH_2O and dried by a stream of N_2. In order to restrict the working area of the IDA electrode, microwells of 4mm thickness with an inner empty rectangular shape are designed and fabricated. The empty rectangular shape has a length of 3mm parallel to the electrode bands and a variable width perpendicular to them to contain all the electrode area. For microwell fabrication, PDMS with a standard mixing ratio of 10:1 is poured into its aluminum mold (fabricated by a CNC machine), cured at 150°C for 10 min, cooled then peeled off. Finally, for bonding of the microwell to the IDA electrode glass chip, a reusable PLA fixture for clipping them together is designed and fabricated by a 3D printer. Several specifications of fixtures are designed for different microwells to balance between firmness and elasticity and one can be confident that the it doesn't cause deformation of the microwell or leakage. The illustration of the clipped microwell on IDA electrode chip is in Figure 3-7a and a photograph is shown in Figure 3-7b.
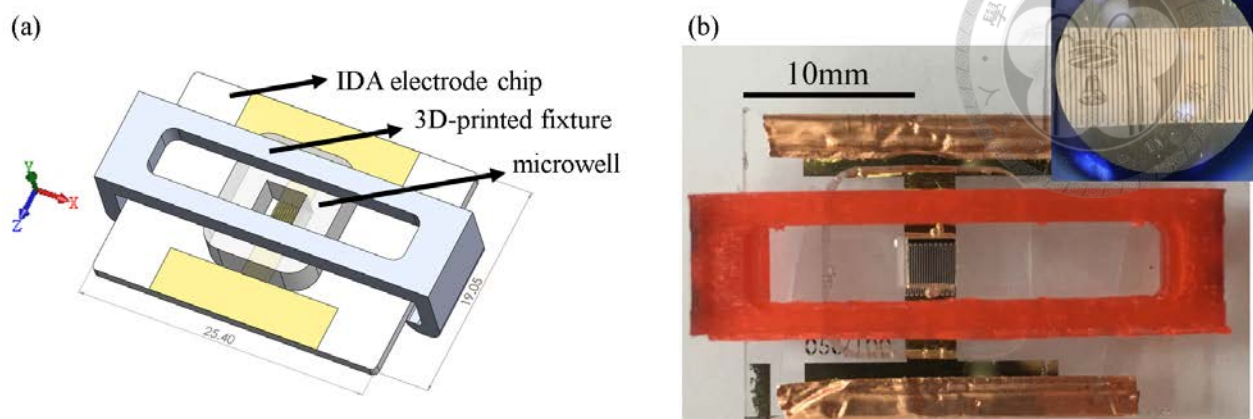
Figure 3-7 (a) Illustration and (b) photograph of the IDA electrode chip clipped with a microwell.

3.3.3 Electrochemical Characterization

The chips are immersed in a piranha solution ($H_2SO_4:H_2O_2 = 3:1(v/v)$) for 5min, rinsed by ddH$_2$O, dried by N$_2$, clipped with microwells and the two electrode pads at the side are pasted with copper tape prior to electrochemical measurements. The solution including the redox species for EIS, CV and CA measurements is 5mM K$_3$Fe(CN)$_6$, 5mM K$_4$Fe(CN)$_6$ and 0.1M KCl in 40μL ddH$_2$O. CA measurements with no K$_4$Fe(CN)$_6$ are also performed. A two-electrode configuration is used throughout these methods with one side of the electrode connecting to the CE/RE and the other connecting to the WE. An electrochemical workstation is used (CH Instruments). In EIS experiments, an AC voltage amplitude of 5mV with no DC voltage is applied and the frequency range is $10^{-2} \sim 10^{5}$Hz. In CV experiments, a scan window of -0.5~0.5V (vs CE/RE) is set and the scan rates are 20mV/s, 100mV/s and 500mV/s. In CA experiments, a potential step of -0.2V is applied for 10s after an initial given voltage of 0V.
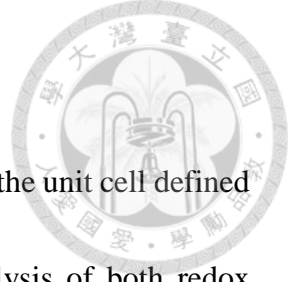
3.3.4 Simulation of Concentration Profile

Simulation for the 2D time-dependent concentration profile of the unit cell defined

in theory is carried out using COMSOL Multiphysics. Electroanalysis of both redox

species are performed. The time-dependent concentration profile for species i can be

calculated using finite difference method of the equation below:

$$\frac{\partial C_i}{\partial t} + \nabla \cdot (-D_i \nabla C_i) = R_i \tag{33}$$

where C_i is the concentration of species i, D_i is its diffusion coefficient and R_i is its

generation rate. The flux of species i can be calculated as:

$$\boldsymbol{N}_i = -D_i \nabla C_i \tag{34}$$

For redox reactions at the electrode, an electroanalytical Butler-Volmer equation is

applied:

$$i_{loc} = nFk_0 \left(C_R e^{\frac{(n-\alpha_c)F\eta}{RT}} - C_O e^{-\frac{\alpha_c F\eta}{RT}} \right) \tag{35}$$

where i_{loc} is the current density, k_0 is the heterogeneous rate constant, α_c is the cathodic

transfer coefficient and η is the overpotential. It is already known that $n = 1$, and $\alpha_c = 0.5$

is set. Global constant parameters $l = 3\text{mm}$ (electrode length), $C^*_{initial} = 5\text{mM}$ (initial

bulk concentration), $D = D_O = D_R = 6 \times 10^{-10} \text{m}^2/\text{s}$, $V_{amp} = 5\text{mV}$ (applied AC voltage), $k_0 =$

0.01m/s and $T = 298\text{K}$ are set. The reason of k_0 being so high is because a diffusion

controlled reaction with redox species rapidly reacting at the electrode is assumed. The

height of the unit cell is set as $2w$ for computational needs, and this study has proven in

51

supplementary material that this height is large enough to keep simulations accurate (section 3.4.2). The other parameters: w_g, w_e and f (frequency) are being given different values for required experiments. The geometry of the unit cell is set using the same definition in the theory. Boundaries with no flux are set at the top and electrode gap of the unit cell. Symmetry boundaries are set at the left and right. The electrode surface at the left is set as the WE with a start potential of 0V, linear voltage sweep rate of $4V_{amp}f$, lower vertex potential of $-V_{amp}$ and upper vertex potential of V_{amp}. The electrode surface at the right is set as the CE with an initial potential value of 0V. For keeping an acceptable computational time, a predefined value of "Finer" is used as the element size. However, to make simulations accurate enough, a "Free Triangle → Distribution" with an element number of 20 and an element ratio of 2 on the two electrode surfaces are set. All other parameters are as of system default. At last, time-dependent studies with a time step of 0.1s and overall periods of at least 2s are computed.

3.3.5 Impedance Calculation and Circuit Fitting Program

For preliminary implementation of necessary calculations, a MATLAB software (R2018b) is used to tackle with complicated functions such as complete, incomplete elliptic integrals and modified Bessel functions that mostly take complex numbers as the input parameter. However, this software is used only for figure drawing and some part of theory confirmation but not the calculation of impedance due to the fact that numerical integrations are needed for calculating the IDA diffusion impedance which may cause comparatively longer computational time.

A program written in C language is designed using the open-source numerical analysis library ALGLIB$^\circledR$ to implement numerical integrations and calculations of the equations in the theory. Bessel functions and the complete elliptic integral of the second kind are pre-calculated and saved in a 1D array. Faster numerical integration can therefore be carried out. A program for calculating the IDA diffusion impedance is designed according to the theory. ALGLIB is also used for non-linear least squares fitting of EIS data using Levenberg-Marquardt method. A program for fitting any user-defined equivalent circuit is designed with several elements available including the IDA diffusion element derived in the theory.

53

3.4 Results and Discussion

3.4.1 Interpretation of Normalized IDA Diffusion Impedance

Figure 3-8 shows the calculated normalized IDA diffusion impedance using eqn.

(28) for different values of w_g/w_e and constant N. When $w_g/w_e \ll 1$, the plot is made up of

a 45° line at high frequencies and an imperfect semicircle at low frequencies. When w_g/w_e

$\gg 1$, the imaginary part exhibits an almost constant value before bending towards the real

axis at low frequencies. This slightly resembles the true finite cylindrical diffusion

impedance when $r_\delta/r_0 > 1$ (Jacobsen and West, 1995) with two major differences. The first

is that a perfect semicircle appears in finite cylindrical diffusion at $r_\delta/r_0 \to 1$. This is

reasonable due to the fact that in IDA diffusion, L_d always vary with x_e (cf. Figure 3-5);

while in cylindrical diffusion, L_d is constant at every point on the electrode. The second

is that the equi-frequency line appears to be more linear compared with cylindrical

diffusion due to geometrical differences.

There's an especially remarkable point about the above calculations. The method

for impedance derivation using cylindrical finite diffusion approximation is by no means

similar to the method for limiting current derivation done in Aoki et al.'s work. This study

is by calculating the cylindrical finite diffusion impedance and theirs by finding the exact

solution of 2D concentration profile. However, if $\omega \to 0$ is set and taken into eqn. (28),

one shall obtain a linear correlation of $R^2 = 0.992$ with the reciprocal of limiting current

54
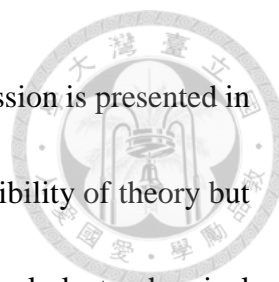
values calculated from eqn. (38) in their work. A more detailed discussion is presented in section 3.4.4. This not only serves as a powerful support for the credibility of theory but also indicates that this study has potential to bridge multi-dimensional electrochemical analytical methods together with more general equations for IDA electrodes. Impedances calculated at non-zero ω can therefore be more reliable.
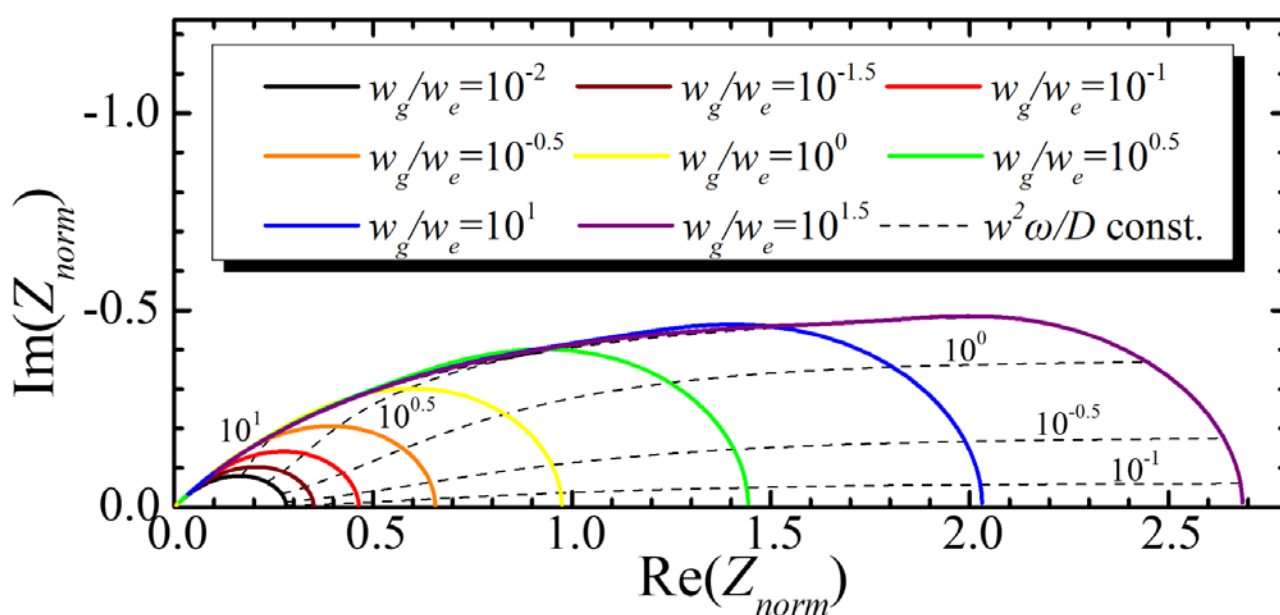
Figure 3-8 Theoretical normalized IDA diffusion impedance for different values of w_g/w_e and constant number of bands (N). The numbers beside the equi-frequency (dashed) lines indicate the reduced frequency $w^2\omega/D$.

3.4.2 Characterization of IDA Electrode Microwell Chip

The fabrication of IDA electrodes using photolithography involves fine tuning of parameters and precise control of instrumentation. A major concern is whether the gap and electrode band are of ideal width and ratio. The consistency of height and roughness of the electrode may also have important influence on experimental results (A.J. Bard and Faulkner, 2000). For characterization of the IDA electrode, a probe-type surface analyzer (KOSAKA ET-4000) is used for obtaining the 1D profile of height (y) in the x direction at a fixed z (Figure 3-9).
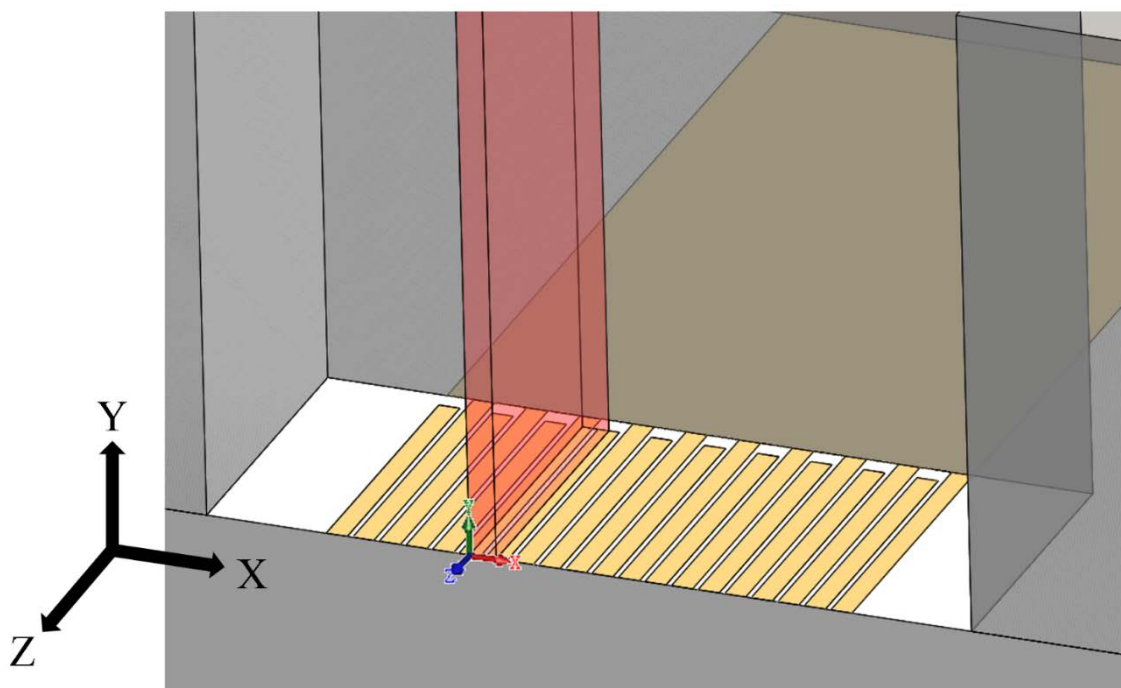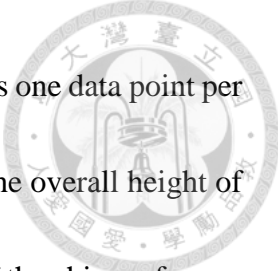
Figure 3-9 Sectional view of the microwell chip with the red translucent region as the defined unit cell with coordinates.

56

The analyzer has a measuring reproducibility of < 5Å and acquires one data point per 130nm. The raw data appeared to have huge drifts of 2.5±1.5μm on the overall height of the electrodes. This may be caused by the tilt of chip, or inclination of the chip surface or the platform itself. A baseline normalization program is designed to offset this kind of bias. An arbitrarily chosen 5-degree polynomial equation is used to fit the whole 1D profile using Levenberg-Marquardt nonlinear curve fitting method. The raw 1D profile and fitted 5-degree polynomial curve of w_g-w_e = 50-50 and 5-100(μm) is plotted in Figure 3-10a and b.

The fitted value is subtracted from the raw data to obtain an offset height 1D profile and its differential values are calculated. In Figure 3-10c and d, one can clearly see peaks of Δy at electrode band and gap edges with a positive peak indicating the start of band area (or the end of gap area) and a negative one indicating the end (or the start of gap area). A threshold of ±5nm for the differential value is defined as the signaling value of the start or end of an electrode band (If Δy>5nm or Δy<–5nm, then that means a large rising or falling edge is encountered). In this way, it is able to precisely calculated the ratio of w_g and w_e even if the bands aren't initially placed perfectly perpendicular to the measuring direction. One can be confident to confirm that the bands are of heights 80±5nm, assuming that the bottom is totally flat. All the IDA electrodes are characterized and confirmed in this manner.

57
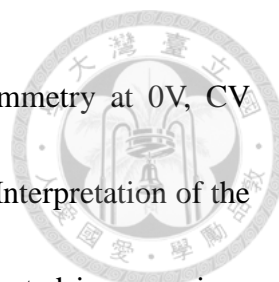
For examination of electrode functionality and potential symmetry at 0V, CV experiments are performed on all nine fabricated chips (Figure S1). Interpretation of the results are in supplementary data and have been extensively elaborated in a previous publication (Weng et al., 2019) for proving potential stability. The chips are confirmed to be symmetric with no structural flaws and damages.
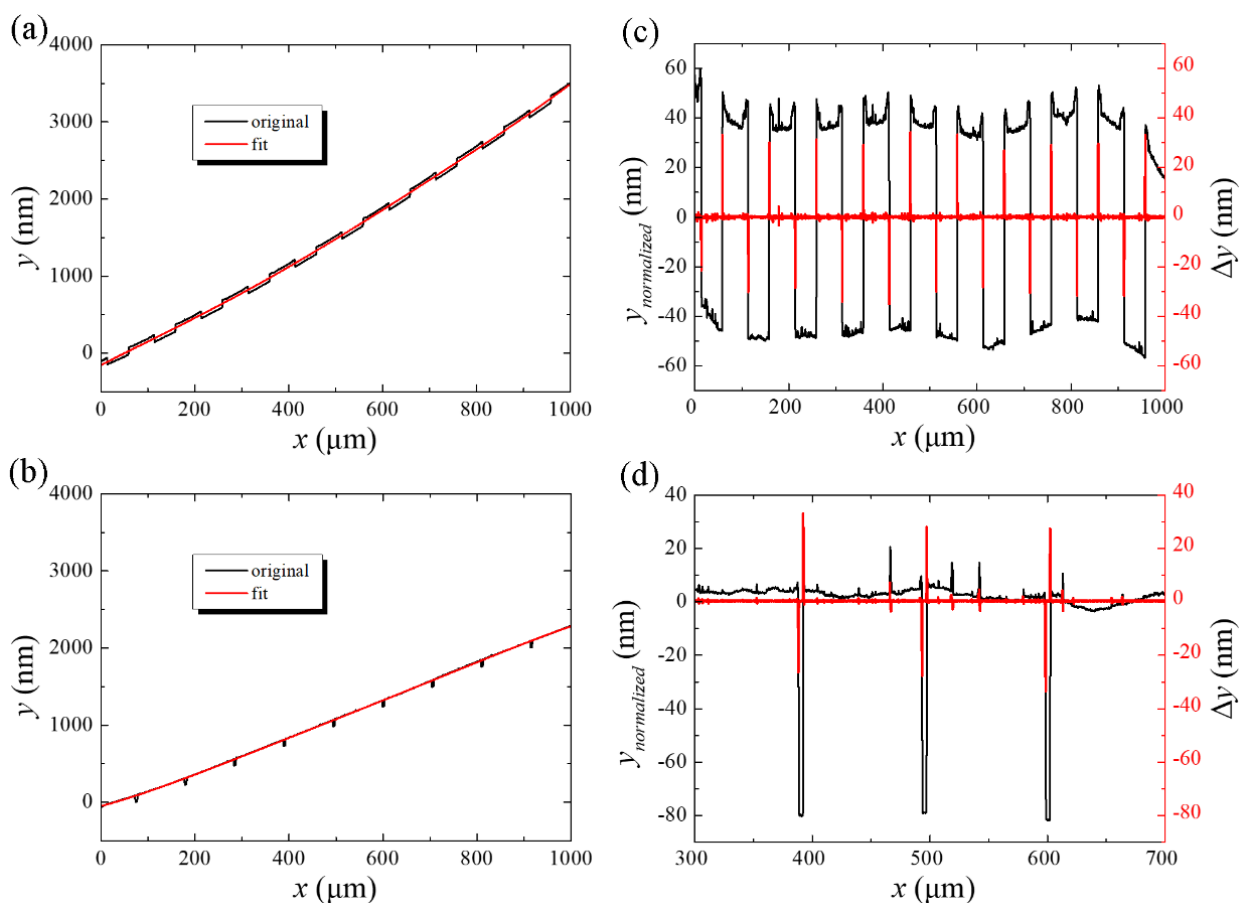
Figure 3-10 1D height (y) profile of IDA electrodes.
Original data and fitted 5-degree polynomial curve of (a) w_g-w_e=50-50, (b) 5-100(μm), and the normalized (original minus fit) and differential normalized data of (c) w_g-w_e=50-50 and (d) 5-100(μm). The differential normalized data is calculated by dividing one point of normalized data by its previous value ($\Delta y = y(x)–y(x+\Delta x)$).

58
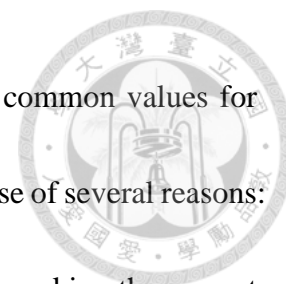
The collection efficiency and redox-cycling number are two common values for characterizing an IDA electrode. Those values aren't discussed because of several reasons: (1) The gap width and electrode bandwidth in this study is too large, making the current too small to keep the measurements accurate. (2) All the electrochemical measurements done in this study use the same two-electrode setup with both redox species appearing at the same time. Thus, measurements of collection efficiencies and redox-cycling numbers which only a reduced/oxidized species is appearing do not apply to the theory. (3) In-depth relationship between impedance, collection efficiency and redox-cycling number are still unclear and is beyond the scope of this study.

When performing electrochemical measurements, the height of solution should be high enough to cater to assumption V in the theory, that the solution above the electrode extends infinitely. Because any point on the surface of the electrode band can be linked to the imaginary constant concentration boundary (ICCB) using the cylindrical finite diffusion element, it is arbitrarily restricted that the solution height mustn't be lower than the height of the point on the ICCB which is linked to $x_e = 0.01(w_e/2)$. That means at least 99% of the points on the electrode can be linked to a point on the ICCB which is within the solution for the correspondence to the assumption. According to eqn. (12), as w_e becomes smaller, a higher solution shall be needed at constant w. Take $w_e/w = 0.1$ for example:

59

$$y_e\left(x_e = 0.01\left(\frac{w_e}{2}\right)\right)\Bigg|_{w_g/w_e=10} = 1.69w \quad (36)$$

That means if w_e-w_g=10-100(μm), a solution height of at least 185.9μm is needed to

ensure over 99% correctness of the finite diffusion calculations in the theory. Accordingly,

in the electrochemical experiments performed in this study, a constant solution height of

3mm is added for all IDA electrode geometries to ensure theoretical correctness.

3.4.3 Simulation of Time-Dependent 2D Concentration Profile in Unit Cell

From assumption IV, the originally unsteady-state perturbation of concentration has

reached a periodic-steady-state, which the concentration phasor $\widetilde{C}$ can be used for the

derivation of finite diffusion impedance. There are two problems arising from this

assumption: (1) When would the concentration reach periodic-steady-state? (2) Would

the concentration gradient be consistent with the derived finite diffusion length $L_d(x_e)$? In

order to answer these questions, simulation of time-dependent 2D concentration profile

in a unit cell using COMSOL Multiphysics for visualization and qualitative examination

is conducted. 2D time-dependent electroanalysis with diluted species C_O and C_R in a unit

cell is performed using the method explained in section 3.3.4. The overall setup of the

simulation corresponds to reality with one obstacle this study cannot overcome: the

setting is only allowed to sweep the voltage linearly among the electrode instead of

60

applying a sinusoidal voltage wave. This factor is neglected and the result is assumed to be close to what this study expects.

The time-dependent concentration profile is simulated from 0 to 2s with varying time steps. Due to eqn. (3), C_O and C_R are symmetric about the ICCB, so only C_O is plotted. Three-electrode configurations with a voltage sweep frequency of 3Hz, each with three arbitrarily chosen time points are shown in Figure 3-11. Colored contours of constant C_O concentration ranging from 4.5 to 5.5mM and red diffusive flux arrows which their lengths are proportional to the logarithm of absolute flux are plotted. The theoretically calculated constant concentration dashed line contours are stacked onto them. Qualitatively interpreting, one can almost observe the periodic-steady-state after a single period. So if the simulation is correct enough, an EIS experiment can be done in one or two cycles and one needn't to be worried about the measurement accuracy.
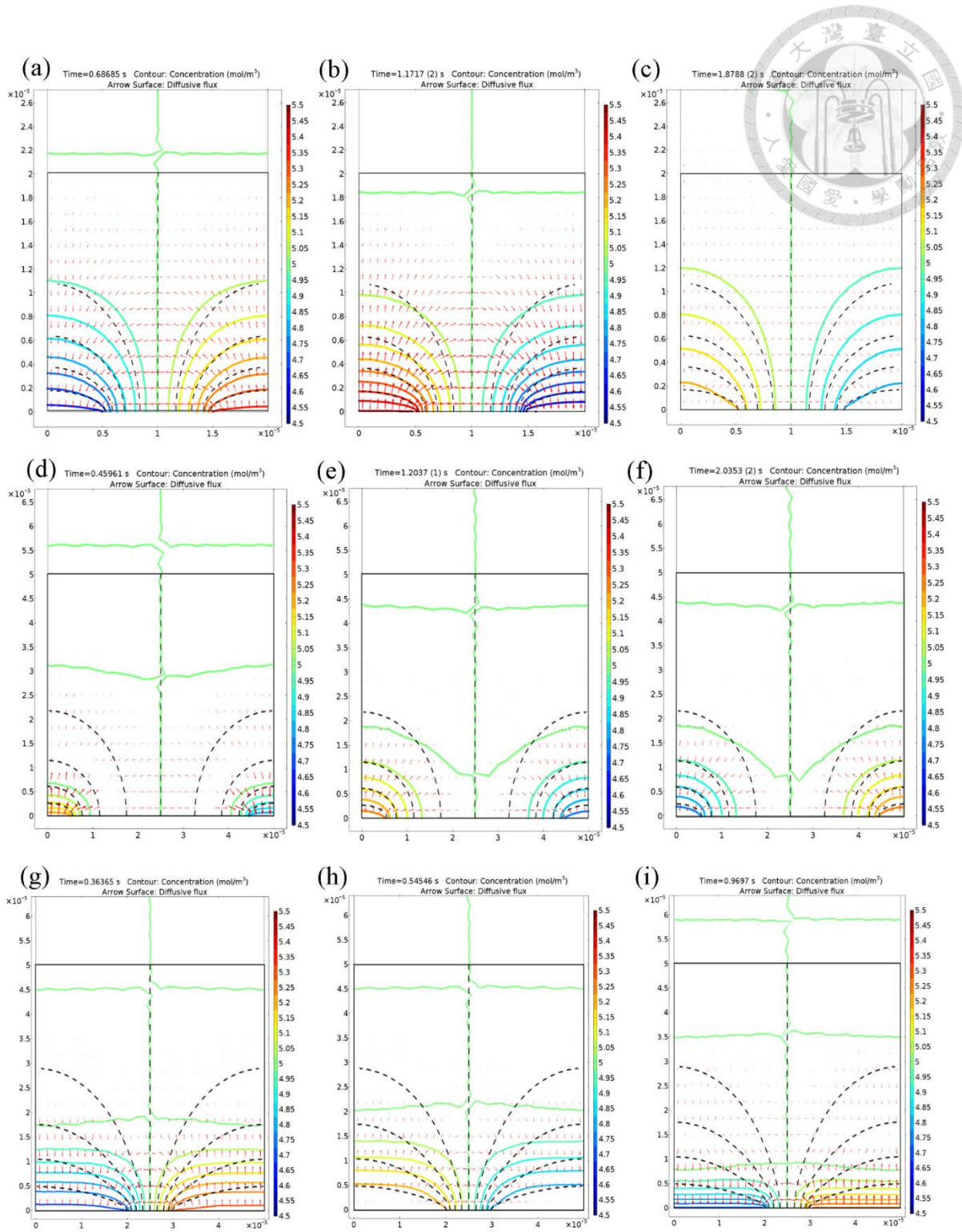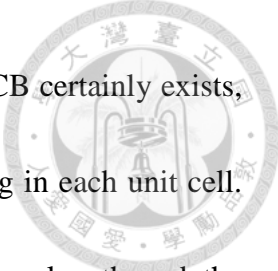
Figure 3-11 Simulation of time-dependent 2D concentration profile in an IDA unit cell. w_e-w_g = (a)~(c) 10-10, (d)~(f) 40-10 and (g)~(i) 10-40 (μm). The colored lines are simulated constant concentration contours and the black dashed lines are the predicted contours.

From Figure 3-11, one is able to directly point out that the ICCB certainly exists, which also points out the concentration and flux symmetry appearing in each unit cell. This is a major boundary condition for deriving the finite diffusion length and the cylindrical finite diffusion impedance. The flux drawn beside the ICCB indicates that redox species do flow across the ICCB, but there exists dynamic equilibrium and that redox species only flow perpendicular to it. The concentration flux is almost in vertical direction at the left and right boundary of the unit cell. This is in consistency with this theory, that redox species don't flow outside the unit cell boundary and the unit cell can really represent behavior of two lateral halves of electrode bands. There might be two possible extensions that can be regarded as future work: (1) Considering asymmetrical configurations of electrode bands, this study expects that the ICCB would still exist. But it mustn't be a straight line and the asymmetric distribution of potential among the electrodes would probably have a significant result on the periodic-steady-state concentration. (2) The ICCB is expected to still be at $\text{Re}(z) = w/2$ for finite heights of solution. But what would happen when convection forces are applied in microfluidic systems? A model with the additional height and velocity parameter must be derived.

Even if the periodic-steady-state is proven to exist, the ever-changing contour shapes show that the approach for deriving a static constant concentration contour will never succeed in EIS measurements. From the contours, one can see qualitatively that

63
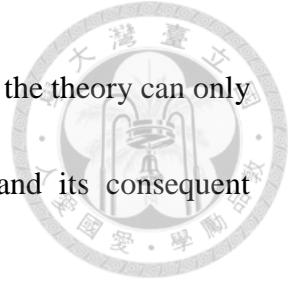
redox species will not always flow within the same path. That means the theory can only

approximate the true nature of diffusive flux of redox species and its consequent

impedance.

Simulated concentration profiles between w_g-w_e=10-10 (Figure 3-11a, b and c), 40-

10 (Figure 3-11e, d and f) and 10-40(μm) (Figure 3-11g, h and i) are qualitatively

compared. When w_g-w_e=10-10(μm), the contours are more consistent with the dashed

lines compared with those of w_g-w_e=10-40(μm), but less consistent compared with those

of w_g-w_e=40-10(μm). Which means the less the gap width compared with the electrode

bandwidth, the more the distortion it may happen. According to the theory, for every point

on the left half of the gap (x_g, 0) (w_e/2 < x_g < w/2), there must exist another point on the

left boundary (0, y_g) that has the same concentration as the point on the gap. The fact that

the left and right boundary extends infinitely upward should cause serious distortion when

w_g is comparatively small. This also indicates the finite diffusion length at $x_e \rightarrow 0$ for a

small gap width will be erroneously predicted by the theory. Therefore, the definition for

the ICCB needs to be modified for more generalized geometries.
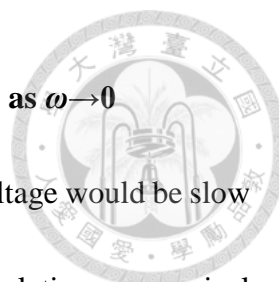
3.4.4 Comparison of Limiting Current and Calculated Impedance as $\omega \to 0$

A special case of impedance arises as $\omega \to 0$. The change of voltage would be slow enough for the concentration and current to reach steady-state. Simulations, numerical and analytical solutions of CV and CA have already been extensively researched for different geometries of IDA electrodes (Aoki, 1990; Yang and Zhang, 2007). It is thus necessary to prove that the equations are consistent with recent studies.
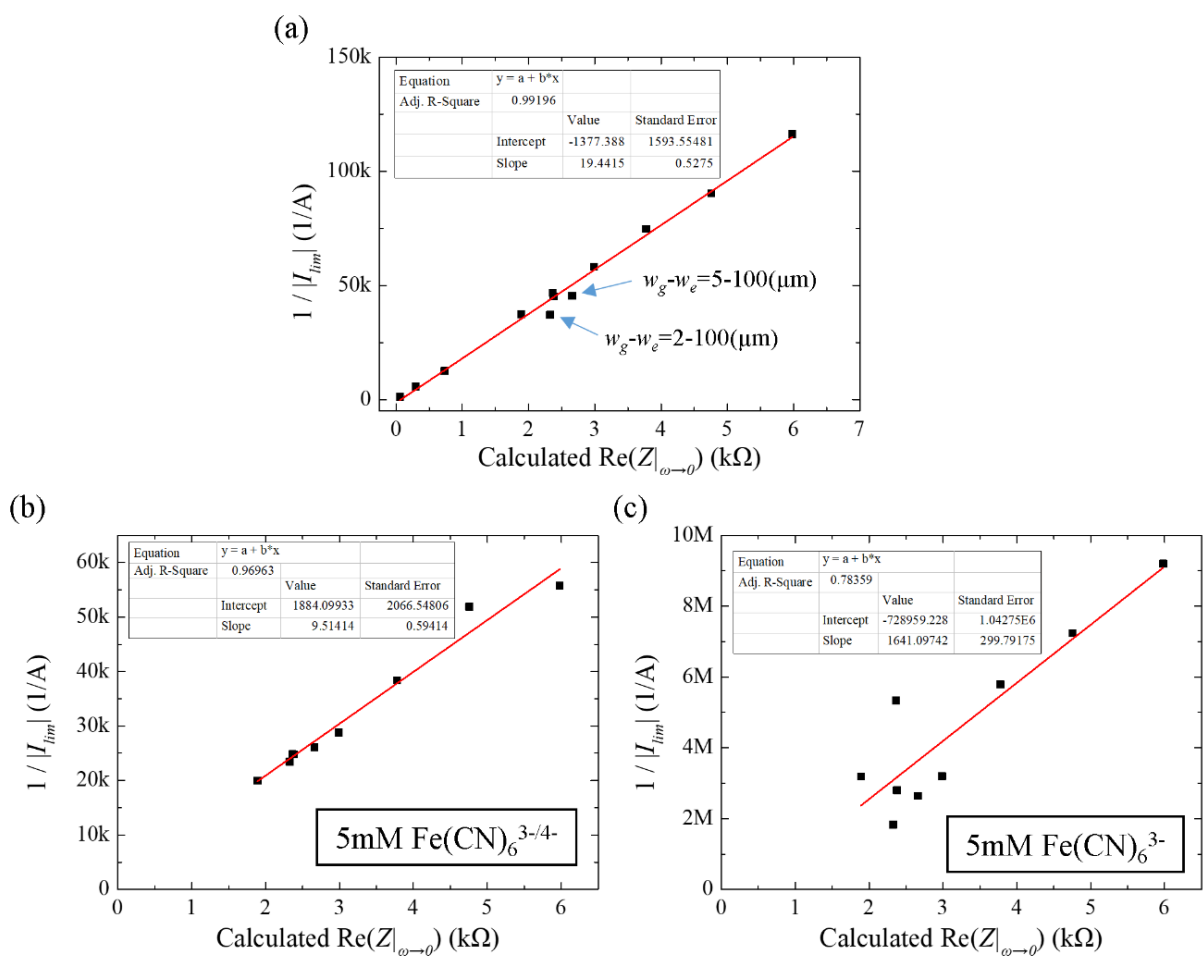
Figure 3-12 The reciprocal of limiting current plotted against the calculated real part of IDA diffusion impedance at $\omega \to 0$. $|I_{lim}|$ is (a) the absolute value of limiting current calculated from eqn. (38) in Aoki et al.'s work (Aoki et al., 1988), or the current at 10s when applying a voltage of –0.2V (vs CE/RE) in a solution containing 0.1M KCl and (b) 5mM $Fe(CN)_6^{3-/4-}$ or (c) 5mM $Fe(CN)_6^{3-}$ in a chronoamperometry experiment.

65
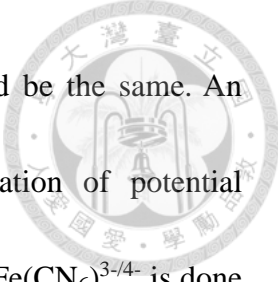
Figure 3-12a plots the reciprocal of the limiting current calculated from eqn. (38) derived in Aoki et al.'s work (Aoki et al., 1988) against the real part of impedance at $\omega \to 0$ calculated from eqn. (28). Different w_g and w_e ranging from 1 to 100μm are randomly assigned. The result of the calculations shows a high correlation ($R^2 = 0.992$) with their work. That means if one is to simplify these equations at the limit of $\omega \to 0$, he or she would arrive at an equation inversely proportional to their limiting current. Unfortunately, efforts for finding an analytical simplified solution made up with only elementary functions has encountered difficulties. Nevertheless, the meaning of this result is significant in different aspects: (1) The result has proven the hypothesis of cylindrical finite diffusion impedance from the ICCB to the electrode valid under low frequencies. (2) One is able to degrade the equations and calculate the limiting current using the derived theory. (3) The theory can be thought of as a novel method for interpreting IDA electrode behavior that further extends steady-state to periodic-steady-state research fields. (4) The ICCB assumption leads to accurate enough results, making an evidence for its existence. Microfluidic systems with finite height and convection forces can also follow relevant assumptions for deriving solutions for the diffusion impedance. In Figure 3-12a, there are two points lower than the regression line, which are the calculated values when w_g-w_e = 2-100 and 5-100(μm). This indicates a possible failure of the theory when w_g/w_e is small (< 0.1) and corresponds to the simulation results. (Note that the diffusion

66

coefficient taken into calculation is $D = 6 \times 10^{-10} \text{m}^2/\text{s}$. This is arbitrarily defined due to

various values obtained ($(6 \pm 3) \times 10^{-10} \text{m}^2/\text{s}$) using CV and Randles-Sevcik equation in this

work (Figure S2) and a previous one by the authors team (Weng et al., 2019).)

With the above advantage in grip, one can be confident that calculation of the

steady-state current is of correctness to a certain degree. Figure 3-12b plots the reciprocal

of steady-state current using different geometries of IDA electrodes in a solution

containing 5mM $Fe(CN_6)^{3-/4-}$ and 0.1M KCl against the calculated real part of impedance

at $\omega \rightarrow 0$. The steady-state current is obtained using chronoamperometry and raw data is

plotted in Figure S3. The calculated value has a correlation of $R^2 = 0.970$ with the

experimental value, which once again verified the accuracy of the theory at steady-state.

Note that calculating the impedance by dividing the applied voltage with the limiting

current is meaningless, because at diffusion controlled circumstances the relation between

the voltage and current is non-linear. Linearity only exists at small voltages. In order to

calculate the limiting current using the equations, the proportional constant between the

impedance and the reciprocal of limiting current should be pre-calculated using the fitted

linear equation. The slope of Figure 3-12b suggests that a proportional constant of

9.51(1/AΩ) can be determined when the limiting current is obtained by applying a -0.2V

(vs CE/RE) using chronoamperometry.

Due to the geometric symmetry, concentration symmetry and the concept of the

67

ICCB, the standard electrode potential of the two electrodes would be the same. An additional experiment using standard Au electrodes for examination of potential symmetry of a two-electrode setup in equal molar concentrations of $Fe(CN_6)^{3-/4-}$ is done (Figure S4). With CE/RE playing the role of pseudo-reference, the reactions are the same at WE and CE/RE.

Linear correlation results in the absence of $Fe(CN_6)^{4-}$ is also obtained (Figure 3-12c). The bigger noises might be caused by invalid conditions of assumption II and the significantly smaller current being measured. In this configuration, only when the generated reduced species have flown across the gap and taken by the collector can there exist a current. So a great enhancement in sensitivity at steady-state can be achieved when both redox species are present. In a nutshell, the steady-state currents predicted by the theory is valid in presence of both redox species.

68

3.4.5 Comparison of Experimental EIS Data and Theoretical Impedances

According to the theory, geometrical parameters of IDA electrodes can be verified

in situ using EIS data. To obtain direct evidence of the correctness of the theory, the

experimental EIS data and the theoretically calculated impedances are compared.

Because all the necessary parameters such as C^* and w_g are known, so eqn. (28) can

directly calculate every single value of impedance with a given frequency and plot them

on a Nyquist plot along with experimental values.

In order to compare the calculated and experimental values, impedances that do not

arise from diffusion need to be eliminated. The solution resistance (R_s), charge transfer

resistance (R_{ct}) and double layer capacitance (Q_{dl}) (i.e., C_{dl}) (Shoar Abouzari et al., 2009)

must be eliminated from the experimental value in advance. A common Warburg element

cannot be used for modeling the low frequency area because the impedance would bend

towards the real axis and the initial angle wouldn't perfectly be 45°. Therefore, another

CPE had to be used for modeling of low frequency impedances. Moreover, only a certain

range of frequency before the bending can be fit accurately enough. Thus, the circuit

$R(Q(RQ))$ is arbitrarily chosen for experimental data fitting, which is equivalent to a

Randles circuit using a CPE for characterizing the diffusion impedance. (This circuit

description code is defined to express equivalent circuits. Elements, including whole

blocks inside parentheses, are either in series or parallel with each other. Those inside an

odd number of pair of parentheses are in parallel with each other, and those inside an even

number of pair of parentheses are in series.) A frequency range of $1 \sim 10^5$Hz is chosen for

fitting rather than the frequency range used in EIS ($10^{-2} \sim 10^5$Hz). Figure 3-13a plots the

raw EIS data of w_g-w_e = 100-50(μm) and its fitted data using the above method. This

serves as an example of how one can extract only the diffusion impedance out. It can be

seen that the circuit can accurately fit the raw data for finding R_s, R_{ct} and Q_{dl}. These three

parameters are subtracted from the impedance using complex number calculations

according to their series and parallel relationship. At last, impedances of EIS data having

values only influenced by diffusion effects are obtained. All the EIS data are modified

using this procedure.
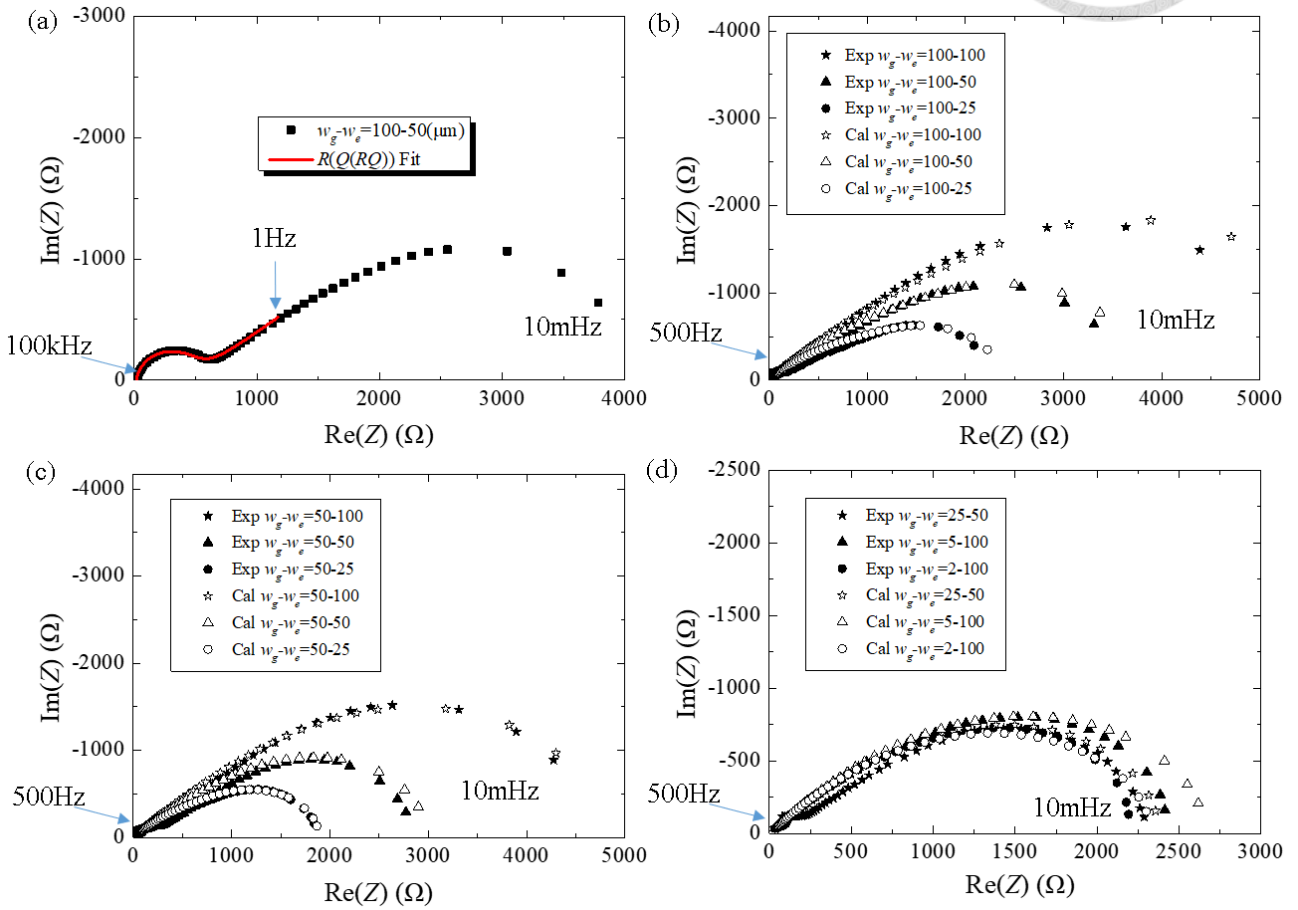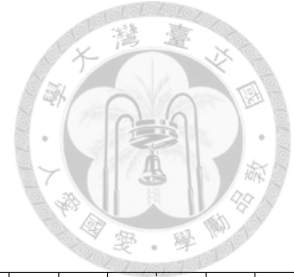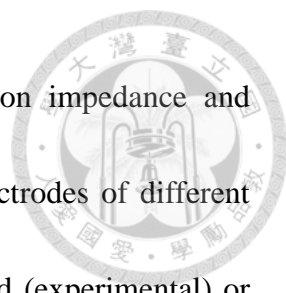
Figure 3-13 (a) Nyquist plot of experimental EIS data of an IDA electrode (w_g-w_e = 100-50(μm)) and its equivalent circuit fitted data. The frequency range of the experimental data is $10^{-2} \sim 10^5$Hz and the frequency range used for fitting is $1 \sim 10^5$Hz. The subfigure at the top-left is the circuit being fitted and is equivalent to $R(Q(RQ))$, which is a typical Randles circuit using a CPE for characterizing the diffusion impedance. (b ~ d) Nyquist plot of experimental (solid) and calculated (hollow) IDA diffusion impedances at (b) w_g = 100, (c) w_g = 50 and (d) $w_g \leq$ 25. The frequency range of all the data is $10^{-2} \sim 10^5$Hz. The unit for widths is μm.

71

The modified experimental EIS data with only the diffusion impedance and calculated values are plotted on the Nyquist plot for nine IDA electrodes of different geometries (Figure 3-13b~d), which are illustrated as different solid (experimental) or hollow (theoretical) shapes. Experimental values of impedances below 547Hz are compared with theoretical results. The reason for not taking impedances at high frequencies is because their significantly small values due to non-diffusion controlled reactions and that a slight difference of the parameters found from fitting would cause huge proportional errors of them. Calculated values are obtained from a self-written program, which is provided in supplementary material. It must be again stressed that the calculated impedances are not values obtained from any fitting program according to the experimental data, but rather calculated directly from T, w_e, w, D, l, N, n, C^* and ω. A high likeliness can be seen between the experimental and calculated values. This result can serve as the direct evidence for the effectiveness and precision of the theory and IDA diffusion impedances can be approximated accurately from eqn. (28). Overall, as w_g/w_e increases, the phase angle before the bending at very low frequencies becomes much smaller than 45°. As w_g/w_e decreases, the phase angle becomes closer to 45° before bending towards the real axis and forming an imperfect semi-circle. This is reasonable and can be seen from Figure 3-8. At very low frequencies, the curves bend toward the real axis and a steady-state impedance or current can be found. Note that the total area of

72

electrode lNw_e are all of the same value (6mm^2) in every chip that have been fabricated.

High correlations between experimental and theoretical IDA diffusion impedances are obtained ($R^2 \geq 0.948$) with the real part and imaginary part individually calculated.

When w_g-w_e = 5-100 and 2-100(μm), it can be seen that the calculated impedances separate from the experimental data at low frequencies. Thus, at $\omega \rightarrow 0$, the real part of impedance will be overestimated by the theory, which further indicates that it may fail when $w_g \ll w_e$ at low frequencies. This is relevant to what this study had discussed in section 3.4.4, that the two points in Figure 3-12a are obviously lower than the regression line and are overestimated. According to the simulation results in section 3.4.3, this failure arises from erroneous constant concentration contours and finite diffusion length calculations. So if more extreme impedance values are needed to be calculated when $w_g \ll w_e$, the definition for the ICCB should be modified, which is another future work worth of study.
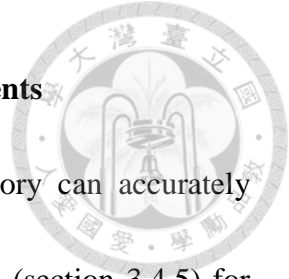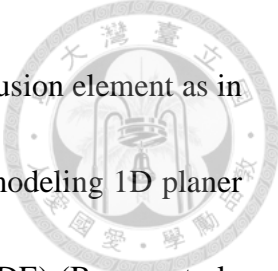
3.4.6 EIS Data Fitting using Different Diffusion Impedance Elements

From the above results, one can be confident that the theory can accurately approximate the limiting current (section 3.4.4) and the impedance (section 3.4.5) for diffusion of redox species of IDA electrodes at $w_g/w_e > 0.1$. In this section, an equivalent circuit element is constructed for EIS data fitting of the diffusion impedance of IDA electrodes and its accuracy and effectiveness with other circuit elements are compared. A program for equivalent circuit fitting is written in advance. The program implements a complex nonlinear least square (CNLS) process (Lasia, 2002), which the weighted sum of squares of error, S, is defined as

$$S = \sum_{i=1}^{N_f} \left[w_{i,\mathrm{Re}} \big(\mathrm{Re}(Z_{i,cal}) - \mathrm{Re}(Z_{i,exp}) \big)^2 + w_{i,\mathrm{Im}} \big(\mathrm{Im}(Z_{i,cal}) - \mathrm{Im}(Z_{i,exp}) \big)^2 \right] \quad (37)$$

where N_f is the number of frequencies within an experiment, Z_i is the impedance of the i–th frequency, and $w_{i,\mathrm{Re}}$ and $w_{i,\mathrm{Im}}$ are the statistical weights for the real and imaginary parts of the impedance of the i–th frequency. The subscript *exp* indicates experimental value and the subscript *cal* indicates the calculated value while fitting. A weighting of $w_{i,\mathrm{Re}} = 1/|\mathrm{Re}(Z_{i,exp})|$ and $w_{i,\mathrm{Im}} = 1/|\mathrm{Im}(Z_{i,exp})|$ is chosen for fitting of parameters. A Levenberg-Marquardt algorithm is used for minimization of S, which is provided by ALGLIB.

Three other diffusion elements are compared with the IDA diffusion element as in Table 3-1. The open finite-length diffusion element is common for modeling 1D planer finite diffusion systems such as the rotating ring-disk electrode (RRDE) (Barnes et al., 2012). This element exhibits a 45° line at high frequencies and a semi-circle at low frequencies on the Nyquist plot. Because 2D finite diffusion exists in an IDA electrode system, so the initial phase angle would be slightly lower that 45° and a somehow imperfect semi-circle would appear (cf. Figure 3-8). Thus a parameter n is introduced into the open finite-length element for better fitting, and this new element is arbitrarily named as the "CPE finite-length diffusion" element. This n has the same effect as in the CPE and can further help reducing the minimum S when fitting. For convenience, the symbol for the CPE finite-length diffusion element is set as "X" and the IDA diffusion element is set as "I".

Table 3-1 Equivalent circuit elements for diffusion impedance.
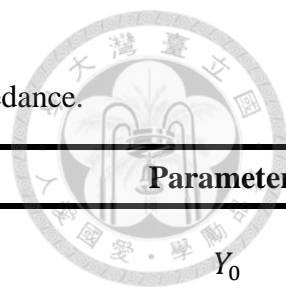
Element Name	Symbol	Value	Parameters
Warburg	W	$Z_W = \dfrac{1}{Y_0\sqrt{j\omega}}$	Y_0
Open finite-length diffusion (Warburg Open)	O	$Z_O = \dfrac{1}{Y_0\sqrt{j\omega}}\tanh(\dfrac{\delta}{\sqrt{D}}\sqrt{j\omega})$	Y_0 and $\dfrac{\delta}{\sqrt{D}}$
CPE finite-length diffusion	X	$Z_X = \dfrac{1}{Y_0(j\omega)^n}\tanh(\dfrac{\delta}{\sqrt{D}}(j\omega)^n)$	$Y_0, \dfrac{\delta}{\sqrt{D}}$ and n
IDA diffusion	I	eqn. (28)	$Y_0, \dfrac{w_e}{w}$ and $\dfrac{w^2}{D}$

All nine IDA electrode chips are washed thoroughly, clipped with microwells and added with the solution used for electrochemical characterization. EIS experiments are performed and each chip is analyzed using a single EIS data. Nyquist plots of three of them (w_g-w_e = 100-25, 50-50 and 2-100(μm)) along with fitted results using the four elements are shown in Figure 3-14. Obviously, the Warburg element fails to work, making the fitted data yield parameters with large errors (Figure 3-14a). The open finite-length diffusion element obtains a better fit (Figure 3-14b). The semi-circle can approximately match the down-bending curve of the IDA electrode's diffusion impedance. However, the IDA diffusion impedance isn't really a perfect semi-circle (cf. Figure 3-8). It is somehow longer in the horizontal direction, especially when w_g/w_e becomes larger. Nevertheless, this element can be regarded as the minimum required one for characterizing an IDA electrode. The CPE finite-length diffusion element fits the data even better (Figure 3-14c).

76
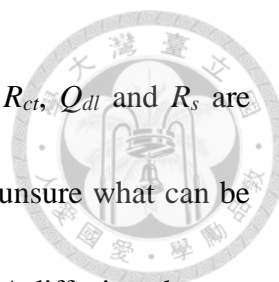
Using this element, one can be confident that parameters such as R_{ct}, Q_{dl} and R_s are correctly fitted to a generally satisfying degree. However, it is still unsure what can be told from the two parameters $\delta/\sqrt{D}$ and n. The fitting result of the IDA diffusion element from the theory is also accurate (Figure 3-14d), and the parameters Y_0, w_e/w and w^2/D can be extracted from it.
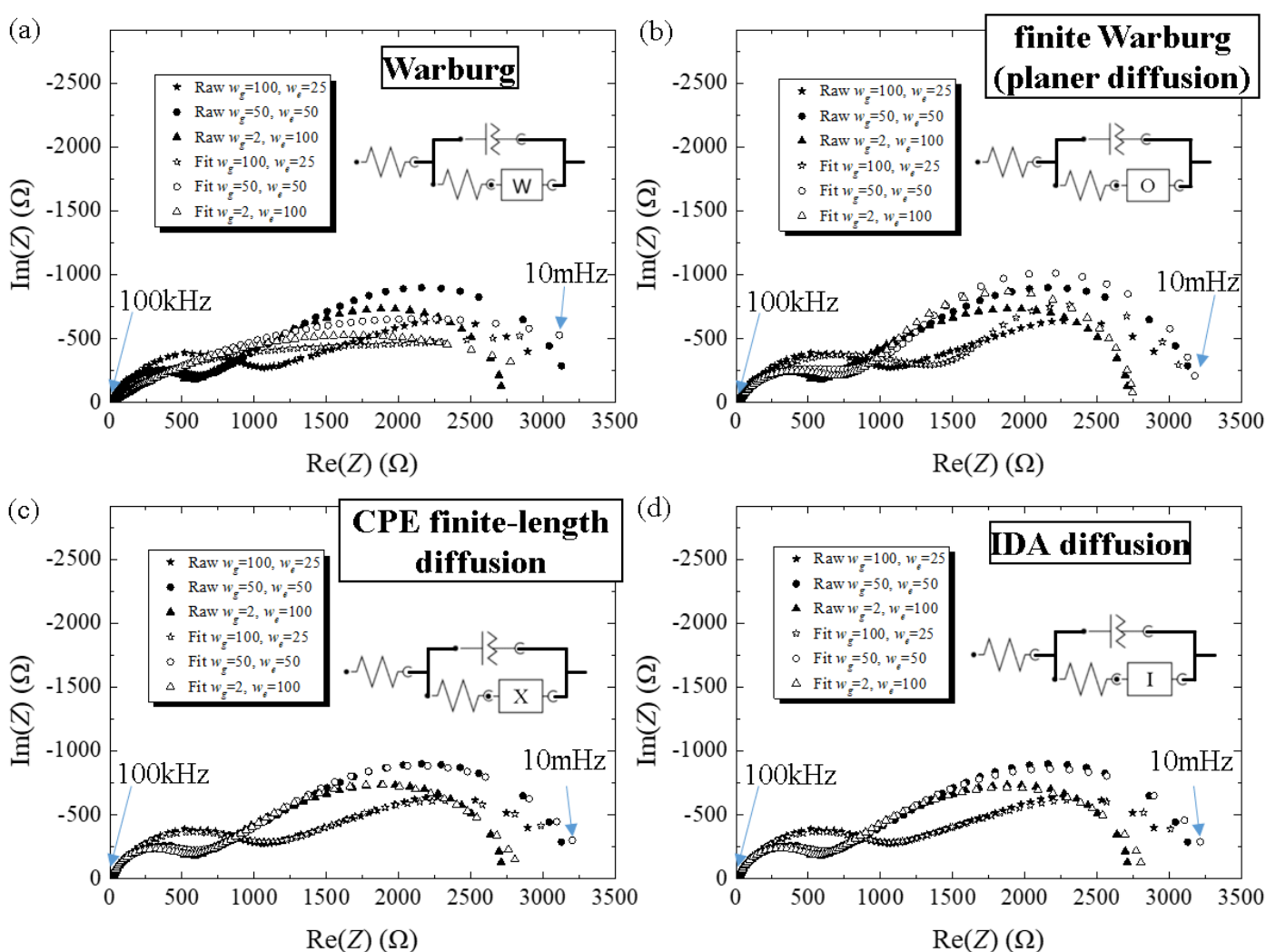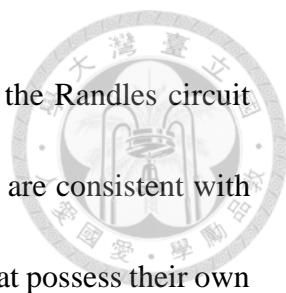
Figure 3-14 Raw and fitted EIS data of three bare IDA electrode chip with the Randles circuit using different elements for diffusion impedance modeling. (a) Warburg element, (b) open finite-length diffusion element, (c) CPE finite-length diffusion element and (d) IDA diffusion element. The frequency range of all the data is $10^{-2} \sim 10^5$ Hz. (units: μm)

Table 3-2 Equivalent circuit fitting results for nine IDA chips using four different diffusion impedance elements.

w_g (µm)	100	100	100	50	50	50	25	5	2
w_e (µm)	100	50	25	100	50	25	50	100	100

$R(Q(RW))$ (W : Warburg element)

R_s	1.14µ	88µ	0.649µ	1.72µ	0.284µ	0.117µ	6.98m	202µ	93.7µ
Q_0	302µ	276µ	82.1µ	234µ	214µ	138µ	153µ	174µ	163µ
n	0.33	0.343	0.46	0.353	0.397	0.422	0.442	0.394	0.403
R_{ct}	15.2k	6.23k	2.23k	8.77k	3.98k	2.45k	2.92k	3.46k	3.15k
Y_0	19.6	594	3.73m	65.4k	34.7M	19.2m	769	9.20k	12.1k

($R_s[=]R_{ct}[=]\Omega$, $Q_0[=]s^n/\Omega$, $n[=]$none , $Y_0[=]s^{1/2}/\Omega$, $\delta/\sqrt{D}[=]s^{1/2}$)

$R(Q(RX))$ (X : CPE finite-length diffusion element)

R_s	30.9	21.5	13.4	28.6	16.7	11.9	15.3	20.6	19
Q_0	995n	778n	4.91µ	1.11µ	2.57µ	2.11µ	2.20µ	668n	965n
n_Q	0.965	0.953	0.788	0.929	0.886	0.875	0.898	0.966	0.939
R_{ct}	515	430	857	489	488	604	404	406	432
Y_0	463µ	512µ	742µ	403µ	525µ	642µ	447µ	440µ	457µ
$\dfrac{\delta}{\sqrt{D}}$	2.69	1.96	1.87	2.02	1.49	1.25	1.02	1.17	1.1
n_X	0.403	0.377	0.326	0.398	0.403	0.367	0.41	0.399	0.398

w_g (µm)	100	100	100	50	50	50	25	5	2
w_e (µm)	100	50	25	100	50	25	50	100	100

$R(Q(RO))$ (O : Open finite-length diffusion element)

R_s	34	4.1	6.28	9.83	8.57	4.77	7.44	21.8	6.15
Q_0	3.43µ	14µ	17.9µ	15.7µ	14.9µ	8.77µ	13.9µ	3.82µ	8.9µ
n	0.825	0.639	0.635	0.633	0.685	0.714	0.693	0.787	0.696
R_{ct}	803	835	1350	966	803	904	699	642	727
Y_0	554µ	634µ	1.16m	477µ	605µ	782µ	487µ	477µ	504µ
$\dfrac{\delta}{\sqrt{D}}$	2.72	1.94	2.02	2.01	1.44	1.19	0.931	1.07	1.01

$R(Q(RI))$ (I : IDA diffusion element)

R_s	29.3	19.5	13.1	26.6	16	12.4	15.3	19.3	17.8
Q_0	1.53µ	1.28µ	5.40µ	1.92µ	3.18µ	2.04µ	2.39µ	1.02µ	1.41µ
n	0.918	0.903	0.779	0.872	0.864	0.88	0.891	0.923	0.901
R_{ct}	621	531	967	621	557	635	448	485	508
Y_0	769µ	739µ	902µ	654µ	809µ	701µ	640µ	664µ	681µ
$\dfrac{w^2}{D}$	65.2	28.3	30.6	33	16.9	9.73	7.19	12.1	10.7
$\dfrac{w_e}{w}$	0.615	0.472	0.248	0.697	0.761	0.321	0.788	0.902	0.907

The fitted parameters obtained using all four elements inside the Randles circuit are shown in Table 3-2. The results using the IDA diffusion element are consistent with the experimental plot in that all parameters hold a reasonable range that possess their own physical meanings. The average weighted sum of squares (S/N_f) for each element and chip are shown in Figure 3-15a. This is also the mean square error (MSE) of the fitting result. Different elements have different magnitudes of errors and all fall in a certain range. The IDA diffusion element has an average MSE of 0.611. Compared to the Warburg element (average MSE = 54.86), this proves the effectiveness of the theory applied for equivalent circuit fitting. The coefficient Y_0 is calculated in advance using theoretical values, and it is compared with the fitted values (Figure 3-15b). The errors have an average of $3.77\times10^{-5}\text{s}^{1/2}/\Omega$ and the standard deviation is $8.11\times10^{-5}\text{s}^{1/2}/\Omega$. These errors might be caused by temperature fluctuation, uneven active electrode areas, bulk concentration changes, or the fitting bias itself. Fitted values of w^2/D and w_e/w are plotted against calculated values (Figure 3-15c and d). The fitted values for w^2/D show a high correlation with the calculated values ($R^2 = 0.940$). With a known w or D, one is able to determine the other value. The correlation between the fitted values and calculated values of w_e/w has a lower value ($R^2 = 0.869$). This suggests a more difficult attempt for finding this ratio using EIS data. The reason might arise from the fact that the shapes of the diffusion impedance look more similar and get closer to each other as w_g/w_e becomes smaller (cf. Figure 3-8).

79
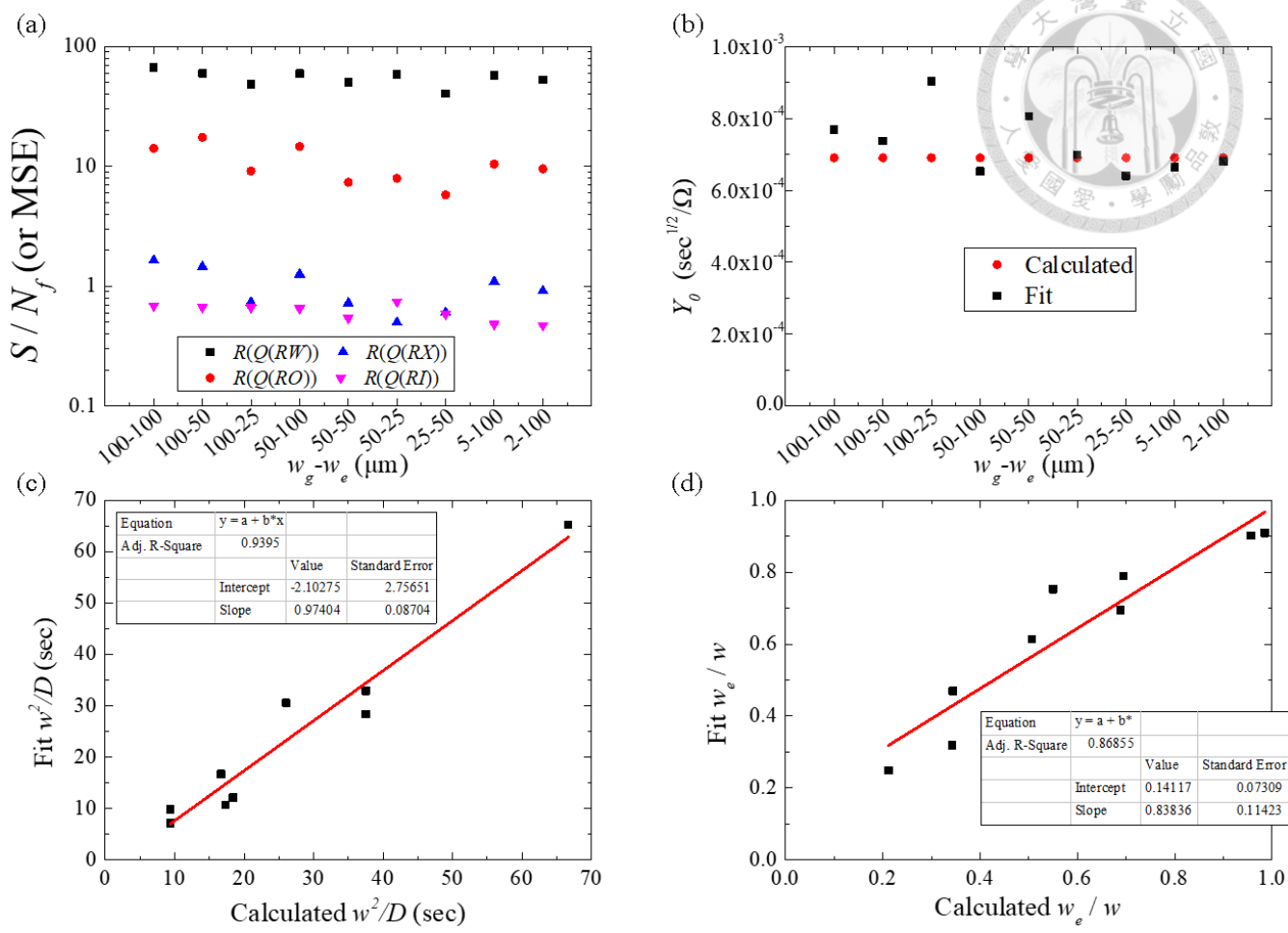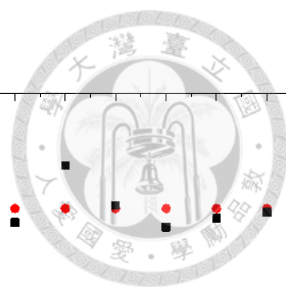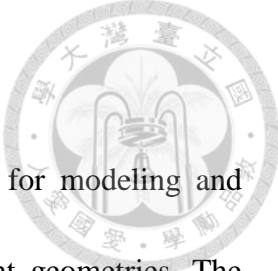
Figure 3-15 (a) S/N_f (or MSE) of the fitting results for the nine IDA electrode chips using different diffusion impedance elements. (b) Calculated and fitted values of Y_0 from the nine chips. (c) Fitted value of w^2/D against its calculated value. (d) Fitted value of w_e/w against its calculated value.

The results above show the accuracy and the effectiveness of the theory applied for equivalent circuit modeling for the EIS data of IDA electrodes. The data from a single EIS experiment is enough for finding Y_0, w^2/D and w_e/w. This solves the problem for erroneous parameter acquisition when using elements that cannot express the diffusion nature of IDA electrodes. This also proves that it is able to verify certain parameters *in situ* and even predict unknown geometries.

80

3.5 Summary

In summary, a novel integral form of solution is presented for modeling and calculating the diffusion impedance for IDA electrodes of different geometries. The theory is based on conformal mappings, diffusion length derivation and cylindrical finite diffusion impedance approximation. According to the derived equations, an impedance calculation program is designed and released for helping researchers predict the diffusion impedance of their own IDA electrode system. The calculated real part of impedance at zero frequency showed high correlation with the reciprocal of limiting current calculated by Aoki et al.'s results ($R^2 = 0.992$) and from chronoamperometry experiments ($R^2 = 0.970$). Experimental EIS data and calculated impedances are highly alike ($R^2 \geq 0.948$). Thus, direct evidence for correctness of the theory is established. An equivalent circuit fitting program is further designed for fitting several elements including the IDA electrode diffusion impedance. The program succeeded to fit the EIS data which the Warburg element would have failed. Therefore, researchers can accurately obtain R_{ct}, Q_{dl} and other parameters or even predict unknown geometries. The proposed solution can also assist them model their data and understand the underlying mechanism more correctly, hoping that it can furthermore mature the theoretical basis of this advantageous sensing architecture.

Chapter 4

EIS Modeling of Symmetric Electrodes for Aptasensing

4.1 Brief Introduction

In Chapter 3, an integral form of solution for approximating the diffusion impedance for IDA electrodes is proposed. Thus, it provides a more general method for fitting their EIS data containing the low frequency spectrum. In this chapter, the parameter relationship between a single and symmetric Randles circuit is derived, and is applied for impedimetric aptasensing of the target proteins using symmetric Au electrodes.

Mucin-1 (MUC1) is a transmembrane protein which overexpresses on certain cancer cell surfaces and ranks the second in the cancer antigen pilot prioritization, making it an ideal tumor marker for cancer diagnosis (Cheever et al., 2009) (Figure 4-1). Although there have been a number of works demonstrating promising integration of impedimetric biosensors in microfluidic biochips (Table 2-1), the tedious three-electrode fabrication and lack of an efficient method for selective deposition of antibodies on the WE have hindered EIS biosensors for realistic microscale and multiplex bioanalysis. In this chapter, a novel fabrication-favorable EIS approach for detection of MUC1 using simply two symmetric aptamer-modified standard Au electrodes is investigated. The Randles equivalent circuit for a two symmetric electrode system is derived to have certain

proportional association with a common Randles circuit. A proof of theory experiment

for this derivation is also conducted. The enzyme thrombin (Bock et al., 1992) is firstly

used as the detection target for verifying the effectiveness of impedimetric aptasensing

with the two electrode setup. Afterwards, detection of MUC1 is conducted with two and

three electrode setups and the results are compared. The results should be compatible with

the theory for denoting that this study has developed a method for analyzing two electrode

setups applied for impedimetric aptasensing. At last, a combination of theory from

Chapter 3 and Chapter 4 is applied for analyzing an impedimetric aptasensor using IDA

chips for regenerable and specific detection of thrombin.
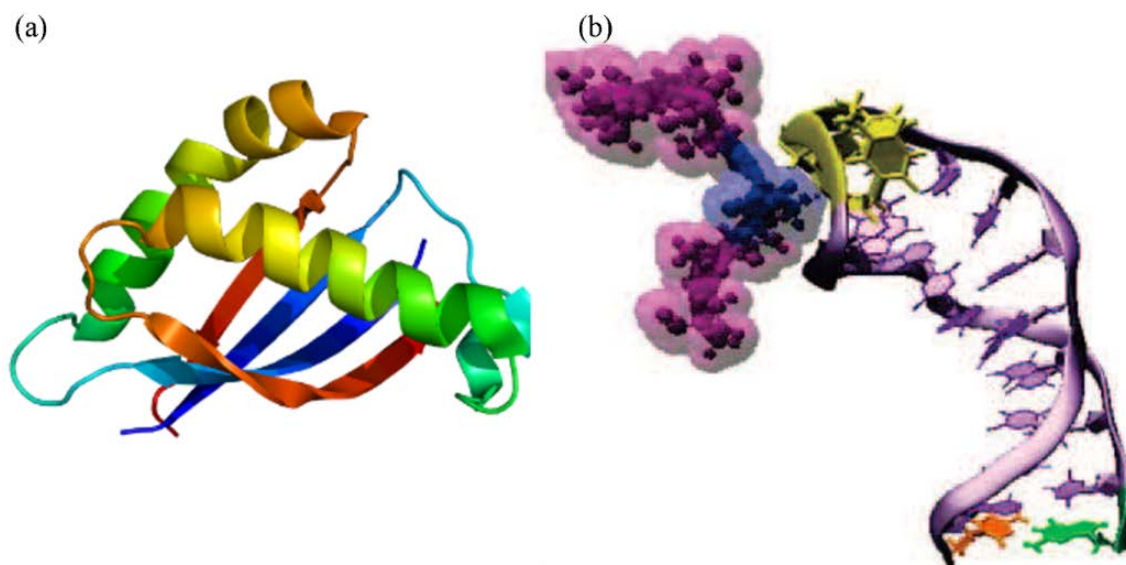
Figure 4-1 (a) Structure of MUC1. PDB ID: 1SM3 (b) Final conformation of the MUC1-
G peptide and S2.2 aptamer interaction (Rhinehardt et al., 2015).

4.2 Theory

In this section, a novel equivalent circuit model is design and justified to analyze the symmetric Au electrode system and an algorithm for fitting the Randles circuit is developed. A brief introduction of the Randles circuit and its related components is carried out, then the details for equivalent circuit model theory and calculation are explained.

4.2.1 Impedance Calculation for the Randles Circuit

In EIS, the equivalent circuit of an electrochemical cell refers to a theoretical circuit that retains all or part of the its electrical characteristics resulted from mass transfer kinetics or surface electrochemical reactions. There are many factors that may have an impact on the electrochemical behavior on an electrode surface, which lead to various equivalent circuits proposed in order to explain the basal phenomenon and the resulting experimental data obtained by EIS (Yuan et al., 2010). A typical one is the Randles circuit, which comprises a solution resistance (R_s), double layer capacitance (C_{dl}), charge transfer resistance (R_{ct}) and Warburg element (the semi-infinite diffusion impedance, Z_W) (Lasia, 2002) as in Figure 4-2.

84
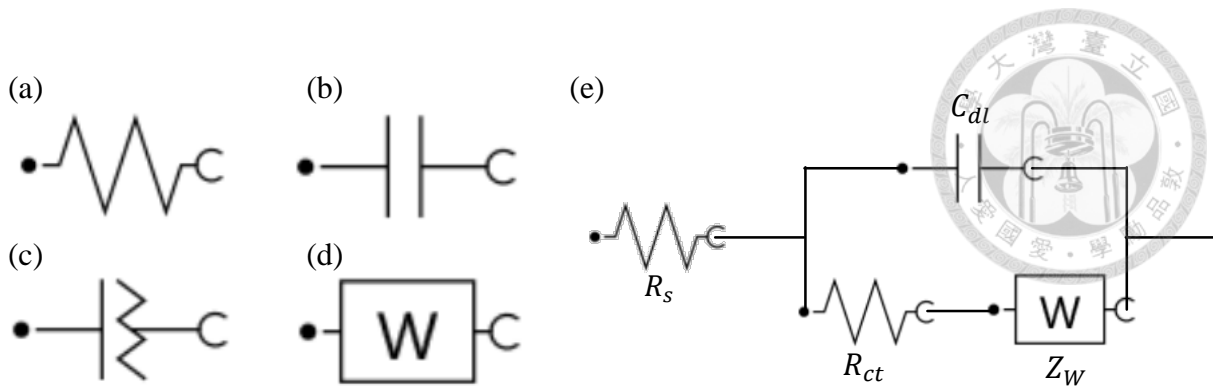
Figure 4-2 A typical Randles circuit and its components. (a) Resistor, (b) capacitor, (c) constant phase element, (d) Warburg element and (e) the Randles circuit.

R_s is determined by solution resistivity that may depend on the ionic concentration, electrode geometry, temperature and the mobility of the ion. C_{dl} is caused by the electrical double layer effect existing on an electrode surface which can lead to non-faradic currents when applying a sinusoidal voltage wave. R_{ct} is a parameter for quantifying the speed of redox reactions which result in faradic currents at the electrode surface and Z_W is a component for modeling the diffusion effect of ions near an electrode. The constant phase element (CPE, using the symbol Q_{dl}) is can be used in place of C_{dl} in order to better present the imperfect behavior of the double layer in this work (Kochowski and Nitsch, 2002). The impedance values of the commonly used components for EIS models are listed in Table 4-1.

Table 4-1 Commonly used equivalent circuit elements.

Name	Symbol	Impedance	Parameters
solution resistance	Z_{R_s}	R_s	R_s
charge transfer resistance	$Z_{R_{ct}}$	R_{ct}	R_{ct}
double layer capacitance	$Z_{C_{dl}}$	$\dfrac{1}{j\omega C_{dl}}$	ω, C_{dl}
constant phase element (double layer capacitance)	$Z_{Q_{dl}}$	$\dfrac{1}{Q_0(j\omega)^n}$	Q_0, ω, n
Warburg element (semi-infinite diffusion impedance)	Z_W	$\dfrac{1}{Y_0\sqrt{j\omega}}$	Y_0, ω

The impedance (Z_{total}) for a single Randles circuit should be calculated as:

$$Z_{total} = \frac{1}{\dfrac{1}{Z_{R_{ct}} + Z_W} + \dfrac{1}{Z_{CPE}}} + Z_{R_s} \tag{38}$$

taking in impedance values,

$$Z_{total} = \frac{1}{\dfrac{1}{R_{ct} + \dfrac{1}{Y_0\sqrt{j\omega}}} + Q_0(j\omega)^n} + Z_{R_s} \tag{39}$$

by applying Euler's formula on the left side,

$$Z_{total} = \frac{1}{\dfrac{1}{R_{ct} + \dfrac{1}{Y_0\omega^{\frac{1}{2}}}\left(cos\dfrac{\pi}{4} - j\,sin\dfrac{\pi}{4}\right)} + Q_0(j\omega)^n} + Z_{R_s}$$

86

$$= \cfrac{1}{\cfrac{1}{(R_{ct} + \cfrac{1}{Y_0 \omega^{\frac{1}{2}}} \cos \cfrac{\pi}{4}) + j(\cfrac{-1}{Y_0 \omega^{\frac{1}{2}}} \sin \cfrac{\pi}{4})} + Q_0(j\omega)^n} + Z_{R_s}$$

$$= \cfrac{1}{\cfrac{1}{A + jB} + Q_0(j\omega)^n} = \cfrac{1}{\cfrac{A - jB}{A^2 + B^2} + Q_0(j\omega)^n} + Z_{R_s} \qquad (40)$$

where

$$A = R_{ct} + \cfrac{1}{Y_0 \omega^{\frac{1}{2}}} \cos \cfrac{\pi}{4} \qquad (41)$$

and

$$B = \cfrac{-1}{Y_0 \omega^{\frac{1}{2}}} \sin \cfrac{\pi}{4} \qquad (42)$$

By applying Euler's formula ($e^{jx} = cosx + jsinx$) on the right side,

$$Z_{total} = \cfrac{1}{\cfrac{A - jB}{A^2 + B^2} + Q_0\omega^n(\cos \cfrac{n\pi}{2} + j \sin \cfrac{n\pi}{2})} + Z_{R_s}$$

$$= \cfrac{1}{\cfrac{A - jB}{A^2 + B^2} + Q_0\omega^n \cos \cfrac{n\pi}{2} + jQ_0\omega^n \sin \cfrac{n\pi}{2}} + Z_{R_s}$$

$$= \cfrac{1}{(\cfrac{A}{A^2 + B^2} + Q_0\omega^n \cos \cfrac{n\pi}{2}) + j(\cfrac{-B}{A^2 + B^2} + Q_0\omega^n \sin \cfrac{n\pi}{2})} + Z_{R_s}$$

$$= \cfrac{1}{C + jD} + Z_{R_s} = \cfrac{C - jD}{C^2 + D^2} + Z_{R_s} \qquad (43)$$

where

$$C = \cfrac{A}{A^2 + B^2} + Q_0\omega^n \cos \cfrac{n\pi}{2} \qquad (44)$$

and

$$D = \cfrac{-B}{A^2 + B^2} + Q_0\omega^n \sin \cfrac{n\pi}{2} \qquad (45)$$

87

4.2.2 Calculations for a Symmetric Randles Circuit

The component values for a symmetric Randles circuit can be found by fitting the

EIS data with a single Randles circuit as proved below. A symmetric two electrode system

can be thought of as two Randles circuits in series with each other as in Figure 4-3. For

symmetric electrodes, it is sometimes probable to induce different reactions on the two

electrodes. However, the same conditions are usually applied on both electrodes in which

identical values of R_s, R_{ct}, Q_{dl} and Z_W can be assigned on the two sides.
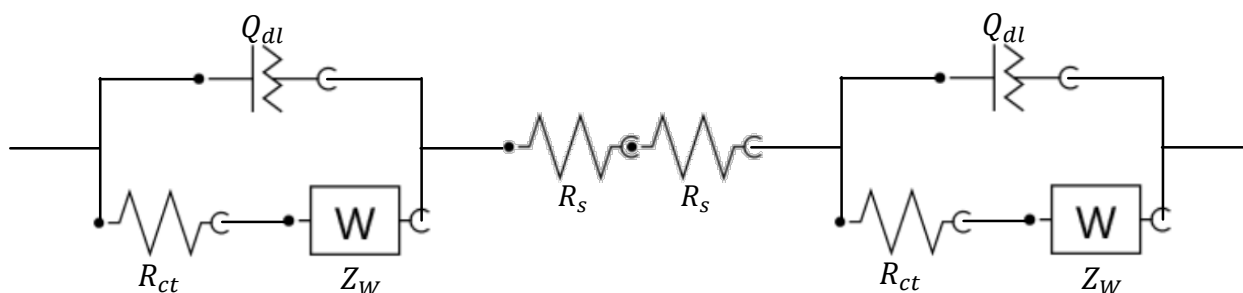
Figure 4-3 Equivalent circuit model for a symmetric electrode system.

For a symmetric Randles circuit Figure 4-3, the impedance should be:

$$2\frac{C-jD}{C^2+D^2}+2Z_{R_s} = \frac{\frac{C}{2}-j\frac{D}{2}}{\left(\frac{C}{2}\right)^2+\left(\frac{D}{2}\right)^2}+2Z_{R_s} \tag{46}$$

Thus, if one is to fit a symmetric electrode system using a single Randles circuit, the

solution resistance is doubled and C and D are halved from the real value. Eqn. (44) and

(45) can be further extended as:

88

$$\frac{C}{2} = \frac{2A}{(2A)^2 + (2B)^2} + \frac{Q_0}{2} \omega^n \cos \frac{n\pi}{2} \qquad (47)$$

and

$$\frac{D}{2} = \frac{-2B}{(2A)^2 + (2B)^2} + \frac{Q_0}{2} \omega^n \sin \frac{n\pi}{2} \qquad (48)$$

which means A and B are doubled, Q_0 is halved and n is the same compared with the real

value. Furthermore,

$$2A = 2R_{ct} + \frac{1}{\frac{Y_0}{2} \omega^{\frac{1}{2}}} \cos \frac{\pi}{4} \qquad (49)$$

and

$$2B = \frac{-1}{\frac{Y_0}{2} \omega^{\frac{1}{2}}} \sin \frac{\pi}{4} \qquad (50)$$

R_{ct} is doubled and Y_0 is halved from the real value. Therefore, the fitting complexity for a

symmetric electrode system can be significantly reduced by just using a single Randles

circuit model. An overall comparison of the component parameters is detailed in Table

4-2. The experimental proof of principle is designed and conducted, and is detailed in

section 4.3.4 and 4.4.1.

Table 4-2 Parameter comparison of symmetric electrode systems using single Randles circuit fitting

component parameter	R_s	R_{ct}	Q_0	n	Y_0
comparison with real value	doubled	doubled	halved	same	halved

4.3 Materials and Methods

4.3.1 Reagents and Materials

Table 4-3 List of reagents and materials used in Chapter 4

Material	Firm	Specification
standard Au electrode	CH instruments	CHI101 2mm Φ
microscopic slide	Jen An Technology	plain 1" x 3"
Au evaporation slug	GUV Team Int Co., Ltd.	99% 2mmΦ x 3.3mmL
Cr evaporation shot	GUV Team Int Co., Ltd.	99.99% 1-3mm and 3-5mm
Ti evaporation slug	GUV Team Int Co., Ltd.	99.995% 6mm Φ
emulsion film	Taiwan Kong King	10000dpi – CD:21±3um
potassium ferricyanade	J.T.Baker	$K_3Fe(CN)_6$
potassium ferrocyanide	Acros Organics	$K_4Fe(CN)_6$
positive photoresist	MicroChem	S1813
negative photoresist	MicroChem	SU8-2050
PDMS (polydimethylsiloxane)	BingBond	Qsil 216
BSA	Sigma-Aldrich	A2153-50g
MUC1	Abnova	H00004582-Q01
MUC1-peptide	Geonomics	95%
MUC1 aptamer (S2.2)	Fu-Xing Medical Equipment CO., LTD	S2.2-SH
thrombin	Haematologic Technologies	FF0315-1mg
thrombin aptamer	Fu-Xing Medical Equipment CO., LTD	HTDQ29-SH
random 25mer oligonucleotide	Fu-Xing Medical Equipment CO., LTD	Rnd-SH

4.3.2 Instruments and Equipment

Table 4-4 List of instruments and equipment used in Chapter 4

Instrument or Equipment	Firm	Model
electrochemical analyzer	CH Instruments, Inc.	CHI614b
syringe pump	KD Scientific Inc	Legato 111
electronic microbalance	Mettler-Toledo	AB104
pH meter	Mettler-Toledo	S220
vortex mixer	Scientific Industries	Vortex Genie 2
ultrasonic cleaner	Branson	3210R-MT
microplate spectrophotometer	BioTek Instruments	Epoch
PCR machine (thermo cycler)	Applied Biosystems	2720 Thermal Cycler
3D printer	Synmao Technology	D-Force 300
E-beam	Prohanns Technology	FULINTEC E-Gun
syringe	Hamilton	1002LTN 2.5mL
crucible	GUV Team Int Co., Ltd.	W liner 3c.c.
adjustable volume pipettes	RAININ	LTS series
fume hood	HIGH TEN	4BH-24
dermal punch	Miltex	1mm diameter

4.3.3 Fabrication of Symmetric Au Electrode Chips

Figure 4-4 illustrates the process for fabrication of the symmetric Au electrode chip used for proof of theory (section 4.4.1). (The same configuration of chip is also applied for real-time impedimetric aptasensing of MUC1 in supplementary material). The following paragraphs explain the process in detail.

Spin coating of positive PR S1813

UV exposure and develop

E-beam evaporation Au/Cr (80/20 nm)

Acetone lift-off
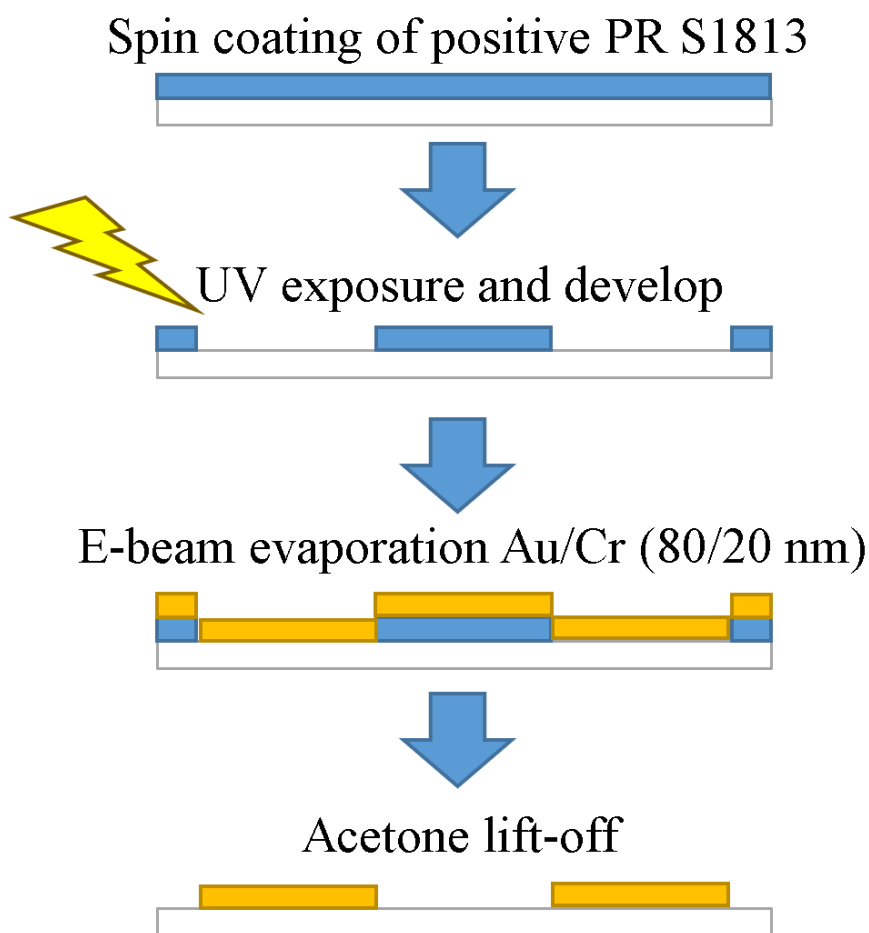
Figure 4-4 Fabrication process of symmetric Au electrode chips.

92
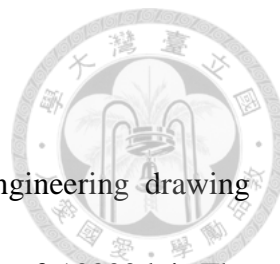
4.3.3.1 Electrode Design

Electrodes with different patterns are designed using an engineering drawing software (SolidWorks) then sent for printing on an emulsion film of 10000dpi. The drawings are fit for contact aligning on three 1"×3" microscopic glass slides with longer edges touching each other. Black areas with no transmittance are areas that would be lift-off by acetone and the transparent areas are of the electrodes.

4.3.3.2 S1813 Photolithography

Microscopic glass slides of dimensions of 1"×3" are washed respectively with 10min acetone, isopropanol (IPA) and distilled water in an ultrasonic cleaner and are subsequently blown with air and dried on a 120°C hot plate. S1813 is taken out from the refrigerator (4°C) then carefully dropped onto the cooled slides till full surface coverage. Slides are spin coated for 1000rpm (20s), 4000rpm (60s) and soft baked at 115°C for 1min then cooled at room temperature (RT) one at a time. After cooling of the slides, groups of three slides with longer edges touching are fit onto the mask aligner. The emulsion film with electrode design is taped to a glass mask and covered on top, softly touching the slides and are exposed for 10s (6mW). The exposed slides are then immersed in TMAH for 1min for developing, rinsed by distilled water and blown dry immediately. The slides are thus covered with S1813 with has the complementary shape of the electrodes prepared for Au deposition.

93

4.3.3.3 E-beam Au Evaporation
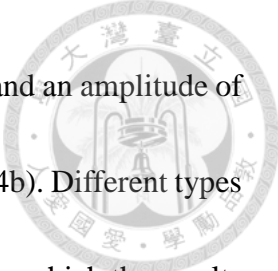
The photolithography processed slides are stuck onto 4" wafers using insulation tape with enough spacing and clipped onto the plate in the E-beam chamber. Crucibles are put in place with several slugs of the same target metal (Ti and Au) inside them. The chamber is then shut close and sucked vacuum for 1.5hr. An adhesive layer of 20nm Ti and the main electrode material 80nm Au are sequentially evaporated onto the slides with a gentle rotation of the plate which holds the slides which are inside the evaporator for uniform deposition. This main evaporation process takes approximately 30min before breaking the vacuum and taking out the slides and crucible. The slides are soaked in acetone overnight to lift off the photoresist. If the S1813 cannot be fully lift off, ultrasonication can be applied but would sometimes damage the slides. At last, the slides are averagely cut in three to make a complete electrode chip.

94

4.3.4 Experimental Proof of Theory

In section 4.2, a novel method for interpreting the equivalent circuit for a symmetric electrode is proposed and calculated in theory. Although the results may seem fair enough, there might appear to be some underlying phenomenon in such a system which the model cannot explain. In the following paragraph, the experimental design for the proof of principle for validating the equivalent circuit theory is detailed using the fabricated symmetric electrode chips.

In order to validate the correctness of the theory, a symmetric electrode system and a three electrode system must be designed, fabricated, implemented and compared with as most control variables as possible. For achieving such accomplishments, fixed volume, electrode spacing and electrode area are required. Thus, a micro-well is designed (Dimension: 3.6(L) x 3.6(W) x 5(H)mm, volume per measurement = 40μL.), fabricated using PDMS soft lithography which the aluminum mold is cut by a CNC machine, and used for limiting the exposed electrode area and volume and is clipped to the fabricated electrode chip by a 3D-printed fixture. A symmetric electrode system is implemented by connecting the WE wire to one end of the chip and the CE/RE wire to the other. On the other hand, a three electrode system is implemented by also connecting the WE to one end of the chip but only the RE wire is connected to the other end. The CE wire is connected to a Pt wire electrode separately and dipped into the micro-well forming a three

95

electrode setup. EIS data is measured at $0.1\sim10^5$Hz with a bias of 0V and an amplitude of 5mV using an electrochemical analyzer (CH Instruments, Inc., CHI614b). Different types of electrodes are compared in order to generalize the proof of principle which the results are further discussed in section 4.4.1.

The overall goal is simple: to confirm validity of Table 4-2. The EIS data obtained from the experiments are fit using the single Randles circuit fitting program which the fitting algorithm applied are detailed. After parameter fitting, values for R_{ct}, R_s, Y_0, Q_0 and n are compared between symmetric electrode and three electrode systems and checked if the relationship founded using equivalent circuit theory is really exhibited.

96
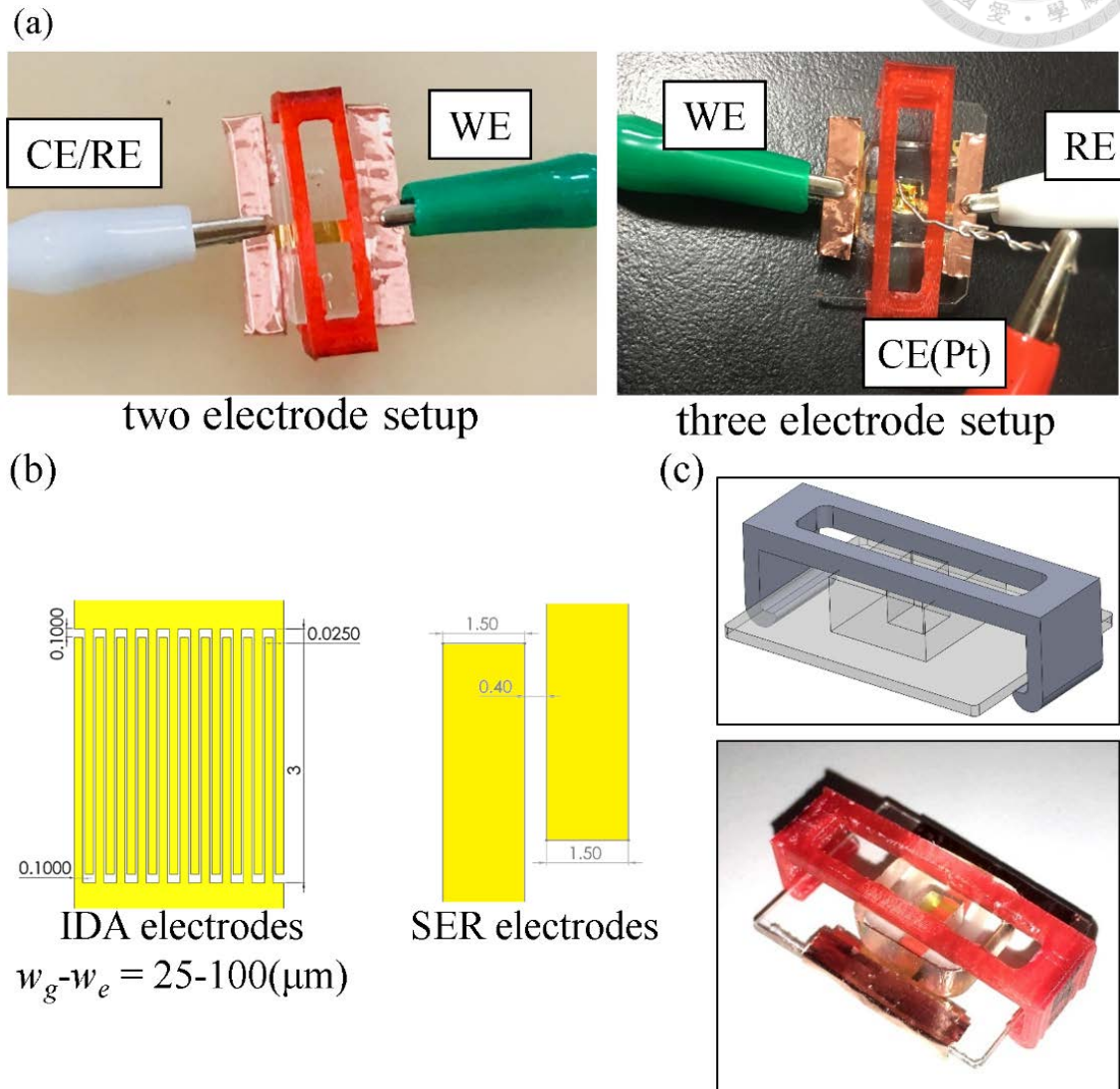
Figure 4-5 Setup for proof of symmetric equivalent circuit. (a) Two and three electrode setups. (b) Dimensions for two different electrode geometries. (c) Illustration and photograph of electrode chips clipped with microwells. (not indicated units: mm)
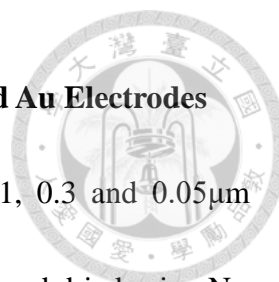
4.3.5 Fabrication of Impedimetric Aptasensor using Two Standard Au Electrodes

Two standard Au electrodes are polished thoroughly using 1, 0.3 and 0.05μm aluminum oxide slurry. It is then dipped in piranha solution for 5min and dried using N_2. One electrode is arbitrarily selected as the WE and the other as the CE/RE. The two electrode are simultaneously dipped in a solution of 5μM sensing element (HTDQ29-SH, S2.2-SH or random 25mer ssDNA-SH) in immobilization buffer (50mM Tris, 100mM NaCl, 4mM KCl, 2.5mM $MgCl_2$, 1mM $CaCl_2$, pH 7.5) overnight at RT. After immobilization, the electrodes are washed two times by dipping into washing buffer (Washing buffer: 0.05% Tween20 in binding buffer. Binding buffer: 10mM Tris-HCl, 50mM KCl, pH 7.5.) for 3min and rinsing with DIW. This process washes away non-specific binding of unwanted molecules. The aptasensor is then fabricated and can perform detection of different concentrations of protein. EIS measurements are performed during each stage of fabrication.
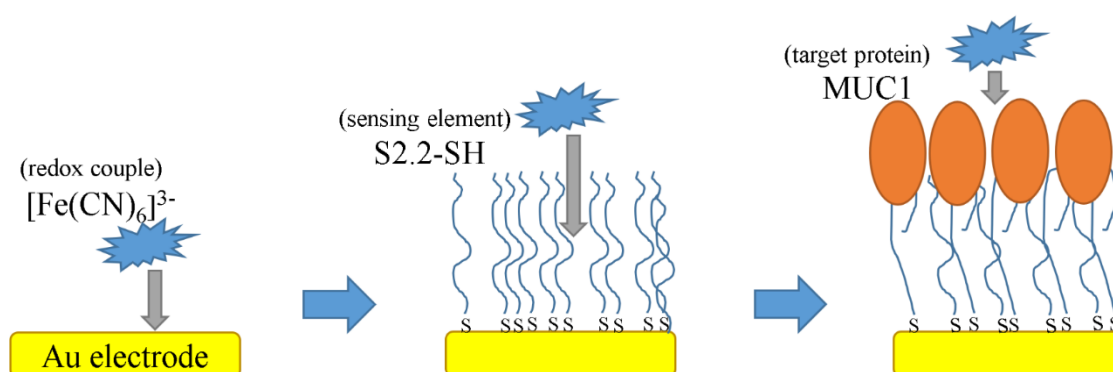
Figure 4-6 Fabrication of impedimetric aptasensor using two standard Au electrodes.

4.3.6 Fabrication of Regenerable Impedimetric Aptasensor using IDA Chips

The IDA chips are designed, fabricated and prepared using the same method as in section 3.3.2. After preparation of the a microwell clipped IDA chip, 1μM HTQD29-SH + MCH is diluted in immobilization buffer (1mM $MgCl_2$ and 1mM EDTA in 1M phosphate buffer, pH 7.5) with a total volume of 80μL, added into the microwell and the chip is held upside-down overnight at RT. The chip is washed twice by adding binding buffer (50mM Tris-HCl, 100mM NaCl, and 1mM $MgCl_2$ in ddH_2O, pH 7.5), standing upright and waiting for 2min at RT (Note that the immobilization buffer and binding buffer for using IDA chips and SGEs are different). Then 1mM MCH in binding buffer is added, and the chip is held upside-down for 2hr at RT to thoroughly block the electrode surface and prevent from non-specific binding. After washing the chip twice, the aptasensor is done fabricated and can be used for thrombin detection. The regenerability and specificity of this aptasensor is verified. EIS is performed after each step during fabrication.

4.4 Results and Discussion

4.4.1 Proof of Theory

This section discusses the results for proving the theory in section 4.2 with experimental procedures detailed in section 4.3.4. In a nutshell, the result for equivalent circuit fitting using a single Randles circuit comparing symmetric and three electrode setups should have a relationship shown in Table 4-2. Two different electrode geometries are used for the proof of theory (Figure 4-5b). Figure 4-7 shows the Nyquist and Bode plots of EIS data obtained on two and three electrode setups using SER electrode chips. The data named "FLIP …" is obtained by either exchanging the WE and CE/RE in two electrode setups or exchanging the WE and RE in three electrode setups. FLIP groups are done in order to guarantee the symmetric characteristics. The phases are identical for two and three electrode setups. However, in the Nyquist and |Z| vs frequency plot, the |Z| of two electrode setups are approximately two times the |Z| of three electrode setups. This correlation is identical to the results obtained from IDA electrode chips (Figure 4-8). The data is fitted with a self-made program for fitting of different equivalent circuits.

100
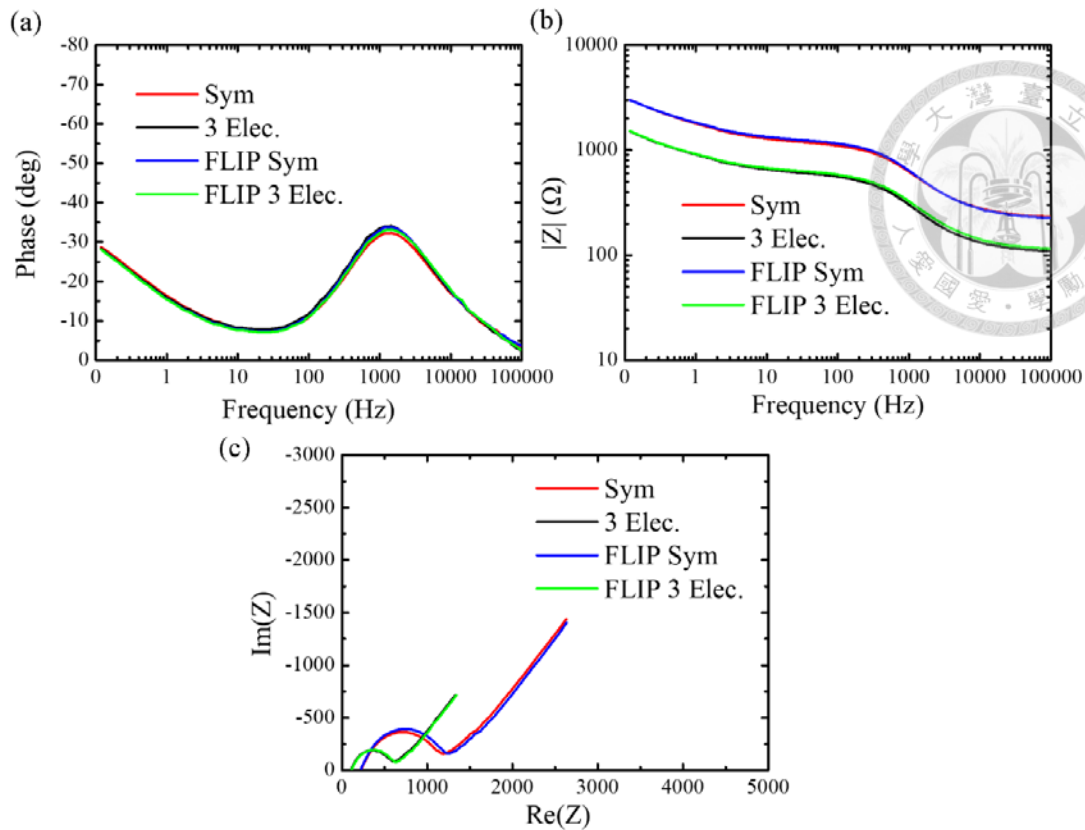
Figure 4-7 Comparison of two and three electrode setups using SER electrode chip. (a) Bode plot (ϕ) (b) Bode plot ($|Z|$) (c) Nyquist plot.
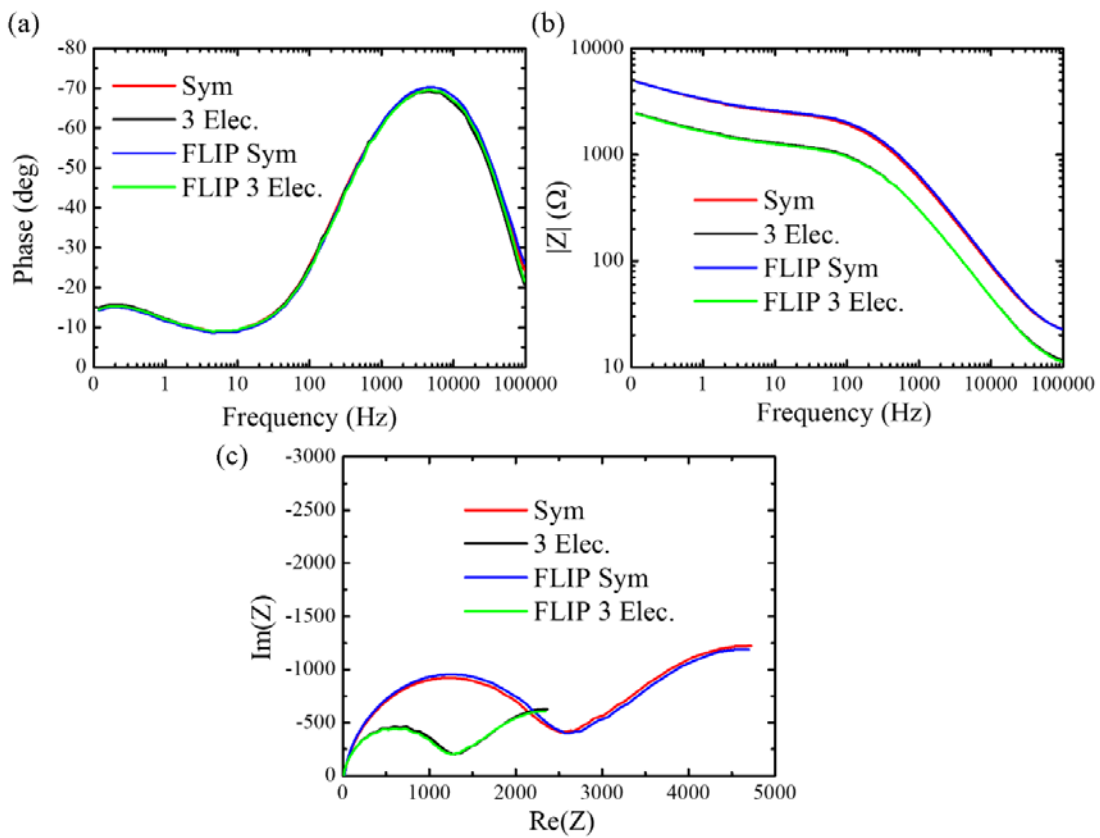
Figure 4-8 Comparison of two and three electrode setups using IDA electrode chip. (a) Bode plot (ϕ) (b) Bode plot ($|Z|$) (c) Nyquist plot.

101
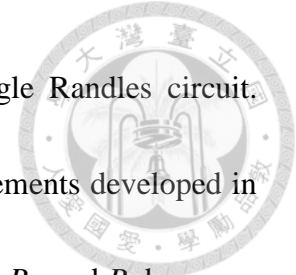
Table 4-5 lists the fitting results obtained by using a single Randles circuit. Warburg elements are used on SER chips and the IDA diffusion elements developed in Chapter 3 are using on IDA chips. The results correspond to theory: R_{ct} and R_s becomes doubled, Q_0 and Y_0 is halved, and n stays the same. Symmetric characteristics are confirmed. This is due the similar values from FLIP and not FLIP groups (e.g. The Q_{dl} of SER 3 elec. and SER FLIP 3 elec. are identical). Note that the theoretical w^2/D and w_e/w for IDA chips are 26.04 and 0.8. The error may be cause by the reason that the lowest frequency is 0.1Hz, which cannot fully present the finite diffusion phenomenon of IDA electrodes and only a small bending of impedance is seen in its Nyquist plot.

Table 4-5 Fitting results using a single Randles circuit as the equivalent circuit.

	R_{ct} (Ω)	R_s (Ω)	Q_0 (for Q_{dl})	n	Y_0 (diffusion)	w^2/D (s)	w_e/w
SER 3 elec.	477.04	109.89	9.84E-06	0.846	0.00287	N/A	N/A
SER 2 elec.	929.06	232.14	5.97E-06	0.810	0.00144	N/A	N/A
SER FLIP 3 elec.	487.30	115.07	9.84E-06	0.832	0.00294	N/A	N/A
SER FLIP 2 elec.	986.40	226.50	5.67E-06	0.814	0.00147	N/A	N/A
IDA 3 elec.	1183.7	8.244	1.84E-06	0.848	0.00131	22.51	0.678
IDA 2 elec.	2342.0	15.410	8.95E-07	0.852	0.00065	21.19	0.652
IDA FLIP 3 elec.	1152.7	7.560	1.85E-06	0.847	0.00127	20.79	0.595
IDA FLIP 2 elec.	2399.7	14.694	7.88E-07	0.859	0.00066	21.25	0.634
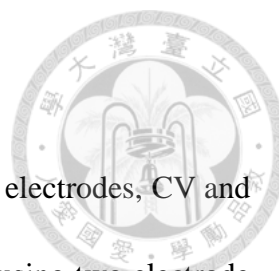
4.4.2 Optimizing the Operating Sensing Voltage (E_{init})

For optimizing the operating sensing voltage of symmetric Au electrodes, CV and

EIS experiments are performed on two standard bare Au electrodes using two electrode

setup (WE: Au, CE/RE: Au) (Figure 4-9). For this system, 10mM $Fe(CN)_6^{3-}$ is used as the

redox species. Two pairs of peaks appeared in the cyclic voltammogram. This result is

due to the asymmetric characteristic in solution, that on the $Fe(CN)_6^{3-}$ is added. However,

one can still find an optimized sensing voltage for EIS detection. By relating the R_{ct} and

the current density, the optimal operating sensing potential (E_{init}) of 0.7V for the

symmetric system is found.
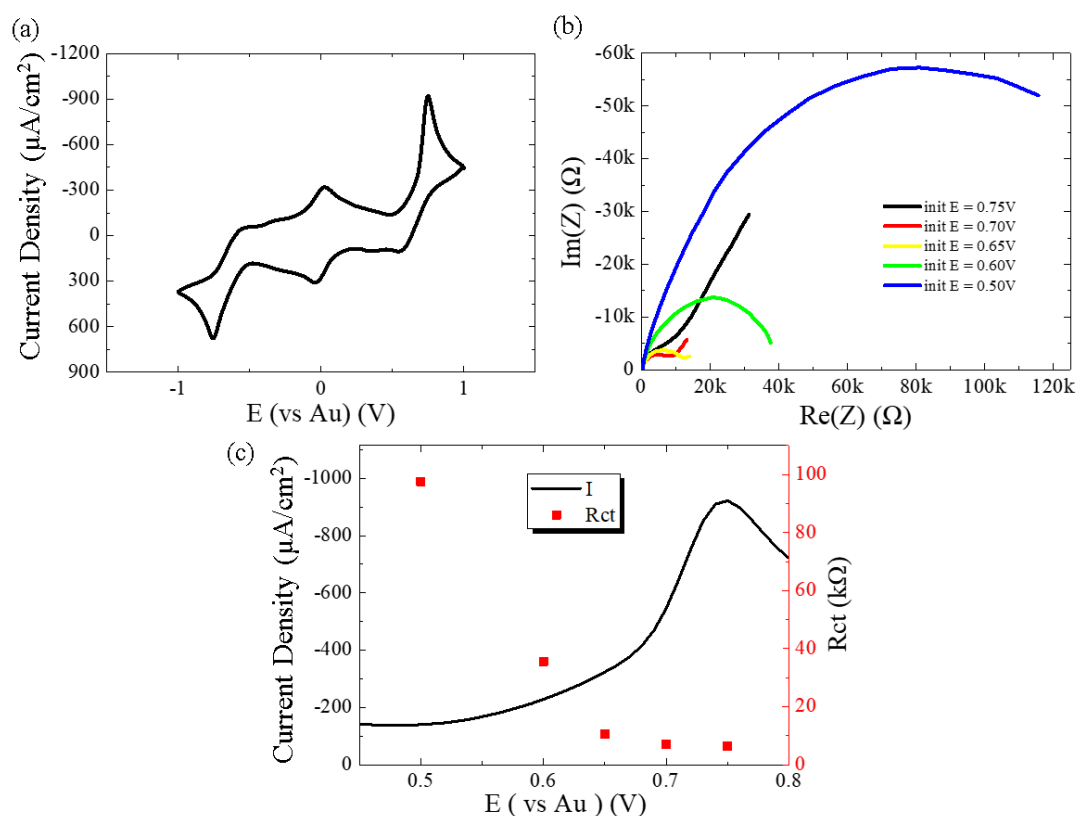
Figure 4-9 Optimizing the EIS initial voltage (E_{init}). (a) Cyclic voltammogram using symmetric Au electrodes. (b) Nyquist plot of symmetric bare Au electrodes at different E_{init}. (c) Sectional view of (a) and its corresponding R_{ct} with E = E_{init}. The solution contains 10mM $Fe(CN)_6^{3-}$ and 0.1M KCl.

103

4.4.3 Proof of Concept by Thrombin Aptasensing

Using the above mentioned initial potential for EIS measurements, proof of concept

by thrombin aptasensing is successfully done using the symmetric electrode system. The

binding buffer used is 10mM Tris-HCl, 50mM KCl (pH 7.5). After each binding step with

a certain concentration, washing of electrodes are performed three times using washing

buffer (0.05% Tween20 in binding buffer) and then immediately used in EIS detection

(10mM $Fe(CN)_6^{3-}$ in binding buffer). Figure 4-10 plots the Nyquist plot and fitted values

of ΔR_{ct} vs thrombin concentration. Here ΔR_{ct} = any R_{ct} value subtracted by the R_{ct} after

aptamer immobilization. A one-site specific binding model is used for parameterizing the

binding mechanism (Masel, 1996). The relation between concentration and R_{ct} is

accordingly:

$$\Delta R_{ct} = \frac{B_{max}[Target]}{K_D + [Target]} \tag{51}$$

Here, B_{max} ([=] Ω) represents the maximum ΔR_{ct} when all the sites are occupied. B_{max} =

1829.1Ω and K_D = 129.4nM. The results show that the setup of using symmetric Au

electrodes with an operating sensing voltage of 0.7V can be used for impedimetric

aptasensing of targets. So the proof of concept is completed and MUC1 will be used for

the following sections.
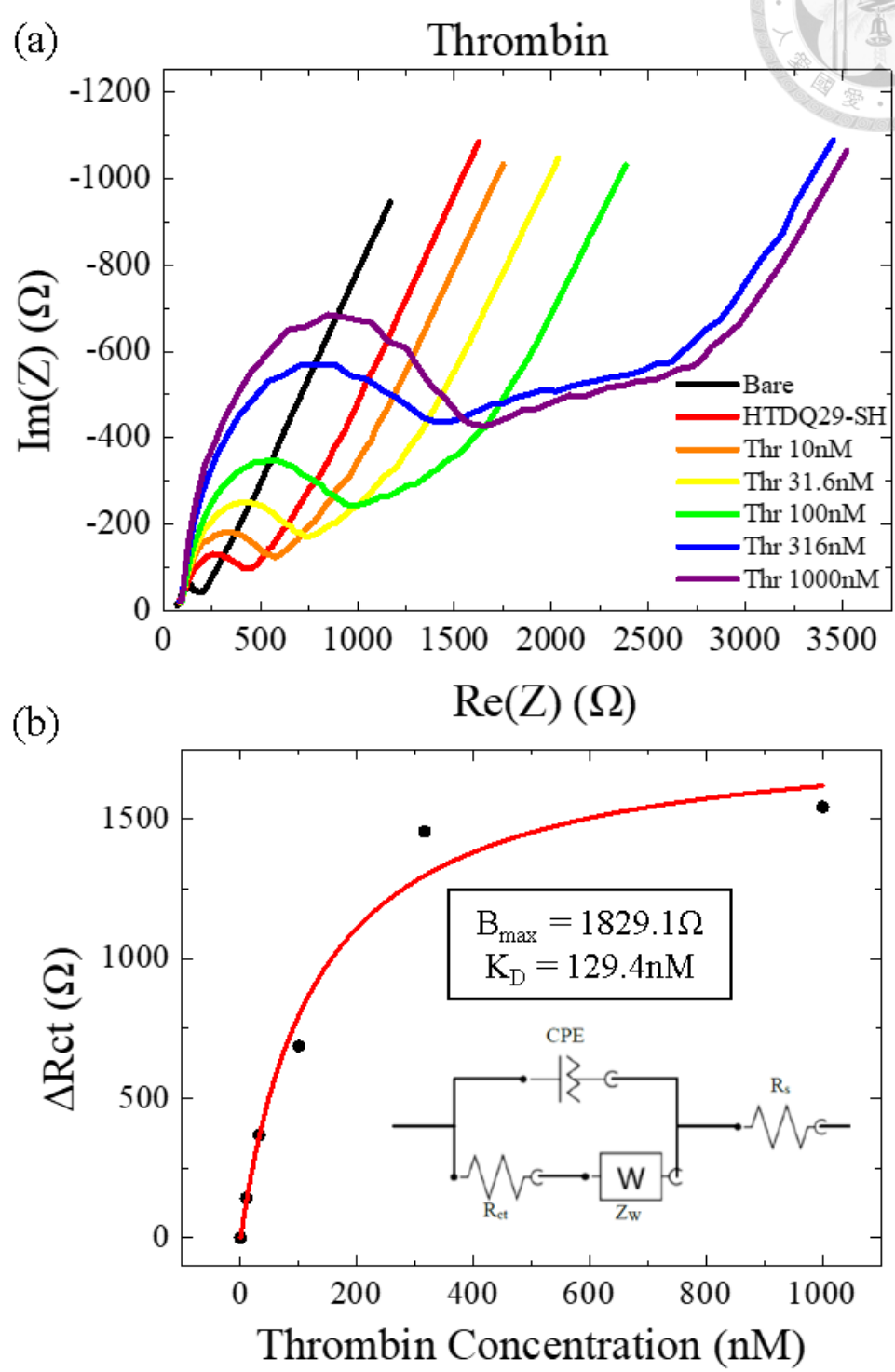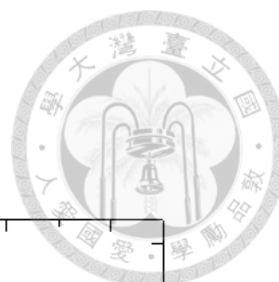
Figure 4-10 (a) Nyquist plot of symmetric Au electrode aptasensor bound with different concentrations of thrombin. (b) ΔR_{ct} vs thrombin concentration and fitted curve using one-site specific binding model.

4.4.4 MUC1 Aptasensor using a Three Electrode Configuration

MUC1 detection using a three electrode setup is performed. The fabrication, target binding process and data fitting method are the same as for thrombin detection. However, for confirmation of aptamer specificity, BSA is used as the counter target. Figure 4-11 shows the Nyquist plots using MUC1 and BSA as the target and their R_{ct} fitting values. A significantly smaller change in R_{ct} is found. This indicates that specific interaction between and MUC1 and the S2.2 aptamer is present. For MUC1, $B_{max} = 7906.5\Omega$ and $K_D = 15.11nM$. These two parameters are compared with two electrode setups.
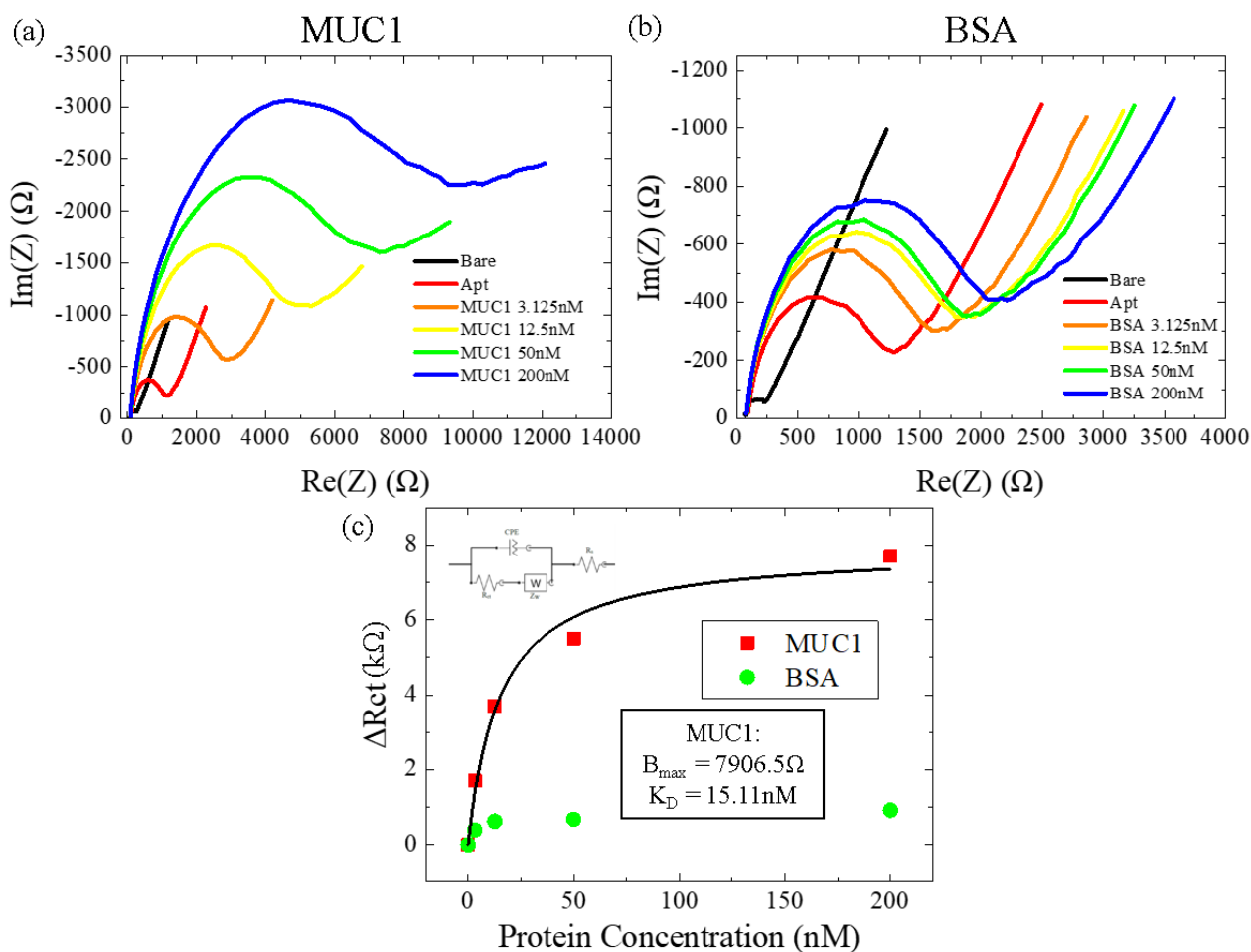
Figure 4-11 Nyquist plot of three electrode setup aptasensor bound with different concentrations of (a) MUC1 and (b) BSA. (c) ΔR_{ct} vs target concentration and fitted curve using one-site specific binding model.

4.4.5 MUC1 Aptasensor using Two Symmetric Au Electrodes

After confirmation of specific binding between MUC1 and S2.2, the two electrode

setup is finally implemented for MUC1 detection. Figure 4-12 shows the Nyquist plots

using MUC1 and BSA as the target and their R_{ct} fitting values using two electrode setups.

For MUC1, $B_{max} = 17084\Omega$ and $K_D = 15.92nM$.
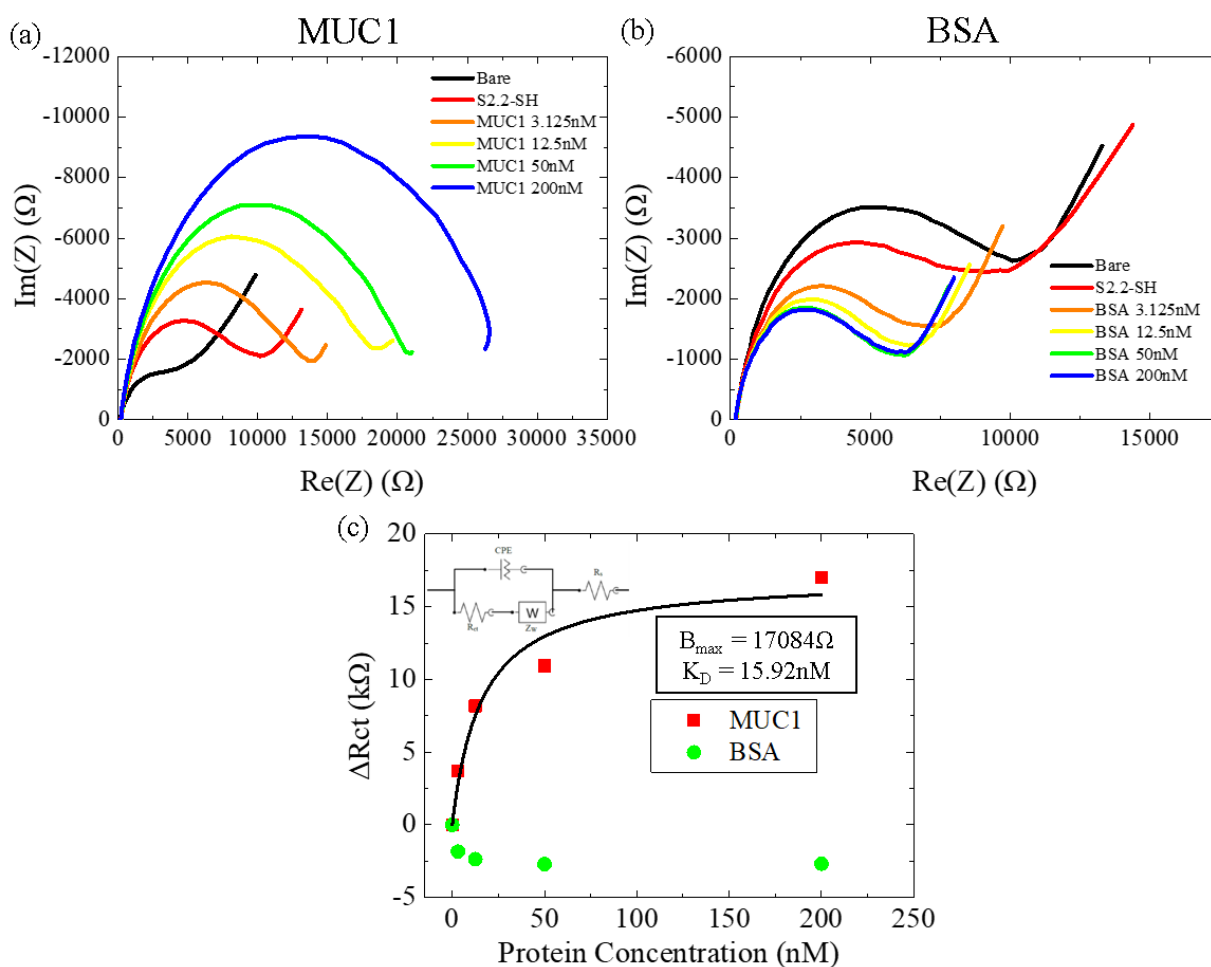
Figure 4-12 Nyquist plot of two symmetric electrode setup aptasensor bound with different concentrations of (a) MUC1 and (b) BSA. (c) ΔR_{ct} vs target concentration and fitted curve using one-site specific binding model.

Table 4-6 compares the conditions and parameters between thrombin detection

(two electrode setup), the three and the two electrode setup for MUC1 detection.
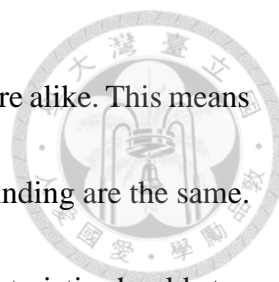
Reasonably, the K_D obtained from the two and three electrode setups are alike. This means

for either setup, the MUC1 concentration that leads to half-full site binding are the same.

Indeed, as long as the aptamer probe density are the same, this characteristic should stay

the same regardless of the electrochemical setup. The B_{max} obtained has a ratio of two

between the two setups. This also agrees to the theory, that in symmetric setups, ΔR_{ct} is

doubled when fitted using a single Randles circuit. However, the correlation between the

concentration of BSA and ΔR_{ct} are opposite comparing the two setups. This phenomenon

still cannot be explained by this study and can serve to be a potential interest in future

work.

Table 4-6 Comparison of aptasensors using three and two (symmetric) Au electrode setups.

	proof of concept	MUC1 (three electrode)	MUC1 (two electrode)
electrode setup	two symmetric	three	two symmetric
target	thrombin	MUC1	MUC1
counter target	none	BSA	BSA
E_{init}	0.7V (vs Au)	0.244V (vs Ag/AgCl)	0.7V (vs Au)
V_{amp}		5mV	
ΔR_{ct} vs [Target] correlation	+	+ (BSA : +)	+ (BSA : −)
K_D	129.4nM	15.11nM	15.92nM
B_{max}	1829.1Ω	7906.5Ω	17084.4Ω

4.4.6   DNA Sequence Specificity Towards MUC1 and BSA

The previously obtained results might seem reasonable. However, there might be a chance that MUC1 binds to "anything" and is not specific of different ssDNA sequences. Therefore, DNA sequence specificity towards MUC1 is confirmed with BSA being the counter target. Four different experiments are conducted which either the S2.2 aptamer or random 25mer ssDNA is used as the sensing element and either MUC1 or BSA is used as the target protein. The aptasensor fabrication process is identical to the previously discussed two electrode setup.

Figure 4-13 displays their Nyquist plots. The scales are adjusted to be the same. In a glance, it is able to confirm that the S2.2 aptamer can truly bind specifically to MUC1. Figure 4-14 shows their R_{ct} fitted values. For S2.2 being the sensing element and MUC1 being the target, $B_{max} = 15655\Omega$ and $K_D = 17.9nM$. This is similar to the result obtained in section 4.4.5. It can also be seen that MUC1 and BSA have approximately the same tendency to bind to random sequences, which means that comparison of binding ability between them are done on an equal basis. This not only examines the theoretical correctness and also proves possible potential applications.
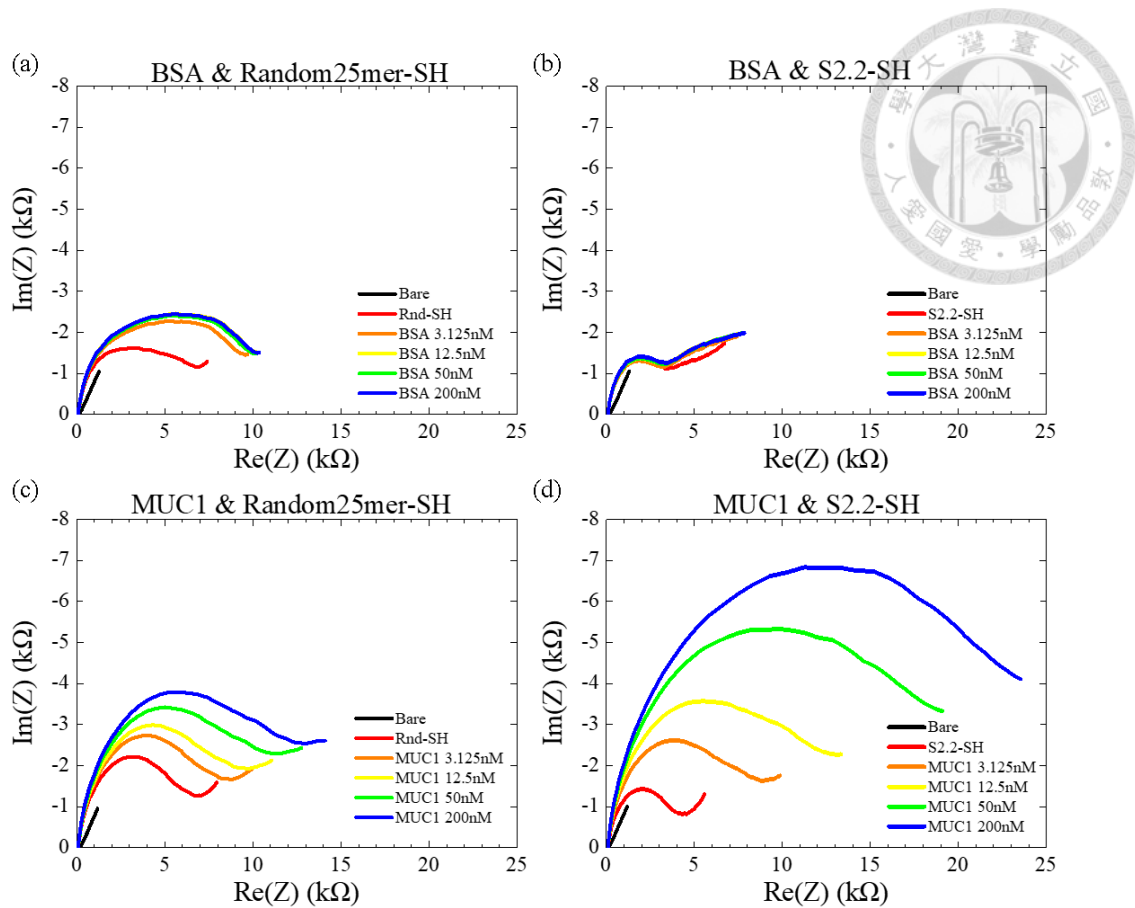
Figure 4-13 Nyquist plot using different detection targets and sensing elements. Target: (a), (b) BSA and (c), (d) MUC1. Sensing element: (a), (c) Random 25mer sequence and (b), (d): S2.2 aptamer.
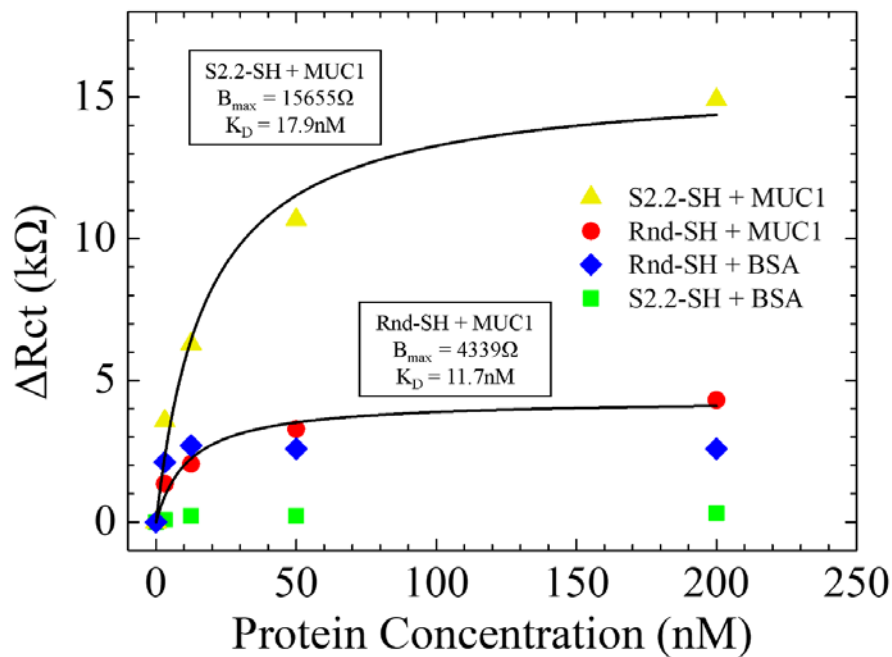
Figure 4-14 ΔR_{ct} vs target concentration and fitted curve using one-site specific binding model for DNA sequence specificity towards MUC1 and BSA.

110

4.4.7 Regenerability and Specificity of Thrombin IDA Aptasensor

In this section, an impedimetric aptasensor for detection of thrombin is fabricated on IDA electrode chips. After fabrication, 20nM thrombin or 15μM HSA is added to compare their specificity against HTDQ29-SH. A regeneration step is applied following each protein binding step to thoroughly break the binding between HTDQ29-SH and the target protein and wash off all non-specific binding conditions. This can restore the functionality of the aptasensor for the next detection step. For every protein binding step, 80μL target protein diluted in binding buffer is added and the chips are held upside down for 10min at RT. For every regeneration step, 100μL regeneration buffer (2M NaCl in ddH$_2$O) is added and the chips are placed upright for 10min at RT. The chips are washed with binding buffer twice and characterized using EIS after each protein binding or regeneration process.

EIS data for the first six steps is shown in Figure 4-15. Qualitatively interpreting, the R_{ct} (the diameter of the imperfect semi-circle) becomes smaller after MCH blocking. Due to the fact that the immobilization buffer has high ionic strength that cancels out the negative charge on the ssDNA, there might be strong non-specific binding of the aptamer on the electrode after HTDQ29-SH immobilization (Studier, 1969). After immersing in a comparatively higher concentration of MCH in binding buffer, the non-specific bound aptamers are somehow plucked off from the electrode surface with MCH occupying their

111

original sites. This will lead to the decrease in R_{ct}. After adding 2M NaCl, the R_{ct} becomes

even smaller. This might be caused by further washing of the electrode, removing non-

specifically bound MCH or even HTDQ29-SH (Goode et al., 2015). Addition of 20nM

thrombin increases the R_{ct}, and then addition of 2M NaCl (second time) decreases the R_{ct}

to a point even lower than the first regeneration step. This might be caused by the fact

that the non-specifically bound molecules aren't thoroughly removed after the first

regeneration step. For clarification and examination of regenerability, repeated steps of

protein binding and regeneration procedures are performed in the following paragraph.

Note the down-bending of impedance at low frequencies. It is clear from Chapter 3 that

this is caused by finite diffusion of redox species between two band electrodes, and there

aren't any previous literatures that propose an adequate model to fit this region that can

yield the geometrical parameters. It can be seen that the shapes of impedances at low

frequencies are not influenced by the immobilized materials on the electrode. This is

because the diffusion path from the ICCB (cf. section 3.2.1) to the electrode surface

(typically a few to tens of μm) is comparatively longer that the tip of the self-assembled

monolayer (SAM) to the electrode surface (typically tens of nm), making its specific

diffusion impedance unchanged.
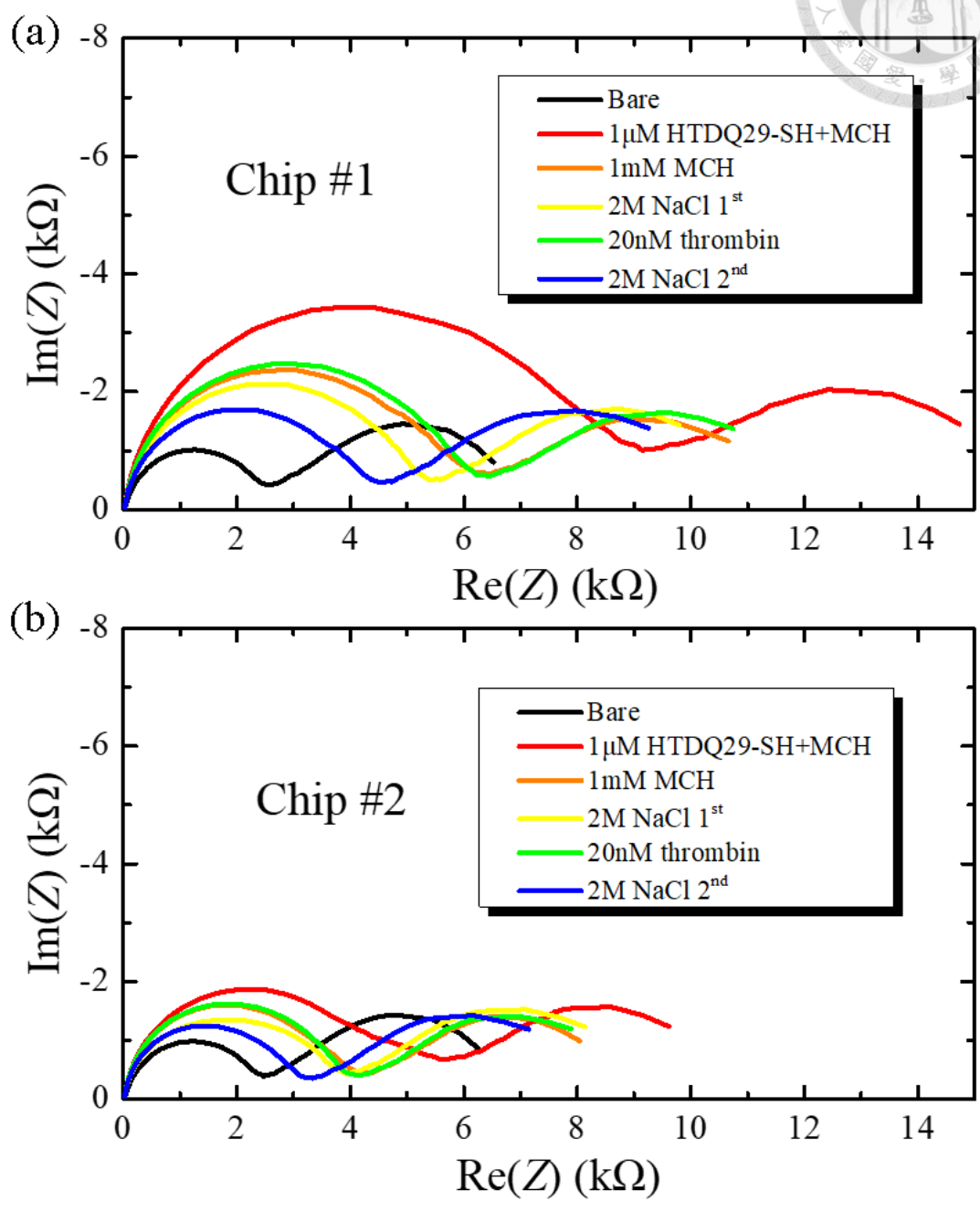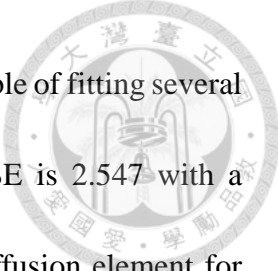
Figure 4-15 Nyquist plot for characterizing the fabrication, detection and regeneration process of thrombin impedimetric aptasensor using IDA chips. (a) Chip #1 and (b) chip #2. The first six steps are shown in the sequence from "Bare" to "2M NaCl 2nd" in the legend.

The circuit fitting program is a self-written program that is capable of fitting several elements including the IDA diffusion impedance. The average MSE is 2.547 with a standard deviation of 1.794 using a Randles circuit with an IDA diffusion element for fitting. This error is small enough and can yield precise fitted parameters (cf. section 3.4.6 for comparison of different diffusion impedance elements used for circuit fitting of IDA electrode EIS data).

A total of four thrombin binding steps and two HSA binding steps are applied on the same electrode consecutively. Figure 4-16a plots the fitted R_{ct} after each step. One can see that after almost each regeneration step, the R_{ct} drops a little compared with its previous regeneration step. Taking the non-specific bound molecules still existing on the electrode in account, the baseline for R_{ct} seems to decay after each step. This baseline is arbitrarily defined as the R_{ct} which is affected by the immobilized SAM layer and the non-specifically bound molecules. If the steps are numbered starting from 1, then on the kth step, the amount of temporarily and non-specifically bound molecules is arbitrarily assumed to decay exponentially. This consequent cause of transient change of R_{ct} is defined as

$$\Delta R_{ct,transient}(k) = B_t e^{-\frac{k}{k_0}} \tag{52}$$

, where B_t ([=] Ω) is the proportional constant that is related to the amount of transient non-specific binding and k_0 (dimensionless) is the constant that can characterize the speed for removal of non-specific binding. B_t might be affected by all the factors that may have

114
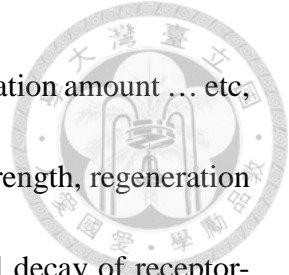
an effect on the R_{ct} (e.g. electrode area), aptamer and MCH immobilization amount … etc,

and k_0 might be affected by the regeneration conditions (e.g. ionic strength, regeneration

time). Note that eqn. (52) is analogous to the first order exponential decay of receptor-

ligand dissociation kinetics (Cima, 1994), where the dissociation rate constant (k_{off}) is

analogous to $1/ k_0$. The difference is k_0 is dimensionless, and is affected by the

regeneration condition, while k_{off} ([=] s^{-1}) characterizes the dissociation rate. Also, the

number of steps k is concerned rather than the time.

The steady-state baseline B_{SS} ([=] Ω) is defined as the R_{ct} only affected by the

immobilized aptamer and MCH without the non-specific bound molecules. Therefore, the

overall baseline can be written as

$$R_{ct,baseline}(k) = B_{SS} + \Delta R_{ct,transient}(k) = B_{SS} + B_t e^{-\frac{k}{k_0}} \qquad (53)$$

Note that eqn. (53) doesn't account for the change of R_{ct} cause by target binding. Thus,

only the regeneration steps can be used to determine the parameters. Accordingly, all the

even number of steps after step 3 are used for non-linear curve fitting of eqn. (53). The

baseline of the two chips are calculated and plotted in Figure 4-16a. The three parameters

can characterize the regenerability of this aptasensor. It can be observed that after each

regeneration step, the R_{ct} drops to approximately the value of baseline, and B_{SS} is almost

reached after the 12th step. This proves that the fabricated IDA impedimetric aptasensor

is able to be regenerated up to six times for six detections.
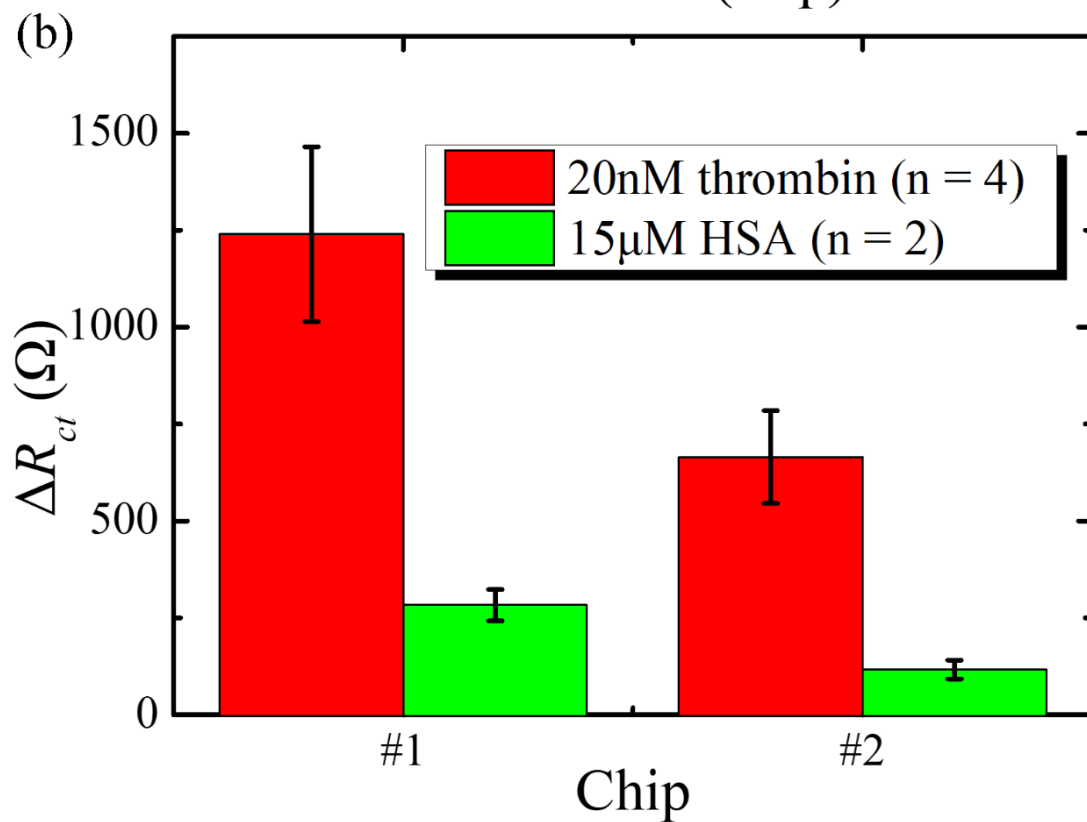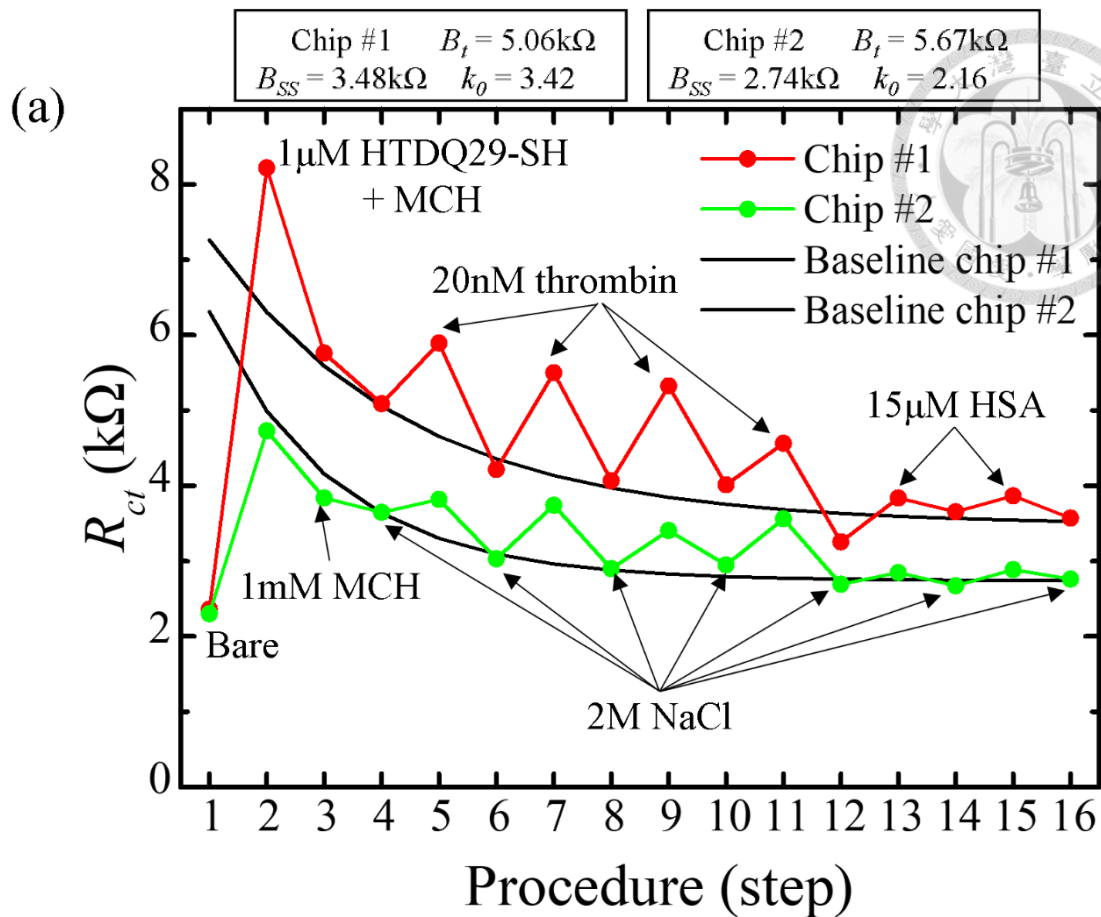
Figure 4-16 (a) R_{ct} vs procedure steps for regenerability test using the IDA chips. (b) ΔR_{ct} ($= R_{ct} - R_{ct,baseline}$) for specificity comparison of thrombin and HSA.

116

The method for determining a baseline for characterizing the regenerability can be further used for obtaining the binding amount of different targets using the same IDA chip. The ΔR_{ct} for each binding event is obtained by

$$\Delta R_{ct}(k) = R_{ct}(k) - R_{ct,baseline}(k) \tag{54}$$

Figure 4-16b plots the calculated values. A 5.1-fold (chip #1) and 5.5-fold (chip #2) difference between the two target proteins is calculated. Even if the concentration of HSA is significantly higher than the concentration of thrombin, a smaller ΔR_{ct} indicates that the binding of HTDQ29-SH and thrombin is quite specific. At last, it is proved that a regenerable impedimetric aptasensor for specific detection of thrombin is successfully fabricated on IDA electrode chips.

4.5 Summary

In summary, specific EIS detection of the thrombin and MUC1 is performed using two symmetric electrode setups. The theory of this study can serve as a method for analyzing symmetric electrode bio-sensing applications. For asymmetric conditions (10mM $Fe(CN)_6^{3-}$), the optimal operating sensing potential for impedimetric aptasensing is identified at 0.7V (vs Au). Specific EIS detection of MUC1 (3 ~ 200 nM) is performed and K_D values of 16.31±1.44nM is obtained. Validity of the two symmetric Au electrode equivalent circuit model is confirmed by comparing R_{ct} values in different electrode setups. Sequence specificity of the binding event is confirmed by comparing S2.2 with 25mer random ssDNA sequences. Fabricated impedimetric aptasensors using IDA chips have the regenerability for six times of detection and the specificity is confirmed (over 5-fold between 20nM thrombin and 15μM HSA).

Though further improvement on sensitivity and selectivity are needed to be realized, the label free and simple characteristics of this system widens its potential for portable, real-time and multiplex developments.

Chapter 5 Conclusion

5.1 Conclusion

In this thesis, electrochemical impedance modeling of symmetric electrodes and IDA chips are proposed for aptasensing applications. Two issues regarding their usage are discussed. (1) Finite diffusion of redox species using IDA electrodes makes data fitting difficult in the low frequency region. (2) For miniaturization, a symmetric electrode setup takes advantage but real parameters cannot be found using a single Randles circuit.

Regarding the first issue (Chapter 3), a novel integral form of solution for calculating the diffusion impedance of IDA electrodes is derived. The theory is based on an imaginary constant concentration boundary (ICCB) assumption, conformal mappings of IDA geometries, finite diffusion length derivation and cylindrical finite diffusion approximation. The dimensionless impedance slightly resembles the finite cylindrical diffusion impedance when $r_\delta/r_0 > 1$. Simulations show the ICCB assumption valid but indicate erroneous predictions when $w_g/w_e < 0.1$. The theory can also be used for calculating the limiting current. The IDA diffusion element proves to exhibit minimal error among three other elements in circuit fitting. Three parameters w_g/w_e, w^2/D and Y_0 can be found by fitting a single EIS data. To the best of the author's knowledge, this is the first approach for derivation of the IDA diffusion impedance regarding relevant

119

parameters such as the electrode bandwidth (w_e) and gap width (w_g).

For the second issue (Chapter 4), the parameter relationship between a single and symmetric Randles circuit is found. R_{ct} and R_s would be double the real value, Q_0 and Y_0 would be half the real value, and n would be the same. Optimal operating sensing potential for symmetric impedimetric aptasensing in contact with $Fe(CN)_6^{3-}$ is identified at 0.7V (vs Au). Specific EIS detection of MUC1 (3 ~ 200 nM) is performed and K_D values of 16.31±1.44nM are obtained. Validity of the symmetric Randles circuit model is confirmed by comparing R_{ct} values in different electrode setups. Sequence specificity of the binding event is confirmed by comparing S2.2 with 25mer random ssDNA sequences. The theory developed from the first and second issue are combined and confirmed that fabricated impedimetric aptasensors using IDA chips have the regenerability for six times of detection and the specificity is over 5-fold between 20nM thrombin and 15μM HSA.

To sum up, the theories derived and experiments conducted in this thesis provide some insights for understanding diffusion behavior and symmetric electrode circuits. Researchers can model their systems more accurately and find important parameters. The author believes that this research can help readers in different fields of microanalysis, biosensors and biochips, in particular for those who are interested in use of symmetric electrodes (including IDA chips) for impedimetric detection.

5.2 Future Work

Point-of-care needs are becoming more demanding with a growing number of innovative technologies and highly competitive markets. Bulky and costly instruments are being replaced by integrated bio-sensing platforms. The author has developed a simple microfluidic system integrated impedimetric aptasensor using IDA electrode chips for real-time detection. The chip has a small volume (25(L)×19(W)×6(H) mm^3), which can be easily packaged and shipped to end-users in need, and has low sample usage. Portable sensing devices are also being developed in corporate with the symmetric electrode chips. Preliminary results are detailed in supplementary material for providing the reader a more concrete concept for future development.
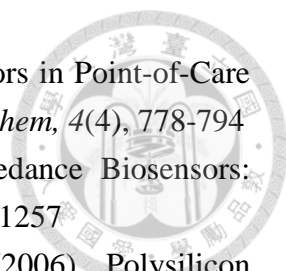
The author anticipates extensive applicative researches in related fields of interest, hoping to furthermore bridge everyday life with the future vision of advanced bio-sensing technologies.

121

References

1. Abramowitz, M. (1974). *Handbook of Mathematical Functions, With Formulas, Graphs, and Mathematical Tables*: Dover Publications, Inc.

2. Aoki, K. (1990). Approximate models of interdigitated array electrodes for evaluating steady-state currents. *Journal of Electroanalytical Chemistry and Interfacial Electrochemistry, 284*(1), 35-42

3. Aoki, K., Morita, M., Niwa, O., & Tabei, H. (1988). Quantitative analysis of reversible diffusion-controlled currents of redox soluble species at interdigitated array electrodes under steady-state conditions. *Journal of Electroanalytical Chemistry and Interfacial Electrochemistry, 256*(2), 269-282

4. Arslan, F., Ustabaş, S., & Arslan, H. (2011). An Amperometric Biosensor for Glucose Determination Prepared from Glucose Oxidase Immobilized in Polyaniline-Polyvinylsulfonate Film. *Sensors (Basel, Switzerland), 11*(8), 8152-8163

5. Arya, S. K., Zhurauski, P., Jolly, P., Batistuti, M. R., Mulato, M., & Estrela, P. (2018). Capacitive aptasensor based on interdigitated electrode for breast cancer detection in undiluted human serum. *Biosensors and Bioelectronics, 102*, 106-112

6. Ashish, V. J., Joan, C., & Jiang, Z. (2011). An impedimetric approach for accurate particle sizing using a microfluidic Coulter counter. *Journal of Micromechanics and Microengineering, 21*(4), 045036

7. Bard, A. J., Crayston, J. A., Kittlesen, G. P., Varco Shea, T., & Wrighton, M. S. (1986). Digital simulation of the measured electrochemical response of reversible redox couples at microelectrode arrays: consequences arising from closely spaced ultramicroelectrodes. *Analytical Chemistry, 58*(11), 2321-2331

8. Bard, A. J., & Faulkner, L. R. (2000). *Electrochemical Methods: Fundamentals and Applications*: Wiley.

9. Barnes, E. O., Lewis, G. E. M., Dale, S. E. C., Marken, F., & Compton, R. G. (2012). Generator-collector double electrode systems: A review. *Analyst, 137*(5), 1068-1081

10. Bhuiyan, R. H. M., Alam, N., Caicedo, J. M., & Ali, M. (2015). Real-Time Wireless Moisture Sensing in Concrete Using Interdigitated Stick-on Sensors. *Sensors & Transducers, 195*(12), 30-38

11. Bissell, C. C. C. C., & Chapman, D. A. D. A. (1992). *Digital signal transmission*: Cambridge University Press.

12. Bock, L. C., Griffin, L. C., Latham, J. A., Vermaas, E. H., & Toole, J. J. (1992). Selection of single-stranded DNA molecules that bind and inhibit human thrombin.
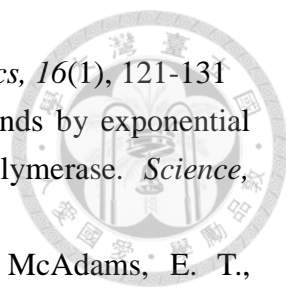
Nature, 355(6360), 564-566

13. Brosel-Oliu, S., Ferreira, R., Uria, N., Abramova, N., Gargallo, R., Muñoz-Pascual, F.-X., & Bratov, A. (2018). Novel impedimetric aptasensor for label-free detection of Escherichia coli O157:H7. *Sensors and Actuators B: Chemical, 255*, 2988-2995

14. Calixto, W. P., Alvarenga, B., da Mota, J. C., Brito, L. d. C., Wu, M., Alves, A. J., . . . Antunes, C. F. R. L. (2010). Electromagnetic Problems Solving by Conformal Mapping: A Mathematical Operator for Optimization. *Mathematical Problems in Engineering, 2010*, 19

15. Capaldo, P., Alfarano, S. R., Ianeselli, L., Zilio, S. D., Bosco, A., Parisse, P., & Casalis, L. (2016). Circulating Disease Biomarker Detection in Complex Matrices: Real-Time, In Situ Measurements of DNA/miRNA Hybridization via Electrochemical Impedance Spectroscopy. *ACS Sensors, 1*(8), 1003-1010

16. Chaubey, A., & Malhotra, B. D. (2002). Mediated biosensors. *Biosens Bioelectron, 17*(6-7), 441-456

17. Cheever, M. A., Allison, J. P., Ferris, A. S., Finn, O. J., Hastings, B. M., Hecht, T. T., . . . Matrisian, L. M. (2009). The prioritization of cancer antigens: a national cancer institute pilot project for the acceleration of translational research. *Clin Cancer Res, 15*(17), 5323-5337

18. Chen, L.-C., & Ho, K.-C. (2001). Interpretations of voltammograms in a typical two-electrode cell: application to complementary electrochromic systems. *Electrochimica Acta, 46*(13), 2159-2166

19. Chesney, D. J. (1996). Laboratory Techniques in Electroanalytical Chemistry, 2nd Edition Edited by Peter T. Kissinger (Purdue University) and William R. Heineman (University of Cincinnati). Dekker: Monticello, NY. 1996. xxii + 986 pp. $79. ISBN 0-8247-9445-1. *Journal of the American Chemical Society, 118*(44), 10946-10946

20. Chiriaco, M. S., Primiceri, E., D'Amone, E., Ionescu, R. E., Rinaldi, R., & Maruccio, G. (2011). EIS microfluidic chips for flow immunoassay and ultrasensitive cholera toxin detection. *Lab on a Chip, 11*(4), 658-663

21. Cho, H.-M., Park, Y. J., Yeon, J.-W., & Shin, H.-C. (2009). In-depth investigation on two- and three-electrode impedance measurements in terms of the effect of the counter electrode. *Electronic Materials Letters, 5*(4), 169-178

22. Cima, L. G. (1994). Receptors: Models for binding, trafficking and signaling. By Douglas A. Lauffenburger and Jennifer J. Linderman, Oxford University Press, 1993, $70.00. *AIChE Journal, 40*(6), 1089-1089

23. da Silva, E. T. S. G., Souto, D. E. P., Barragan, J. T. C., de F. Giarola, J., de Moraes,

A. C. M., & Kubota, L. T. (2017). Electrochemical Biosensors in Point-of-Care Devices: Recent Advances and Future Trends. *ChemElectroChem, 4*(4), 778-794

24. Daniels, J. S., & Pourmand, N. (2007). Label-Free Impedance Biosensors: Opportunities and Challenges. *Electroanalysis, 19*(12), 1239-1257

25. de la Rica, R., Fernández-Sánchez, C., & Baldi, A. (2006). Polysilicon interdigitated electrodes as impedimetric sensors. *Electrochemistry Communications, 8*(8), 1239-1244

26. Ding, S., Das, S. R., Brownlee, B. J., Parate, K., Davis, T. M., Stromberg, L. R., . . . Claussen, J. C. (2018). CIP2A immunosensor comprised of vertically-aligned carbon nanotube interdigitated electrodes towards point-of-care oral cancer screening. *Biosensors and Bioelectronics, 117*, 68-74

27. Ding, S., Mosher, C., Lee, X. Y., Das, S. R., Cargill, A. A., Tang, X., . . . Claussen, J. C. (2017). Rapid and Label-Free Detection of Interferon Gamma via an Electrochemical Aptasensor Comprising a Ternary Surface Monolayer on a Gold Interdigitated Electrode Array. *ACS Sensors, 2*(2), 210-217

28. Goode, J. A., Rushworth, J. V. H., & Millner, P. A. (2015). Biosensor Regeneration: A Review of Common Techniques and Outcomes. *Langmuir, 31*(23), 6267-6276

29. Grieshaber, D., MacKenzie, R., Vörös, J., & Reimhult, E. (2008). Electrochemical Biosensors - Sensor Principles and Architectures. *Sensors (Basel, Switzerland), 8*(3), 1400-1458

30. Groeber, F., Engelhardt, L., Egger, S., Werthmann, H., Monaghan, M., Walles, H., & Hansmann, J. (2015). Impedance spectroscopy for the non-destructive evaluation of in vitro epidermal models. *Pharmaceutical research, 32*(5), 1845-1854

31. Hambley, A. R. (2011). *Electrical engineering: principles and applications* (Vol. 2): Prentice Hall.

32. Hianik, T., & Wang, J. (2009). Electrochemical Aptasensors – Recent Achievements and Perspectives. *Electroanalysis, 21*(11), 1223-1235

33. Ivnitskii, D. M., & Rishpon, J. (1994). A potentiometric biosensor for pesticides based on the thiocholine hexacyanoferrate (III) reaction. *Biosensors and Bioelectronics, 9*(8), 569-576

34. Jacobsen, T., & West, K. (1995). Diffusion impedance in planar, cylindrical and spherical symmetry. *Electrochimica Acta, 40*(2), 255-262

35. Jiang, J., Wang, X., Chao, R., Ren, Y., Hu, C., Xu, Z., & Liu, G. L. (2014). Smartphone based portable bacteria pre-concentrating microfluidic sensor and impedance sensing system. *Sensors and Actuators B: Chemical, 193*, 653-659

36. Jin, S., Ye, Z., Wang, Y., & Ying, Y. (2017). A Novel Impedimetric Microfluidic

Analysis System for Transgenic Protein Cry1Ab Detection. *7*, 43175

37. Jolly, P., Formisano, N., Tkáč, J., Kasák, P., Frost, C. G., & Estrela, P. (2015). Label-free impedimetric aptasensor with antifouling surface chemistry: A prostate specific antigen case study. *Sensors and Actuators B: Chemical, 209*, 306-312

38. Keefe, A. D., Pai, S., & Ellington, A. (2010). Aptamers as therapeutics. *Nat Rev Drug Discov, 9*(7), 537-550

39. Kirby, B. J. (2010). *Micro- and Nanoscale Fluid Mechanics: Transport in Microfluidic Devices*: Cambridge University Press.

40. Kochowski, S., & Nitsch, K. (2002). Description of the frequency behaviour of metal–SiO2–GaAs structure characteristics by electrical equivalent circuit with constant phase element. *Thin Solid Films, 415*(1), 133-137

41. Lasia, A. (2002). Electrochemical Impedance Spectroscopy and its Applications. In B. E. Conway, J. O. M. Bockris, & R. E. White (Eds.), *Modern Aspects of Electrochemistry* (pp. 143-248). Boston, MA: Springer US.

42. Lim, T., Lee, S. Y., Yang, J., Hwang, S. Y., & Ahn, Y. (2017). Microfluidic biochips for simple impedimetric detection of thrombin based on label-free DNA aptamers. *BioChip Journal, 11*(2), 109-115

43. Lim, Y. C., Kouzani, A. Z., & Duan, W. (2010). Aptasensors: a review. *Journal of biomedical nanotechnology, 6*(2), 93-105

44. Liu, X., Qin, Y., Deng, C., Xiang, J., & Li, Y. (2015). A simple and sensitive impedimetric aptasensor for the detection of tumor markers based on gold nanoparticles signal amplification. *Talanta, 132*, 150-154

45. Lu, Y., Yao, Y., Zhang, Q., Zhang, D., Zhuang, S., Li, H., & Liu, Q. (2015). Olfactory biosensor for insect semiochemicals analysis by impedance sensing of odorant-binding proteins on interdigitated electrodes. *Biosensors and Bioelectronics, 67*, 662-669

46. Lum, J., Wang, R., Hargis, B., Tung, S., Bottje, W., Lu, H., & Li, Y. (2015). An Impedance Aptasensor with Microfluidic Chips for Specific Detection of H5N1 Avian Influenza Virus. *Sensors (Basel), 15*(8), 18565-18578

47. Malvano, F., Albanese, D., Pilloton, R., & Di Matteo, M. (2017). A new label-free impedimetric aptasensor for gluten detection. *Food Control, 79*, 200-206

48. Manczak, R., Fouet, M., Courson, R., Fabre, P.-L., Montrose, A., Sudor, J., . . . Reybier, K. (2016). Improved on-chip impedimetric immuno-detection of subpopulations of cells toward single-cell resolution. *Sensors and Actuators B: Chemical, 230*, 825-831

49. Marchenko, S. V., Kucherenko, I. S., Hereshko, A. N., Panasiuk, I. V., Soldatkin, O. O., El'skaya, A. V., & Soldatkin, A. P. (2015). Application of potentiometric

biosensor based on recombinant urease for urea determination in blood serum and hemodialyzate. *Sensors and Actuators B: Chemical, 207*, 981-986

50. Masel, R. I. (1996). *Principles of adsorption and reaction on solid surfaces*. New York: Wiley.

51. Mazlan, N. S., Ramli, M. M., Abdullah, M. M. A. B., Halin, D. S. C., Isa, S. S. M., Talip, L. F. A., . . . Murad, S. A. Z. (2017). Interdigitated electrodes as impedance and capacitance biosensors: A review. *AIP Conference Proceedings, 1885*(1), 020276

52. Morita, M., Hayashi, K., Horiuchi, T., Shibano, S., Yamamoto, K., & Aoki, K. (2014). Enhancement of Redox Cycling Currents at Interdigitated Electrodes with Elevated Fingers. *Journal of The Electrochemical Society, 161*(4), H178-H182

53. Mulder, W. H., Sluyters, J. H., Pajkossy, T., & Nyikos, L. (1990). Tafel current at fractal electrodes: Connection with admittance spectra. *Journal of Electroanalytical Chemistry and Interfacial Electrochemistry, 285*(1), 103-115

54. Nadja E Solis-Marcano, M. L.-N., Brismar Pinto-Pacheco, Carlos R. Cabrera. (2016). Capacitive Biosensing Technique for the Detection of DNA Modification and Hybridization Process Using Tailored Interdigital Microelectrode Arrays. *46th International Conference on Environmental Systems*(Electrochemistry Capacitance)

55. Niwa, O., Morita, M., & Tabei, H. (1990). Electrochemical behavior of reversible redox species at interdigitated array electrodes with different geometries: consideration of redox cycling and collection efficiency. *Analytical Chemistry, 62*(5), 447-452

56. Ohno, R., Ohnuki, H., Wang, H., Yokoyama, T., Endo, H., Tsuya, D., & Izumi, M. (2013). Electrochemical impedance spectroscopy biosensor with interdigitated electrode for detection of human immunoglobulin A. *Biosensors and Bioelectronics, 40*(1), 422-426

57. Orazem, M. E., & Tribollet, B. (2011). *Electrochemical Impedance Spectroscopy*: Wiley.

58. Punter-Villagrasa, J., Colomer-Farrarons, J., del Campo, F. J., & Miribel-Català, P. (2017). Introduction to Electrochemical Point-of-Care Devices. In J. Punter-Villagrasa, J. Colomer-Farrarons, F. J. del Campo, & P. Miribel (Eds.), *Amperometric and Impedance Monitoring Systems for Biomedical Applications* (pp. 1-26). Cham: Springer International Publishing.

59. Pursey, J. P., Chen, Y., Stulz, E., Park, M. K., & Kongsuphol, P. (2017). Microfluidic electrochemical multiplex detection of bladder cancer DNA markers. *Sensors and Actuators B: Chemical, 251*, 34-39

60. Radi, A.-E., Acero Sánchez, J. L., Baldrich, E., & O'Sullivan, C. K. (2005). Reusable Impedimetric Aptasensor. *Analytical Chemistry, 77*(19), 6320-6323

61. Rasooly, A. (2006). Moving biosensors to point-of-care cancer diagnostics. *Biosens Bioelectron, 21*(10), 1847-1850

62. Rasooly, A., & Jacobson, J. (2006). Development of biosensors for cancer clinical testing. *Biosens Bioelectron, 21*(10), 1851-1858

63. Reich, P., Stoltenburg, R., Strehlitz, B., Frense, D., & Beckmann, D. (2017). Development of An Impedimetric Aptasensor for the Detection of Staphylococcus aureus. *International journal of molecular sciences, 18*(11)

64. Rhinehardt, K., Mohan, R., Srinivas, G., & Kelkar, A. (2015, 7-10 March 2015). *Analysis and understanding of aptamer and peptide molecular interactions: Application to mucin 1 (Muc1) aptasensor.* Paper presented at the 2015 2nd International Symposium on Physics and Technology of Sensors (ISPTS).

65. Rogers, K. R. (2000). Principles of affinity-based biosensors. *Molecular biotechnology, 14*(2), 109-129

66. Romero, M. R., Ahumada, F., Garay, F., & Baruzzi, A. M. (2010). Amperometric Biosensor for Direct Blood Lactate Detection. *Analytical Chemistry, 82*(13), 5568-5572

67. Sexton, A. P. (2012, 2012//). *Abramowitz and Stegun – A Resource for Mathematical Document Analysis.* Paper presented at the Intelligent Computer Mathematics, Berlin, Heidelberg.

68. Shoar Abouzari, M. R., Berkemeier, F., Schmitz, G., & Wilmer, D. (2009). On the physical interpretation of constant phase elements. *Solid State Ionics, 180*(14), 922-927

69. Shoute, L. C. T., Anwar, A., MacKay, S., Abdelrasoul, G. N., Lin, D., Yan, Z., . . . Li, X. S. (2018). Immuno-impedimetric Biosensor for Onsite Monitoring of Ascospores and Forecasting of Sclerotinia Stem Rot of Canola. *Scientific Reports, 8*(1), 12396

70. Smith, S., Korvink, J. G., Mager, D., & Land, K. (2018). The potential of paper-based diagnostics to meet the ASSURED criteria. *RSC Advances, 8*(59), 34012-34034

71. Studier, F. W. (1969). Effects of the conformation of single-stranded DNA on renaturation and aggregation. *Journal of Molecular Biology, 41*(2), 199-209

72. Thévenot, D. R., Toth, K., Durst, R. A., & Wilson, G. S. (2001). Electrochemical biosensors: recommended definitions and classification1International Union of Pure and Applied Chemistry: Physical Chemistry Division, Commission I.7 (Biophysical Chemistry); Analytical Chemistry Division, Commission V.5

(Electroanalytical Chemistry).1. *Biosensors and Bioelectronics, 16*(1), 121-131

73.   Tuerk, C., & Gold, L. (1990). Systematic evolution of ligands by exponential enrichment: RNA ligands to bacteriophage T4 DNA polymerase. *Science, 249*(4968), 505

74.   Tweedie, M., Subramanian, R., Lemoine, P., Craig, I., McAdams, E. T., McLaughlin, J. A., . . . Kent, N. (2006, Aug. 30 2006-Sept. 3 2006). *Fabrication of impedimetric sensors for label-free Point-of-Care immunoassay cardiac marker systems, with passive microfluidic delivery.* Paper presented at the 2006 International Conference of the IEEE Engineering in Medicine and Biology Society.

75.   Valera, E., Ramón-Azcón, J., Rodríguez, Á., Castañer, L. M., Sánchez, F. J., & Marco, M. P. (2007). Impedimetric immunosensor for atrazine detection using interdigitated μ-electrodes (IDμE's). *Sensors and Actuators B: Chemical, 125*(2), 526-537

76.   Vandenryt, T., Pohl, A., van Grinsven, B., Thoelen, R., De Ceuninck, W., Wagner, P., & Opitz, J. (2013). Combining Electrochemical Impedance Spectroscopy and Surface Plasmon Resonance into one Simultaneous Read-Out System for the Detection of Surface Interactions. *Sensors (Basel, Switzerland), 13*(11), 14650-14661

77.   Vashist, S. K. (2017). Point-of-Care Diagnostics: Recent Advances and Trends. *Biosensors, 7*(4), 62

78.   Vericat, C., Vela, M. E., Benitez, G., Carro, P., & Salvarezza, R. C. (2010). Self-assembled monolayers of thiols and dithiols on gold: new challenges for a well-known system. *Chemical Society Reviews, 39*(5), 1805-1834

79.   Wang, J. (2006). Electrochemical biosensors: Towards point-of-care cancer diagnostics. *Biosensors and Bioelectronics, 21*(10), 1887-1892

80.   Wang, L., Veselinovic, M., Yang, L., Geiss, B. J., Dandy, D. S., & Chen, T. (2017). A sensitive DNA capacitive biosensor using interdigitated electrodes. *Biosensors and Bioelectronics, 87*, 646-653

81.   Wang, R., Wang, Y., Lassiter, K., Li, Y., Hargis, B., Tung, S., . . . Bottje, W. (2009). Interdigitated array microelectrode based impedance immunosensor for detection of avian influenza virus H5N1. *Talanta, 79*(2), 159-164

82.   Wang, Y., Ye, Z., Ping, J., Jing, S., & Ying, Y. (2014). Development of an aptamer-based impedimetric bioassay using microfluidic system and magnetic separation for protein detection. *Biosensors and Bioelectronics, 59*, 106-111

83.   Wang, Y., Ye, Z., & Ying, Y. (2012). New trends in impedimetric biosensors for the detection of foodborne pathogenic bacteria. *Sensors (Basel, Switzerland),*

12(3), 3449-3471

84. Weng, J.-H., Lai, C.-Y., & Chen, L.-C. (2019). Microfluidic amperometry with two symmetric Au microelectrodes under one-way and shuttle flow conditions. *Electrochimica Acta, 297*, 118-128

85. Wolfram Research, I. (©1998–2019a). The Wolfram Functions Site - JacobiCD. Retrieved from http://functions.wolfram.com/09.25.16.0043.01

86. Wolfram Research, I. (©1998–2019b). The Wolfram Functions Site - JacobiSN. Retrieved from http://functions.wolfram.com/09.36.16.0008.01

87. Xu, D., Xu, D., Yu, X., Liu, Z., He, W., & Ma, Z. (2005). Label-Free Electrochemical Detection for Aptamer-Based Array Electrodes. *Analytical Chemistry, 77*(16), 5107-5113

88. Xu, Y., Zhang, W., Shi, J., Zou, X., Li, Z., & Zhu, Y. (2016). Microfabricated interdigitated Au electrode for voltammetric determination of lead and cadmium in Chinese mitten crab (Eriocheir sinensis). *Food Chemistry, 201*, 190-196

89. Yan, X.-F., Wang, M.-H., & An, D. (2011). Progress of Interdigitated Array Microelectrodes Based Impedance Immunosensor. *Chinese Journal of Analytical Chemistry, 39*(10), 1601-1610

90. Yang, X., & Zhang, G. (2007). The voltammetric performance of interdigitated electrodes with different electron-transfer rate constants. *Sensors and Actuators B: Chemical, 126*(2), 624-631

91. Yuan, X.-Z., Song, C., Wang, H., & Zhang, J. (2010). EIS Equivalent Circuits *Electrochemical Impedance Spectroscopy in PEM Fuel Cells: Fundamentals and Applications* (pp. 139-192). London: Springer London.

92. Zhang, D., Jiang, J., Chen, J., Zhang, Q., Lu, Y., Yao, Y., . . . Liu, Q. (2015). Smartphone-based portable biosensing system using impedance measurement with printed electrodes for 2,4,6-trinitrotoluene (TNT) detection. *Biosens Bioelectron, 70*, 81-88

93. Zhang, D., Lu, Y., Zhang, Q., Liu, L., Li, S., Yao, Y., . . . Liu, Q. (2016). Protein detecting with smartphone-controlled electrochemical impedance spectroscopy for point-of-care applications. *Sensors and Actuators B: Chemical, 222*, 994-1002

94. Zhang, L., Dou, S. X., Liu, H. K., Huang, Y., & Hu, X. (2016). Symmetric Electrodes for Electrochemical Energy-Storage Devices. *Adv Sci (Weinh), 3*(12), 1600115-1600115

95. Zhou, J., & Rossi, J. (2016). Aptamers as targeted therapeutics: current potential and challenges. *Nature Reviews Drug Discovery, 16*, 181

96. Zhurauski, P., Arya, S. K., Jolly, P., Tiede, C., Tomlinson, D. C., Ko Ferrigno, P., & Estrela, P. (2018). Sensitive and selective Affimer-functionalised interdigitated

electrode-based capacitive biosensor for Her4 protein tumour biomarker detection. *Biosensors and Bioelectronics, 108*, 1-8

97.   Zou, Z., Kai, J., Rust, M. J., Han, J., & Ahn, C. H. (2007). Functionalized nano interdigitated electrodes arrays on polymer with integrated microfluidics for direct bio-affinity sensing using impedimetric measurement. *Sensors and Actuators A: Physical, 136*(2), 518-526

98.   Zou, Z., Lee, S., & Ahn, C. H. (2008). A Polymer Microfluidic Chip With Interdigitated Electrodes Arrays for Simultaneous Dielectrophoretic Manipulation and Impedimetric Detection of Microparticles. *IEEE Sensors Journal, 8*(5), 527-535

Appendices (Supplementary Material)

S.1 Detailed Derivations of Equations in Theory

S.1.1 Equation (10) to (12)

This section details the derivation process from eqn. (10) to (12). Note that

$$-K(m) + \beta i = F\left(\sin^{-1}\left(-\frac{\cos(x_e\pi/w)}{k}\right)|m\right) \tag{9}$$

$$\frac{w}{2} + y_{ICCB}i = \frac{w}{\pi}\cos^{-1}(-k \cdot sn(\beta i, m)) \tag{10}$$

$$y_{ICCB} = \frac{w}{\pi}\ln\left(\sqrt{s^2 - 1} + s\right) \tag{12}$$

$$s = \frac{\sin\left(\frac{w_e\pi}{2w}\right)}{\sin\left(\frac{x_e\pi}{w}\right)} \tag{13}$$

and $k = \cos(w_e\pi/(2w))$. There are also some formulae needed.

$$cd(z, m) = sn(K(m) + z, m) \tag{S1}$$

$$sn^{-1}(z, m) = F(\sin^{-1} z\,|m) \tag{S2}$$

$$cd(sn^{-1}(z, m), m)^2 = \frac{z^2 - 1}{mz^2 - 1} \tag{S3}$$

where $cd(z, m) = cd(z, k^2)$ is another Jacobi elliptic function. Therefore, by taking eqn.

(9) into (10) and applying eqn. (S1) ~ (S3), one can obtain

$$\frac{w}{2} + y_{ICCB}i = \frac{w}{\pi}\cos^{-1}\left(\pm\sqrt{\frac{\cos^2(x_e\pi/w) - k^2}{\cos^2(x_e\pi/w) - 1}}\right) = \frac{w}{\pi}\cos^{-1}\left(\pm\sqrt{1 - s^2}\right) \tag{S4}$$

The plus-minus sign is due to taking the square root of eqn. (S3), and whether the value

at the right is positive or not cannot be determined here. Still, the $1 - s^2$ inside the square

root of eqn. (S4) is negative, so the following complex relationships are needed.

$$\cos^{-1}(z) = -i \operatorname{Log}\left(z + \sqrt{z^2 - 1}\right) \tag{S5}$$

$$\operatorname{Log}(z) = \ln|z| + i\operatorname{Arg}(z) \tag{S6}$$

Eqn. (S4) thus equals

$$\frac{w}{2} + y_{ICCB}i = -i\frac{w}{\pi}\operatorname{Log}\left(\pm i\sqrt{s^2 - 1} + \sqrt{-s^2}\right) = -i\frac{w}{\pi}\operatorname{Log}\left(i\left(\pm\sqrt{s^2 - 1} + s\right)\right)$$

$$= -i\frac{w}{\pi}\left(\ln\left(\pm\sqrt{s^2 - 1} + s\right) + i\frac{\pi}{2}\right) = \frac{w}{2} - i\frac{w}{\pi}\ln\left(\pm\sqrt{s^2 - 1} + s\right) \tag{S7}$$

Because $y_{ICCB} \geq 0$, so in eqn. (S7), it must be that $\ln\left(\pm\sqrt{s^2 - 1} + s\right) \leq 0$. This is only

possible if

$$\ln\left(-\sqrt{s^2 - 1} + s\right) = -\ln\left(\left(-\sqrt{s^2 - 1} + s\right)^{-1}\right) = -\ln\left(\sqrt{s^2 - 1} + s\right) \leq 0 \tag{S8}$$

because $\sqrt{s^2 - 1} + s \geq 1$. At last, substitution of eqn. (S8) into (S7) yields eqn. (12).

S.1.2 Equation (12) and (13) to (20)

This section details the process for finding the derivative of $-y_{ICCB}$ with respect to x_e.

From eqn. (12), it can be derived that

$$-\frac{dy_{ICCB}}{dx_e} = -\frac{w}{\pi}\frac{1}{\sqrt{s^2 - 1} + s}\frac{d\left(\sqrt{s^2 - 1} + s\right)}{dx_e} = -\frac{w}{\pi}\frac{1}{\sqrt{s^2 - 1} + s}\left(\frac{s}{\sqrt{s^2 - 1}} + 1\right)\frac{ds}{dx_e} \tag{S9}$$

and from eqn. (13),

$$\frac{ds}{dx_e} = -\frac{\sin\left(\frac{w_e\pi}{2w}\right)}{\sin^2\left(\frac{x_e\pi}{w}\right)} \cdot \frac{\pi}{w}\cos\left(\frac{x_e\pi}{w}\right) = -s\frac{\pi}{w}\cot\left(\frac{x_e\pi}{w}\right) \tag{S10}$$

Substituting eqn. (S10) into (S9), eqn. (20) can be derived. Note that the w/π in eqn. (S9)

and the π/w in eqn. (S10) have been canceled, resulting in a dimensionless value.

132

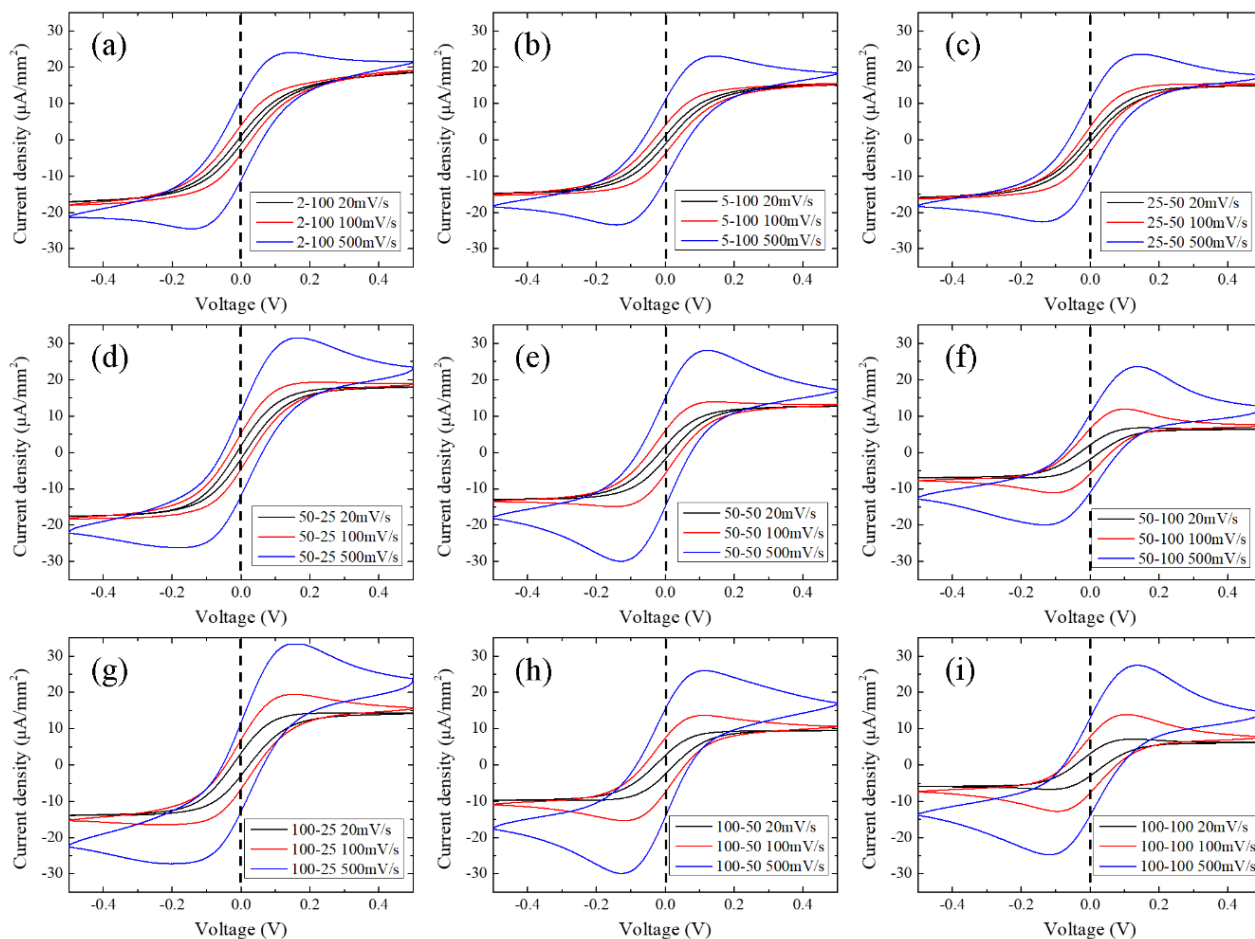## S.2 The Potential Symmetry of IDA Electrodes

Figure S1 Cyclic voltammograms for the nine fabricated chips. The dimension in the legends is w_g-w_e (μm) and the value to the right of them are the scan rates. Four consecutive cycles are scanned in each experiment and the last one is plotted out. The pairs of peak voltages are all symmetric about 0V (vs CE/RE).

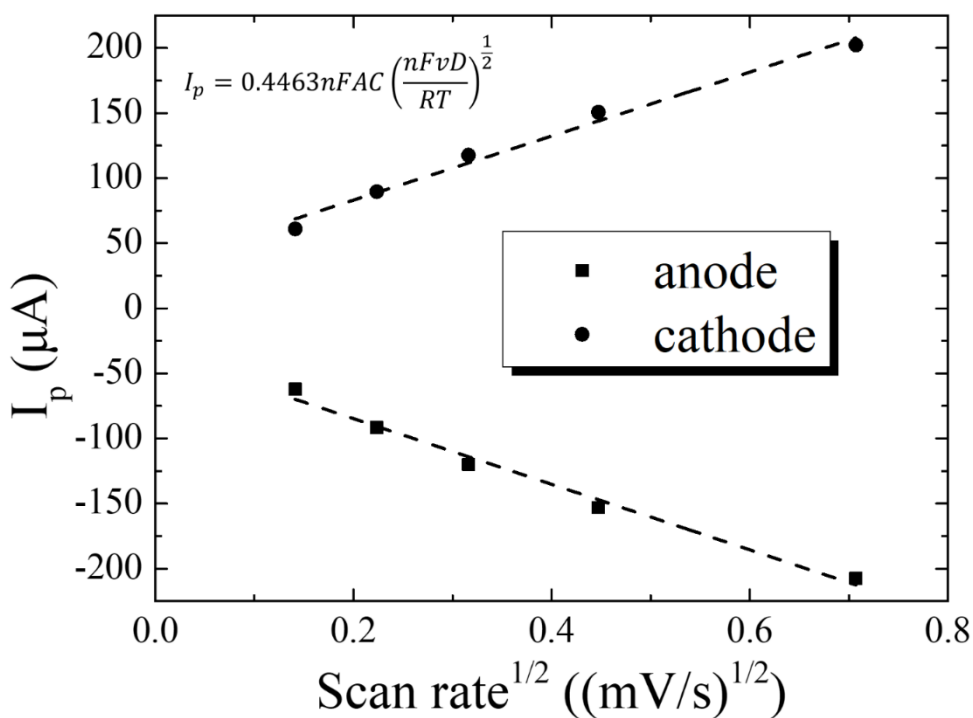**S.3 Diffusion Coefficient Calculation using Randles-Sevcik Equation**

Figure S2 Peak current plotted against the positive square root of the scan rate. Cyclic voltammetry is performed using a three electrode setup (WE: bare standard Au electrode, CE: Pt electrode and RE: Ag/AgCl electrode) in a solution of 5mM $Fe(CN)_6^{3-/4-}$ and 0.1M KCl. Several experiments using different standard Au electrodes at different time points are carried out and $D_O=D_R=D$ is calculated as $(6\pm3)\times10^{-10}m^2/s$ using the Randles-Sevcik equation (top-left equation).
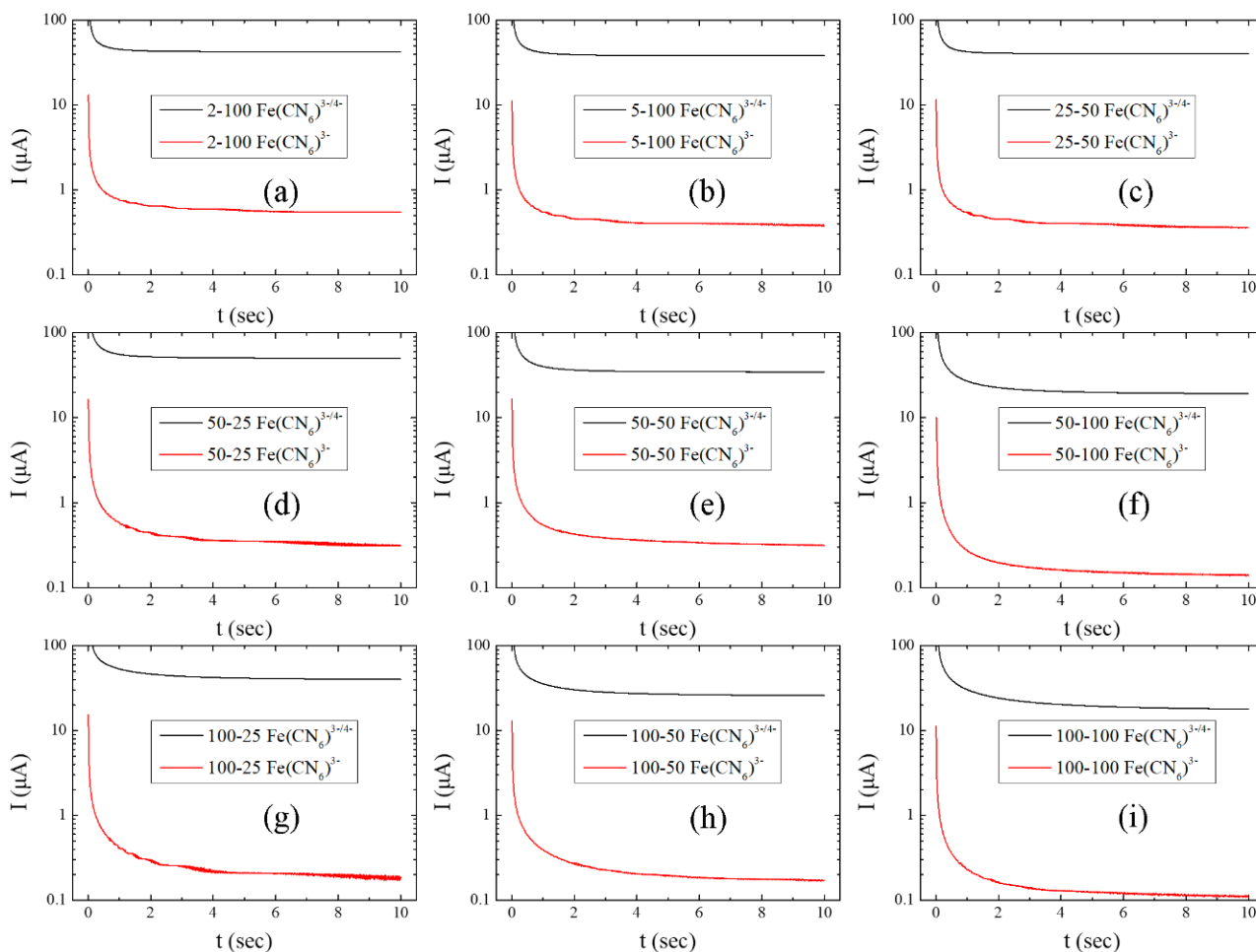
S.4 Limiting Current of IDA Electrodes

Figure S3 Current plotted against time in chronoamperometry experiments. The dimension in the legends is w_g-w_e (µm) and the concentration of redox species is 5mM for either $Fe(CN)_6^{3-/4-}$ (black line) or $Fe(CN)_6^{3-}$ (red line). 0.1M KCl is also added to the solution.

S.5 Comparison of Electrode Compositions in Two and Three Electrode Systems

The characteristic "potential symmetric" is arbitrarily defined as the situation when cyclic voltammetry shows a standard potential (E^0) of 0V (vs RE). Cyclic voltammetry is performed on different electrochemical setup systems using bare standard Au electrodes as working electrodes (Figure S4). When only $Fe(CN)_6^{3-}$ is present, no configuration can yield a clear two-peak cyclic voltammogram with potential symmetry. Although when both $Fe(CN)_6^{3-}$ and $Fe(CN)_6^{4-}$ are present, potential symmetry can be accomplished by two or three-electrode setups when Au is used as pseudo reference. From the experiment results and previous knowledge, it is concluded that two conditions are needed for clear potential symmetry, at least for this system: (1) Both redox species with equal bulk concentration must be present in solution and (2) the reference and working electrode must exhibit the same redox reaction. This is quite obvious due to the fact that when these two conditions are agreed, according to the Nernst equation, an initial condition is met:

$$E_{WE} = E_{RE} = E_0 + \frac{RT}{nF} \ln \frac{a_{Red}}{a_{Ox}} = E_0' + \frac{RT}{nF} \ln \frac{C_R(x=0)}{C_O(x=0)} = E_0' \qquad (S11)$$

where E_{WE} and E_{RE} are the electrode potentials, E_0 is the standard potential, and a_R and a_O are the activities of the reduced and oxidized species on the electrode surface. When cyclic voltammetry is performing, an equal bulk concentration of both redox species can contribute the working electrode symmetrical reaction while sweeping positive or negative. Thus, a clear two-peak closed curve can be formed.
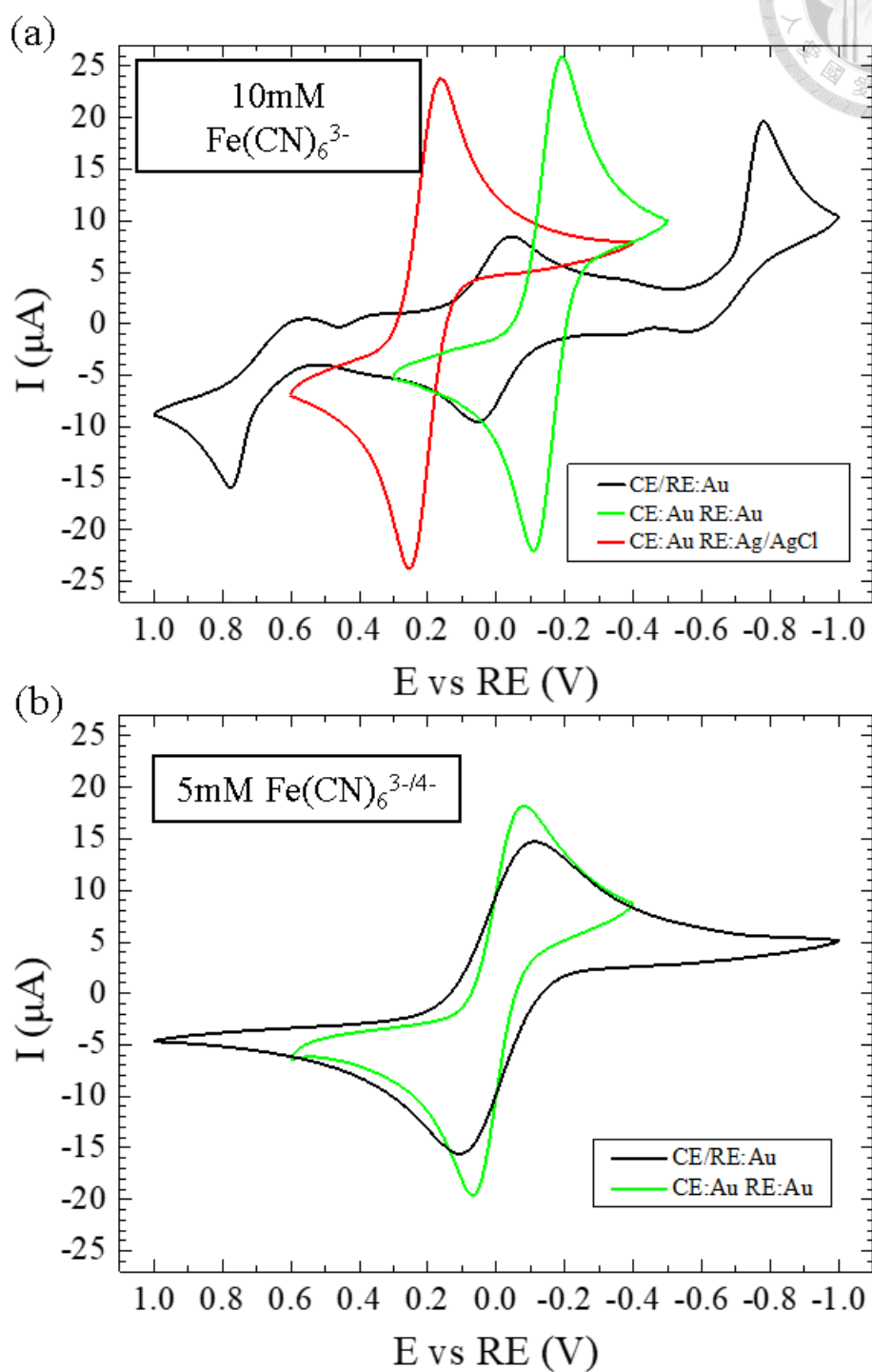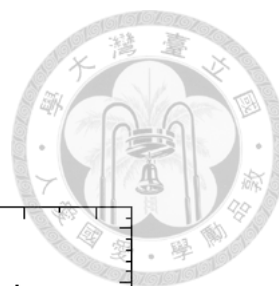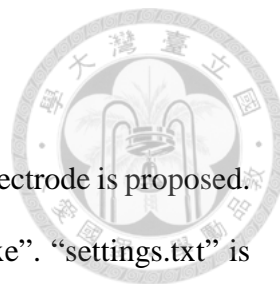
136

Figure S4 Cyclic voltammograms of two and three electrode setups in a solution of 0.1M KCl and (a) 10mM $Fe(CN)_6^{3-}$ or (b) 5mM $Fe(CN)_6^{3-/4-}$ with the legends indicating the electrode material. The WE is always a bare standard Au electrode (ϕ=2mm).

137

S.6 IDA Diffusion Impedance Calculation Program

A program for calculating the diffusion impedance for an IDA electrode is proposed.

The program consists of two files "settings.txt" and "IDA_diff_Z.exe". "settings.txt" is

of the format below:

```
// please do not change the order of the settings
// invalid format of this file might cause unknown failure

// output settings (1:yes 0:no)
[output to txt file] 0

// EIS settings
[max freq (Hz)] 100000
[min freq (Hz)] 0.01
[points per decade] 3

// geometry settings
[electrode bandwidth we (um)] 25
[gap width wg (um)] 50
[electrode length l (mm)] 3
[number of bands N] 80

// redox species properties
[diffusion coefficient D (m^2/s)] 6e-10
[bulk concentration C* (mM)] 5
[number of electrons n] 1

// environment settings
[temperature T (K)] 298.0
```

These contain all the 12 parameters for the usage of this program. A detailed description

is listed in order below:

1. If [output to txt file] is 0, then calculated impedances will be shown directly on screen. If it is 1, then the values will be saved to the file "Z_diffusion_IDA.txt".
2. The maximum frequency for impedance calculation can be set after [max freq (Hz)].
3. The minimum frequency for impedance calculation can be set after [min freq (Hz)].
4. The number of frequency points within a decade can be set (e.g. If [points per decade] is set to 5, then frequencies calculated between 10^1 and 10^0Hz will be 10^1, $10^{0.8}$, $10^{0.6}$, $10^{0.4}$, $10^{0.2}$ and 10^0Hz.)
5. w_e can be set after [electrode bandwidth we (um)].
6. w_g can be set after [gap width wg (um)].
7. l can be set after [electrode length l (mm)].

138

8. *N* can be set after [number of bands N].

9. *D* can be set after [diffusion coefficient D (m^2/s)].

10. C^* can be set after [bulk concentration C* (mM)].

11. *n* can be set after [number of electrons n].

12. *T* can be set after [temperature T (K)].

After setting the 12 parameters, put "settings.txt" and "IDA_diff_Z.exe" in the same directory and open "IDA_diff_Z.exe". Impedances will be automatically calculated and printed in the defined format (Figure S5).

※The program can only be run in a Windows 64-bit environment.


```
Output to file : NO
-------------------------------------------------
Max frequency (Hz) : 100000.000000
Min frequency (Hz) : 0.010000
Points per decade : 3
-------------------------------------------------
Electrode bandwidth (um) : 25.000000
Gap width (μm) : 50.000000
Electrode length (mm) : 3.000000
Number of bands : 80
-------------------------------------------------
Diffusion coefficient (m^2/s) : 6.000000e-010
Bulk concentration (mM) : 5.000000
Number of electrons : 1
-------------------------------------------------
Temperature (K) : 298.000000
-------------------------------------------------

Initializing Bessel Functions ...
10%    20%    30%    40%    50%    60%    70%    80%    90%    100%    DONE
Initializing Elliptic Integral Functions ...
10%    20%    30%    40%    50%    60%    70%    80%    90%    100%    DONE

     Freq (Hz)      Re(Z) (Ω)      Im(Z) (Ω)         |Z| (Ω)         Phase (°)
 100000.000000          2.584         -2.577           3.649          -44.9188
  46415.888352          3.793         -3.777           5.353          -44.8811
  21544.346915          5.567         -5.533           7.849          -44.8259
  10000.000010          8.171         -8.098          11.504          -44.7455
   4641.588840         11.992        -11.837          16.850          -44.6287
   2154.434694         17.598        -17.269          24.656          -44.4595
   1000.000002         25.821        -25.124          36.028          -44.2161
    464.158884         37.873        -36.406          52.534          -43.8686
    215.443470         55.510        -52.452          76.371          -43.3777
    100.000000         81.250        -74.959         110.546          -42.6938
     46.415888        118.631       -105.913         159.031          -41.7583
     21.544347        172.459       -147.338         226.827          -40.5084
     10.000000        248.897       -200.748         319.765          -38.8878
      4.641589        355.152       -266.295         443.898          -36.8628
      2.154435        498.141       -341.654         604.046          -34.4446
      1.000000        683.063       -425.475         804.739          -31.9184
      0.464159        929.584       -510.304        1060.441          -28.7650
      0.215443       1245.934       -540.505        1358.122          -23.4519
      0.100000       1556.807       -456.564        1622.374          -16.3448
      0.046416       1759.923       -299.946        1785.300           -9.6721
      0.021544       1846.646       -161.572        1853.701           -5.0003
      0.010000       1872.035        -78.395        1873.676           -2.3980

請按任意鍵繼續 . . .
```

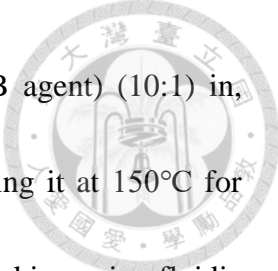Figure S5 An example output of the IDA diffusion impedance calculation program.

S.7 Real-time Impedimetric MUC1 Aptasensor using Microfluidic IDA Chips

S.7.1 Microfluidic System Integration

The photomasks of different widths of microfluidic channels are designed and fabricated similar to the method in section 0. This time, a negative photoresist (SU-8 2050) is used for microfabrication. A 4" silicon wafer is washed respectively with 10min acetone, isopropanol (IPA) and distilled water in an ultrasonic cleaner and are subsequently blown with air and dried on a 120℃ hot plate. SU8-2050 (stored in RT) is taken out and carefully poured onto the cooled wafer to form a uniform thin layer covering almost all the areas. The wafer is spin coated at 500rpm 10s and 1600rpm 50s then soft baked at 65℃ 5min and 95℃ 16min and cooled at RT. The wafer is then exposed for 110s (6mW) (in contact with the photomask) and immediately baked at 65℃ 5min and 95℃ 9min 12s. After baking, it is immersed in SU-8 developer for 8min 48s with continuous gentle shake of the container to obtain better developing effect then taken out, rinsed with IPA and dried with airflow. If the wafer is not clean enough, a second developing stage can be implemented. Hard bake of 160℃ is given on a hot plate for 30min.

After cooling of the wafer, a pattern for PDMS molding should appear on it with a height of ~100μm which can retain its structure after several time of molding. The microfluidic channel is made by using aluminum foil to fold out a wall at the sides of the

140

wafer, pouring the mixed prepolymer (A agent) and crosslinker (B agent) (10:1) in, vacuum sucking (~2hr) to remove bubbles in the mixture and heating it at 150°C for 10min on a hot plate. After cooling, the PDMS is cut in pieces making microfluidic channels with different widths. At last, the microfluidic channels are punched holes (1mm Φ) for inlet and outlet using a dermal punch. The final dimension of the microfluidic chip is 25(L)×19(W)×6(H) mm^3.

The microfluidic channel can be clipped onto the electrode chip which the fixture is designed with different heights using the same technical drawing software for the photomask and is 3D printed and polished. For the setup of the overall microfluidic electrochemical system, a silicon tube is pricked into the inlet and connected to a syringe (2.5mL) which is installed on a syringe pump and another tube is pricked into the outlet and connected to the bottom of a tube. Continuous flow in the channel can be realized by withdrawal of the syringe at a constant flow rate while continuously adding fluid to the tube.

S.7.2 Impedimetric Aptasensing of Target Protein

The target protein (thrombin, MUC1 or BSA) is detected using impedimetric methods with the sensing element immobilized on either standard Au electrodes (section 4.3.5) or the microfluidic integrated IDA electrode chip. As for the case of standard Au electrodes, the Au electrodes are dipped in different solutions containing various concentrations of the target protein in binding buffer for 30min. They are washed using the same method as the aptasensor fabrication process and are immediately characterized using EIS. For real-time detection of MUC1 using the microfluidic integrated IDA electrode chip, 10μM BSA in binding buffer is flown through the channel at a rate of 0.2μL/s for blocking and reducing non-specific binding. Afterwards, 200nM MUC1-peptide in binding buffer is flown through at 0.2μL/s. Real-time data are acquired at each stage.
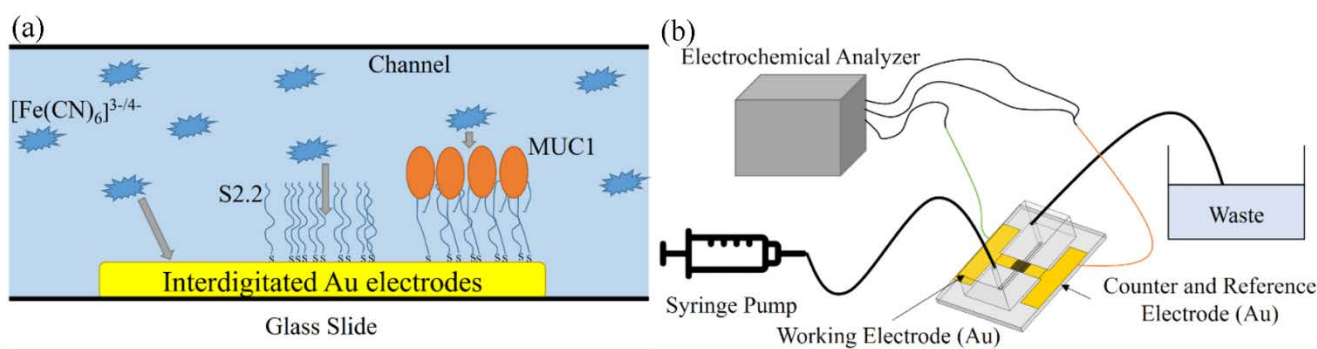
Figure S6 (a) Schematic of MUC1 impedimetric aptasensing using $Fe(CN)_6^{3-/4-}$ as the redox species in a microfluidic channel, (b) microfluidic system and electrochemical setup of this study.

S.7.3 Characterization of IDA Electrode Microfluidic Chip

Interdigitated array electrodes of 100μm width each and 25μm apart are fabricated

and the straight channel of 0.5mm width and ~100μm height is fabricated using SU-8 soft

lithography and PDMS molding. A significant difference is present between 0μL/s and

other flow rates in the cyclic voltammogram of the microfluidic Au interdigitated

electrodes (Figure S7). This is due to the active $Fe(CN)_6^{3-/4-}$ surface refresh in flowing

conditions (Weng et al., 2019). Furthermore, at 0μL/s, the increase in scan rate enhances

the current while scan rates at other speeds don't. Although a higher flow rate can result

in a high current, the volume of sample used will increase.
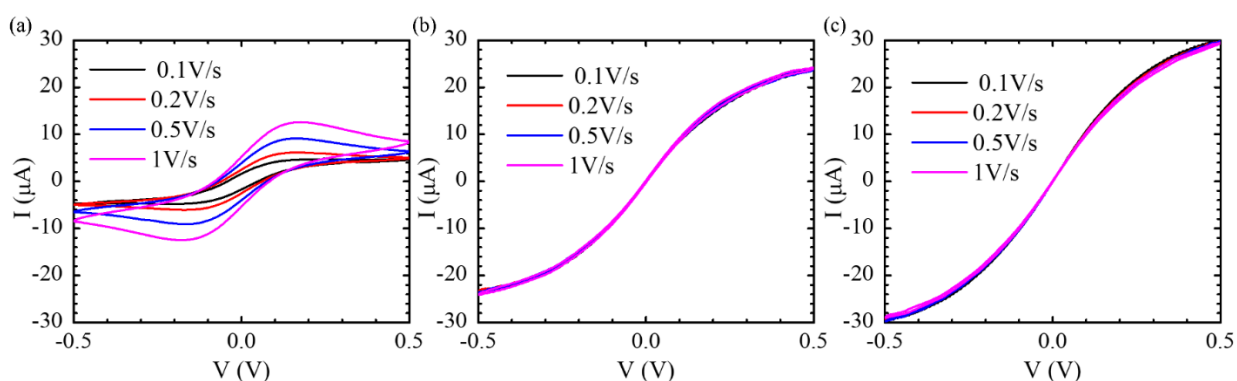
Figure S7 Cyclic voltammogram on microfluidic bare Au electrode comparing different flow rates and scan rates. (a) 0μL/s, (b) 0.2μL/s and (c) 0.4μL/s. The solution is 5mM $Fe(CN)_6^{3-/4-}$ in 10mM Tris-HCl buffer (5mM $MgCl_2$, 50mM KCl, pH 7.4).

S.7.4 Real-Time EIS Detection Frequency Optimization

The effect of impedance influenced by flow speed is secondly characterized by EIS. Nyquist and Bode plots are of EIS data of an IDA microfluidic chip at different flow rates are plotted in Figure S8. Overall, an increase in flow rate results in a decrease in total impedance and phase angle at low frequencies. At 0μL/s, the plot resembles a typical pattern for the IDA electrode, which has a bending of impedance at low frequencies. However, there is one major difference: the solution height is finite. This does not correspond to assumption V in section 3.2. So analysis methods cannot be directly implemented (Nevertheless, it is reasonable to predict that the imaginary constant concentration boundary (ICCB) would be the same even with finite heights.). As the flow rate increases, the impedance bend towards the real axis at higher frequencies. If there exists an ICCB when the flow rate is larger than 0μL/s, then the finite diffusion length is predicted to be shorter as the flow rate increases. But it shouldn't be a vertical line. Instead, it should be approximately perpendicular to the flow direction because redox species should be "refreshed" and the refresh rate should have a positive correlation with the flow rate. This is particularly interesting and can be a major subject targeting the modeling of finite diffusion phenomenon of IDA electrodes within a convective force applied microfluidic channel.
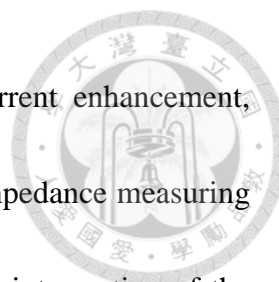
In order to achieve balance between sample usage and current enhancement, 0.2μL/s is chosen as the optimal flow rate. The optimal real-time impedance measuring frequency is arbitrarily chosen as 100Hz, which corresponds to the intersection of the charge transfer and diffusion limiting region.
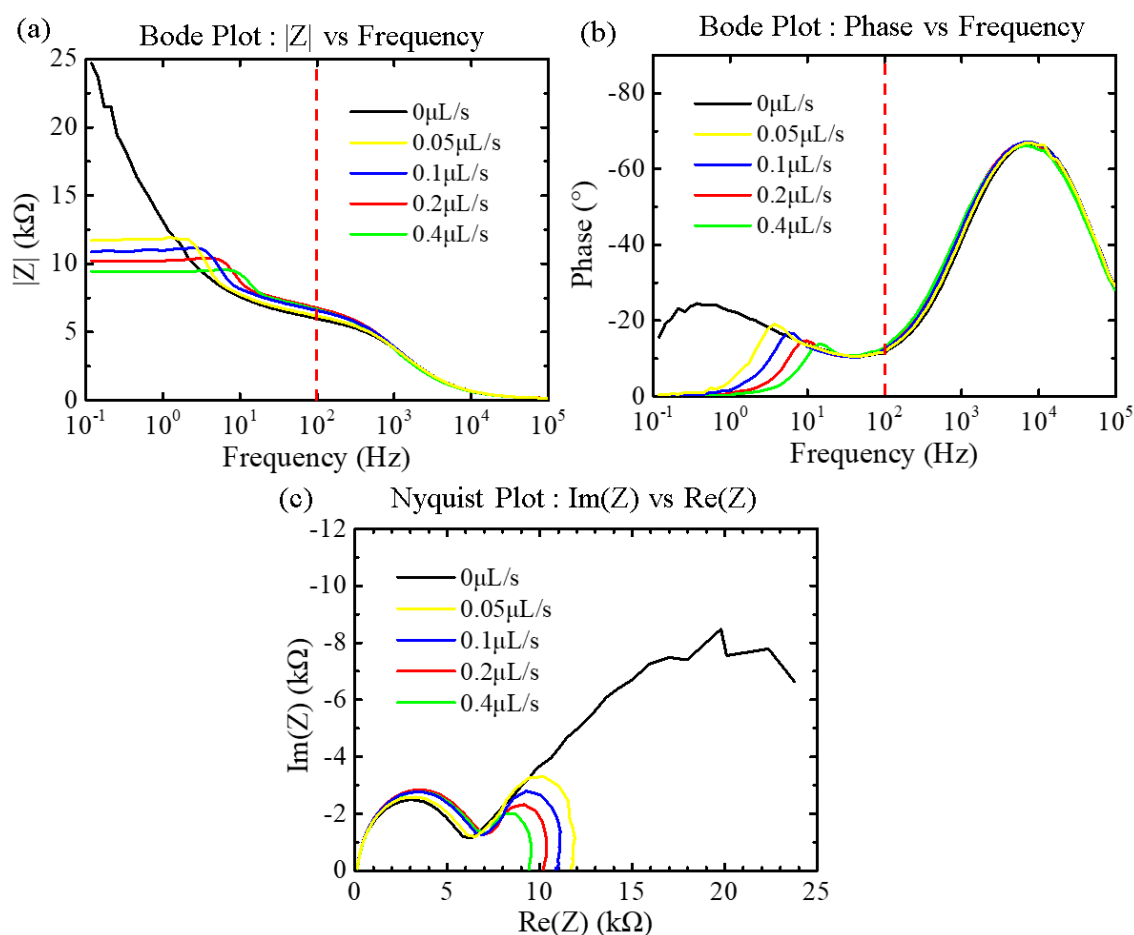

Figure S8 EIS spectra on microfluidic bare Au electrode comparing different flow rates. (a) |Z| vs frequency, (b) Phase vs frequency bode plot and (c) Nyquist plot. $E_{init} = 0V$, $V_{amp} = 5mV$, 5mM $Fe(CN)_6^{3-/4-}$ in 10mM Tris-HCl buffer (5mM $MgCl_2$, 50mM KCl, pH 7.4).

S.7.5 Real-Time Impedimetric Aptasensing of MUC1

Lastly, real-time impedimetric aptasensing of MUC1 is realized by applying the parameters previously set. Figure S9 plots the $|Z|$, phase, Re(Z) and Im(Z) vs time. It can be seen that $|Z|$ and the phase increased after aptamer immobilization, although the further increase in impedance after BSA flow-through indicates a strong non-specific binding to the not fully covered Au electrode. MUC1 binding results an increase in phase angle and Im(Z) and a decrease in Re(Z). The results show four kinds of values for analyzing the impedance against time and demonstrates that a potential future of miniaturized bio-sensing chips using novel electrode structures for medical care and environmental detection is on the move.

146
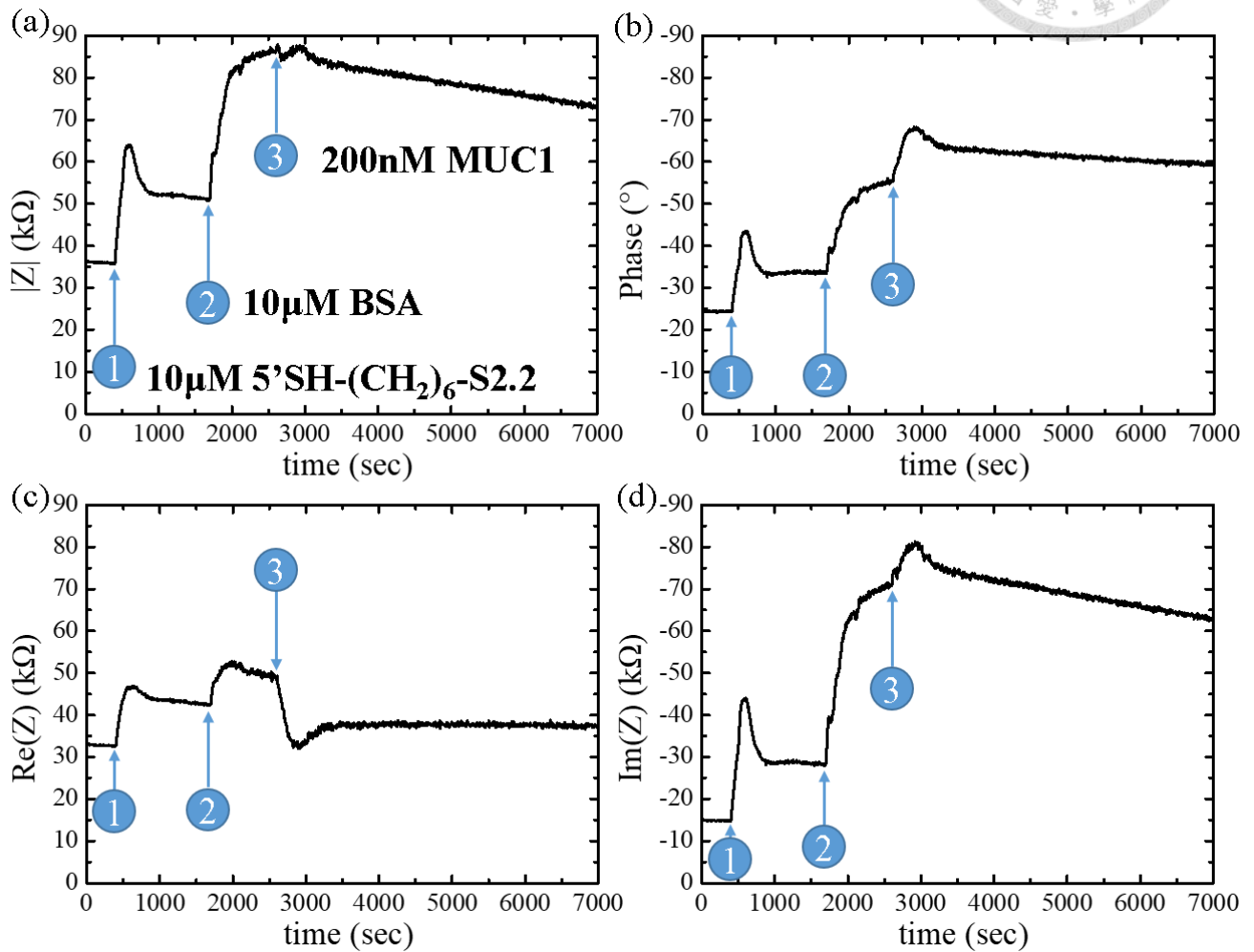
Figure S9 Plots of Real-time impedimetric aptasensing of MUC1. (a) |Z| vs time, (b) Phase vs time, (c) Re(Z) vs time and (d) Im(Z) vs time. Frequency = 100Hz, V_{amp} = 5mV, flow rate = 0.2μL/s and all samples are dissolved in 10mM Tris-HCl buffer.

S.8 Portable Devices for Integrated Bio-Sensing Platforms

Nothing can be portable with bulky lab instrumentation. An electrochemical sensor chip always needs a device or instrument for performing data acquisition of its value, therefore the miniaturization of instrumentation or device should be a major demand for portable systems that can meet the ASSURED criteria pointed out by the world health organization (Smith et al., 2018). In the following paragraphs, the development of electrochemical impedance detection instruments is stated and the design and concepts are detailed. Two generations are developed in this thesis which are, generation α and β. Both exhibiting different design concepts and goals to achieve. Generation α serve as the foundation for construction of a real-time impedimetric detection system that can measure impedances from $10^{-1} \sim 10^4$Hz. Generation β improves several features of generation α include quantitative ones such as the frequency range, impedance range, detection time and detection repeatability. A website is constructed for controlling the system and acquiring real-time data in generation β so that any remote user can log in using smart devices without the need for installing any apps or services. This is particularity useful regarding portability and usage convenience, and is highly competitive for integrated biosensors playing a role in internet of things (IoT) technologies.

S.8.1 Generation α (Z_GENα)

S.8.1.1 Preface and Concepts

In this generation, the goal for developing a device that has the ability for mimicking the impedance measuring ability of a typical electrochemical analyzer is set. The general scheme is depicted in Figure S10. A function generator is used for producing sine voltage waves across the symmetric electrode, then a DAQ device (USB-6210) is used for collecting voltage signals from the circuitry. The signal is processed and sent to the connected computer for data analysis and plotting. For being the first "pre" generation developed, the targets are of the easiest which stricter targets are set in generation β.
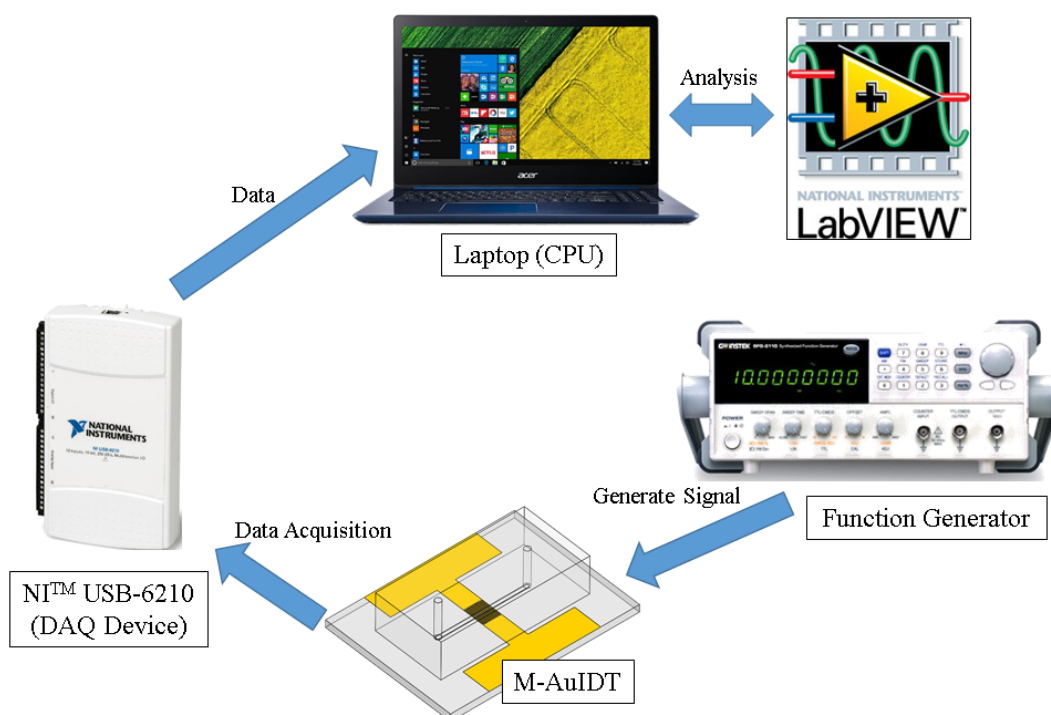
Figure S10 General scheme for real-time impedimetric detection system (Z_GENα)

S.8.1.2 Schematic Design

As for generating an amplitude of 5mV, a voltage divider using an operational amplifier (op-amp) is firstly connected to the output of the function generator and the output of the op-amp is split and connected to one end of the electrode chip and the DAQ device. The other end of the chip is connected to the inverting input of another op-amp for amplifying the current flowing through the chip induced by the applied voltage. The amplified current is transformed to voltage and acquired by the DAQ device and then sent to the computer for further manipulation. For being rather a rough and elementary system, the detailed schematic is not shown.

S.8.1.3 LabVIEW Data Analysis Design

The block diagram and front panel of the LabVIEW data analysis procedure are depicted in Figure S11. There are two signals obtained by the DAQ device: the input voltage and the amplified current (measured in voltages) of the electrode chip. When the amplification ratio of the current is known, we can calculate the current by dividing the measured voltage with the known ratio. The frequency is the same as the manually set input or can also be calculated using Fourier transform of the two signals. The absolute impedance ($|Z|$) can be found by dividing the amplitude of the input voltage by the calculated current and the phase can be found by calculating the relative phase between

150
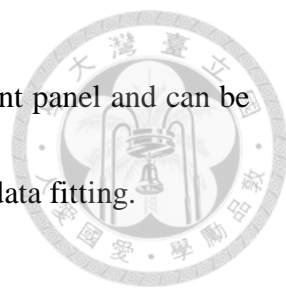
the two signals. These two values are plotted on the graph in the front panel and can be saved as comma-separated values (.csv) that can be further used for data fitting.
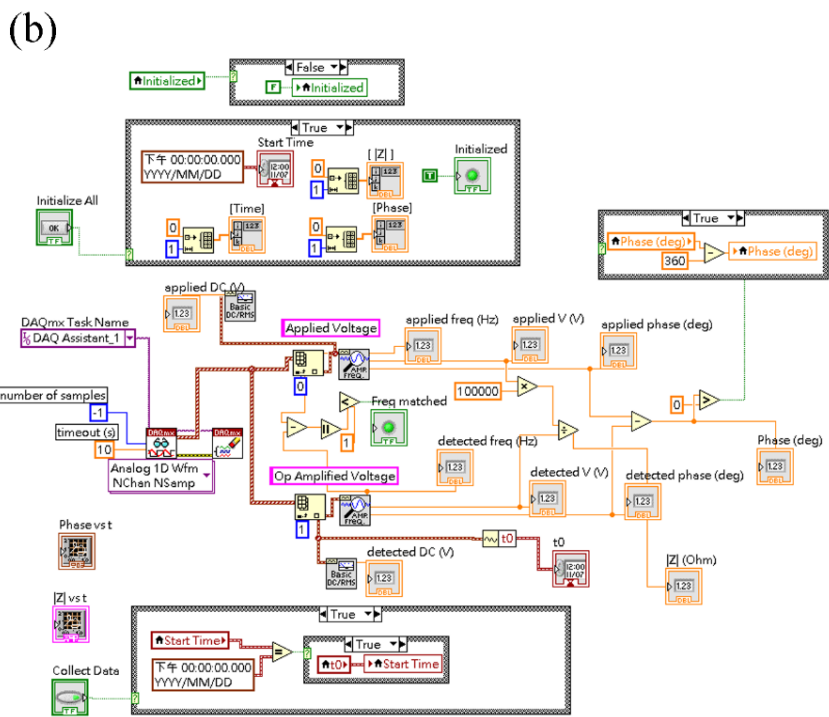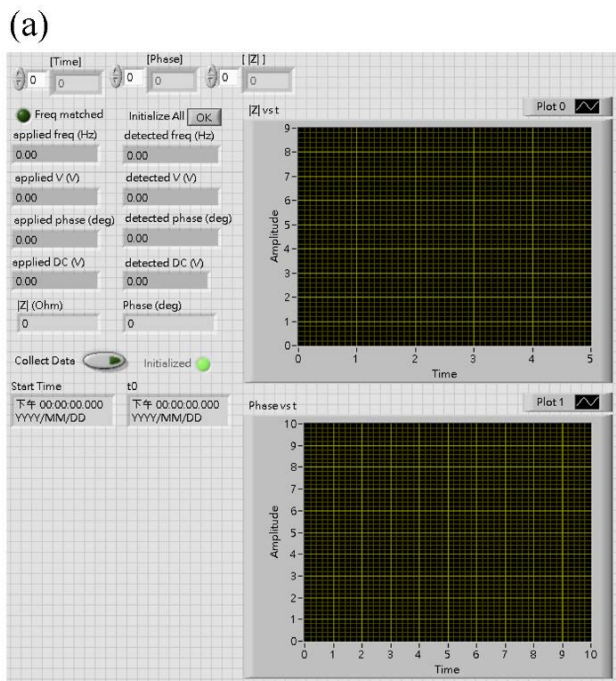

Figure S11 (a) Control panel and (b) block diagram for impedance measurement of Z_GENα using DAQ device and LabVIEW software

S.8.1.4 Stability Test for Impedance Detection using Z_GENα

Figure S12 plots the real-time impedance value obtained using Z_GENα. A microfluidic IDA chip (w_g/w_e = 25/100μm) is used. The flow rate is 0.1μL/s and the applied frequency is 100Hz. One can see erroneous values in $|Z|$ and phase throughout the sensing duration. For Z_GENα, the impedance values are not stable enough, the equipment is bulky, the applied frequency cannot be automatically controlled during detection, and the available detection frequency range is small ($10^{-1} \sim 10^4$Hz). The problems are addressed in the next generation.
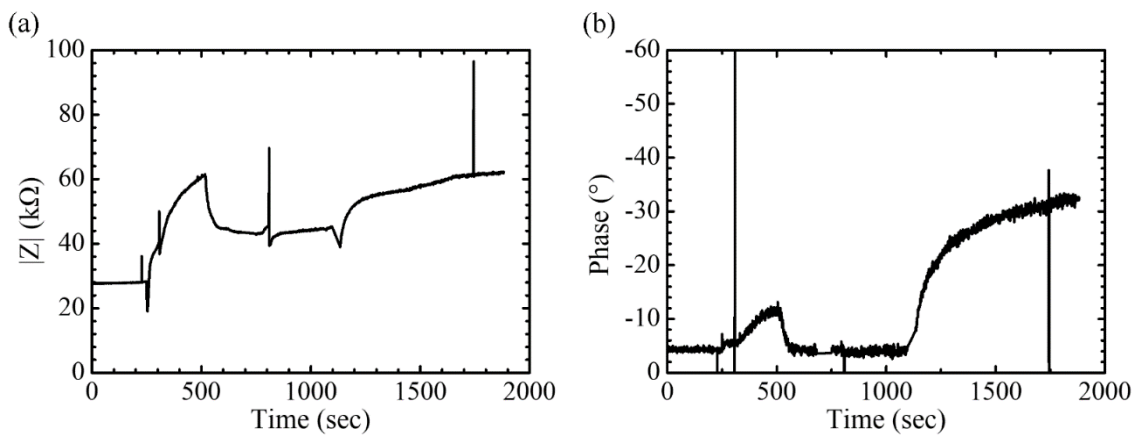
Figure S12 (a) $|Z|$ vs t and (b) phase vs t for real-time impedimetric detection using Z_GENα.

S.8.2 Generation β (Z_GENβ)

S.8.2.1 Preface and Concepts

Usually, the determination of the impedance phase of a signal requires measuring

the input voltage and output current at the same time, the phase is hard to calculate using

only a single input. However, if a DAQ device can realize continuous measurements from

the start of measurement and apply a sinusoidal wave which the phase always commences

from a constant value (say 0°), phase measurement may be accomplished by using just

one single input, which is a major concept for the design of Z_GENβ. The target set for

it has a whole list of goals in addition to the main features of a typical impedance analyzer:

miniaturization, portable, real-time, low-cost and user-friendly. The scheme of Z_GENβ

is illustrated, which a Raspberry Pi 3 b+ is used as the CPU for integrating circuitry

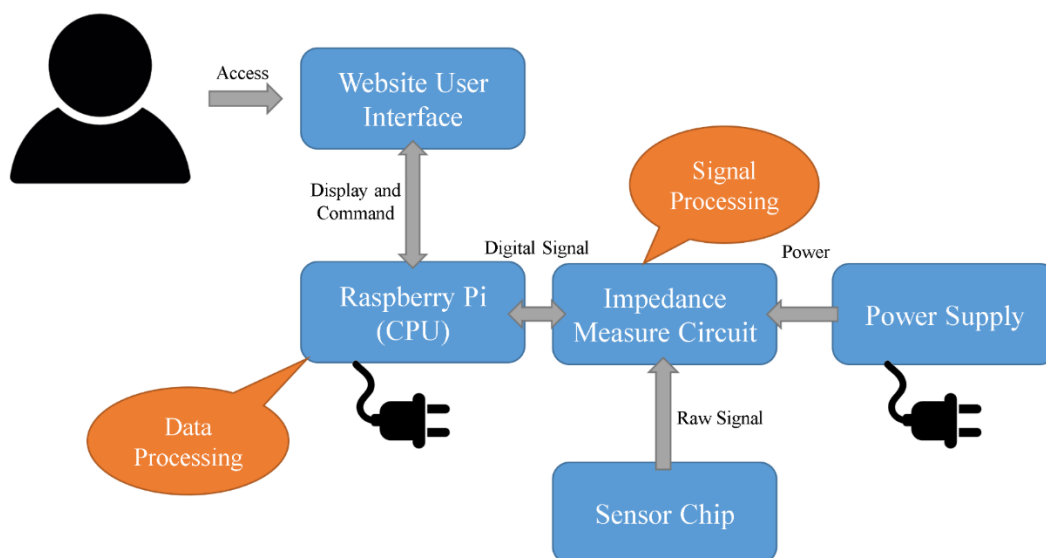signals and information from the web server obtained from and given to the user.

Figure S13 General scheme for real-time impedimetric detection system (Z_GENβ)

153

S.8.2.2 Schematic Design

Apart from Z_GENα, which uses a function generator for production of sinusoidal voltage waves, a power supply to give stable voltage, a commercially developed DAQ device for acquiring signal and its software for data processing, Z_GENβ needs to realize all that matter and integrate them into a miniaturized device. The schematic for circuitry is shown, which is rather more complex than that of Z_GENα.
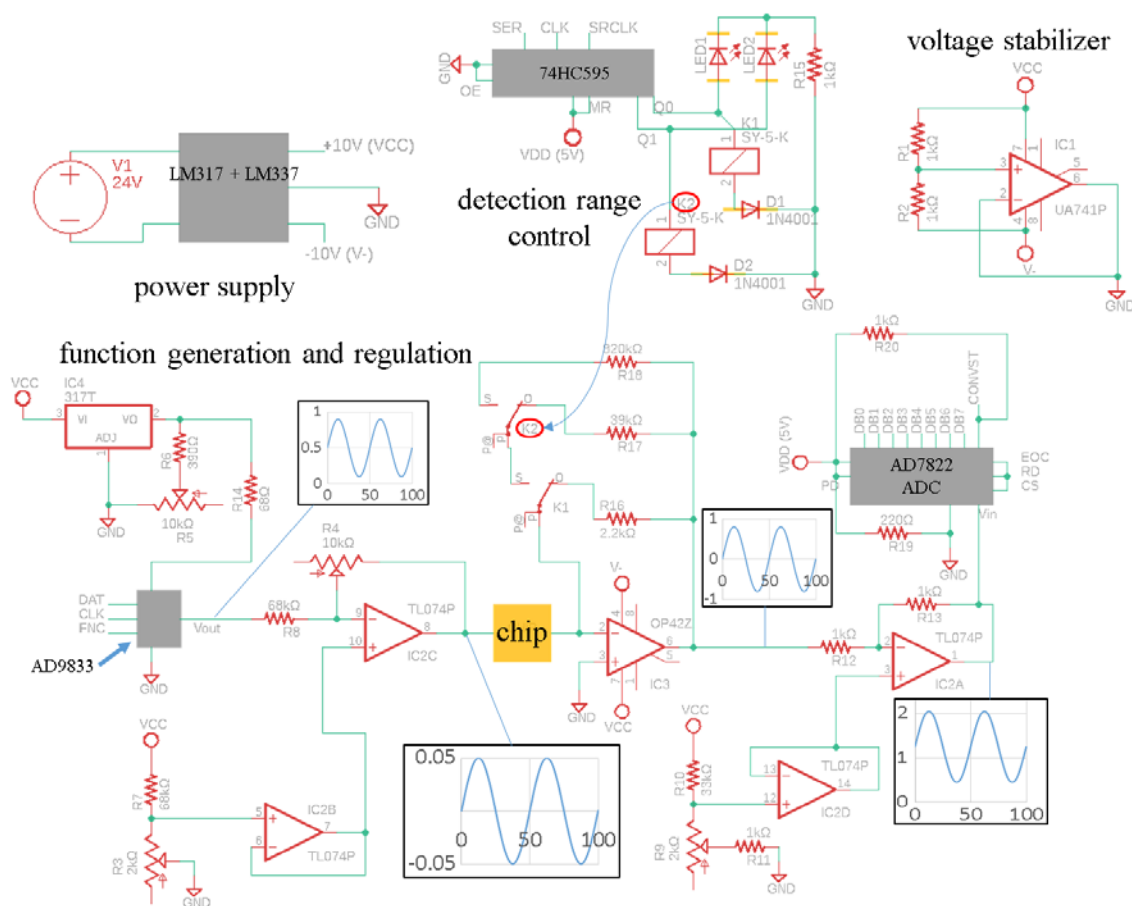

Figure S14 Circuit schematic for Z_GENβ.

S.8.2.3 Data Processing

The raw signal obtained by the ADC is an 8-bit resolution data ranging from 0 to 255 at a rate of 1MS/s (mega samples per second). Due to the relatively fast sampling speed by raspberry Pi and some unknown imperfections within the circuitry, there may appear to be some defects or noisy signal in the acquired data. Thus, a strategy for data processing before the calculation of |Z| and phase of the measured system is designed. The general concept is depicted for raw signals with a linearly transformed value between 0 and 1.
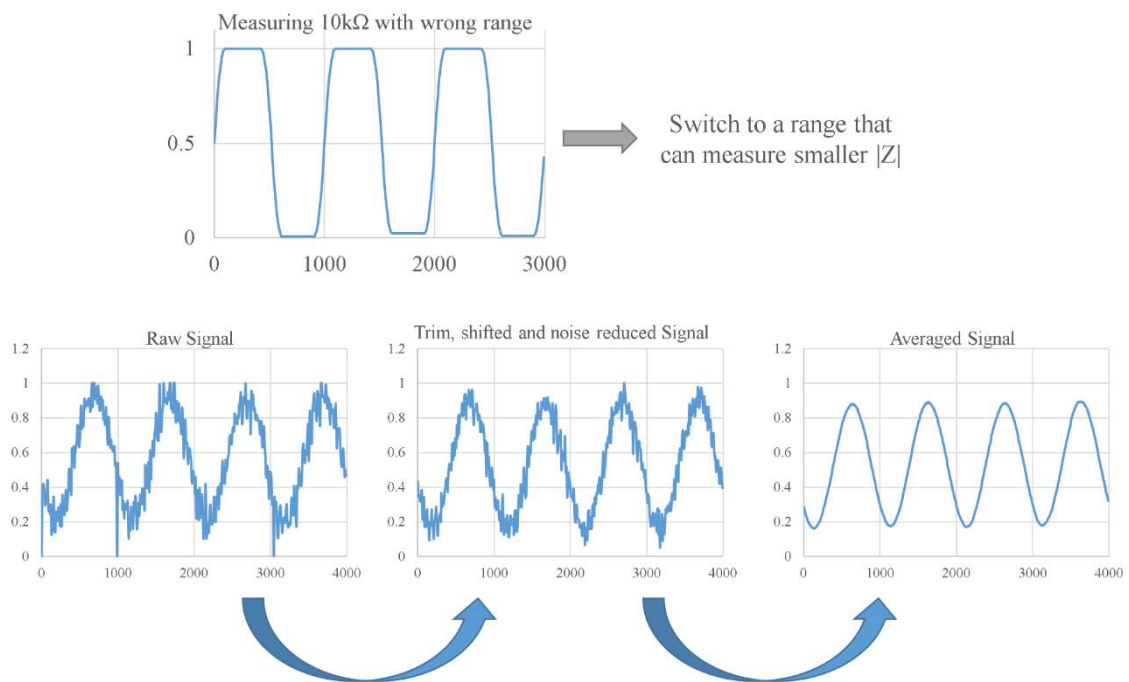
Figure S15 Strategy for impedance range detection and data processing (Z_GENβ).

First, leading and ending consecutive zeros are trimmed and the data is shifted to a start of a non-zero value. Second, values outside n standard deviations from the average of m data points are removed where n and m are arbitrarily defined constants for a specific sampling frequency. Third, the removed values are linearly bridged between non-removed values to form continuous data points. Fourth, smoothing is performed by averaging k data points to form a new value. At last, |Z| is found by calculating the standard deviation of the overall data which equals the zero-mean RMS of the signal and is proportional to the amplitude with a relationship of $\sqrt{2}\times$RMS=Amp (Bissell and Chapman, 1992) and the phase is obtained by first calculating the average of the remainder of the time (μs) of a data point, which is larger than or equals the mean and its previous data point is smaller than the mean, divided by the number of data points within a repeating sine wave cycle, then linearly transforming it to a value between 0 and 360 degrees.

156

S.8.2.4 Website Server

For portable devices dedicated to point-of-care applications, a relatively
miniaturized device compared with an instrument must be set up that contains user-
friendly interfaces and well-designed data display graphics. A smart phone might come
in handy when it comes to the such integration. Applications using smart phone for
electrochemical on-chip detection of biomarkers are presented and published every year
(Jiang et al., 2014; Zhang et al., 2015; D. Zhang et al., 2016). For the above reasons, a
website platform for the user interface of generation β is set as a target for its improvement
compared with generation α, which can be accessed using local networking on either a
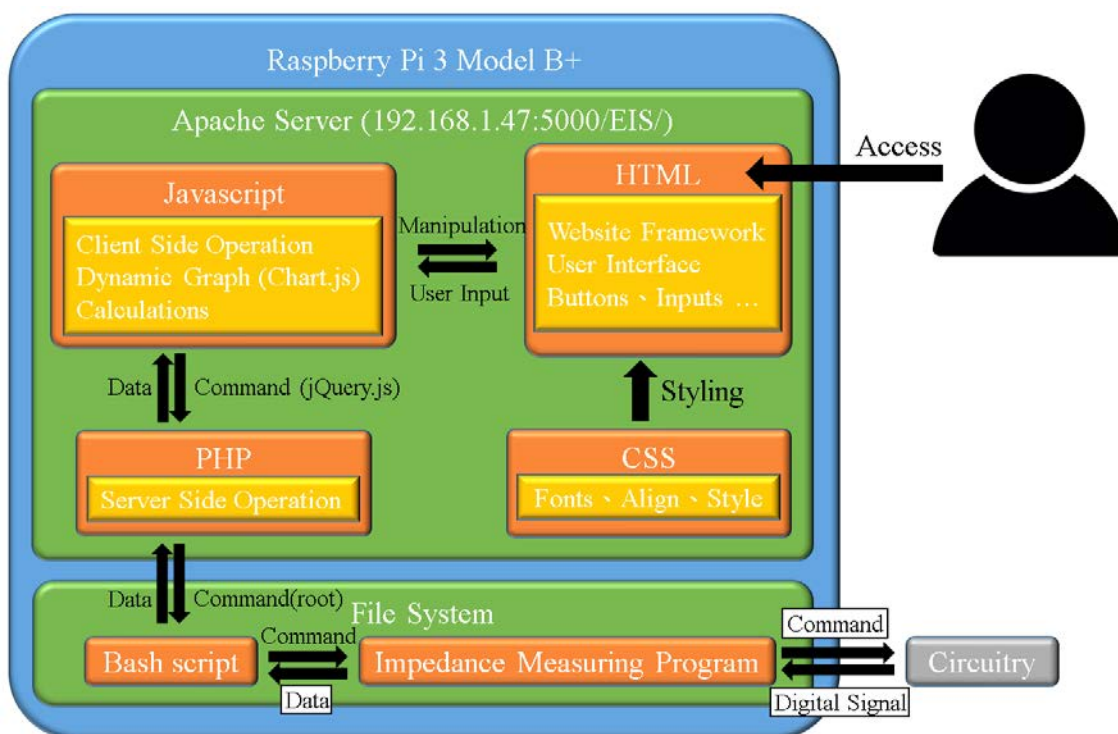personal computer, a smart phone, a pad … etc. The overall structure is shown.

Figure S16 Structure of web server with user, circuitry and inter communication (Z_GENβ).

157

S.8.3 Preliminary Results for Z_GENβ

S.8.3.1 Fabrication and Setup Results

The photograph of Z_GENβ is shown in Figure S17. The dimension is $22(L)\times10(W)\times6(H)$ cm^3, making the whole system portable. The raspberry Pi controls the circuitry by sending voltage signals towards several IC chips. The sinusoidal current passes through the connected chip and is amplified by an operational amplifier (OP42). The signal is then linearly transformed into a range which the analog-digital converter (ADC) can sample. The transformed digital values are read by the raspberry Pi and being processed. At last, impedance values are plotted on the website.
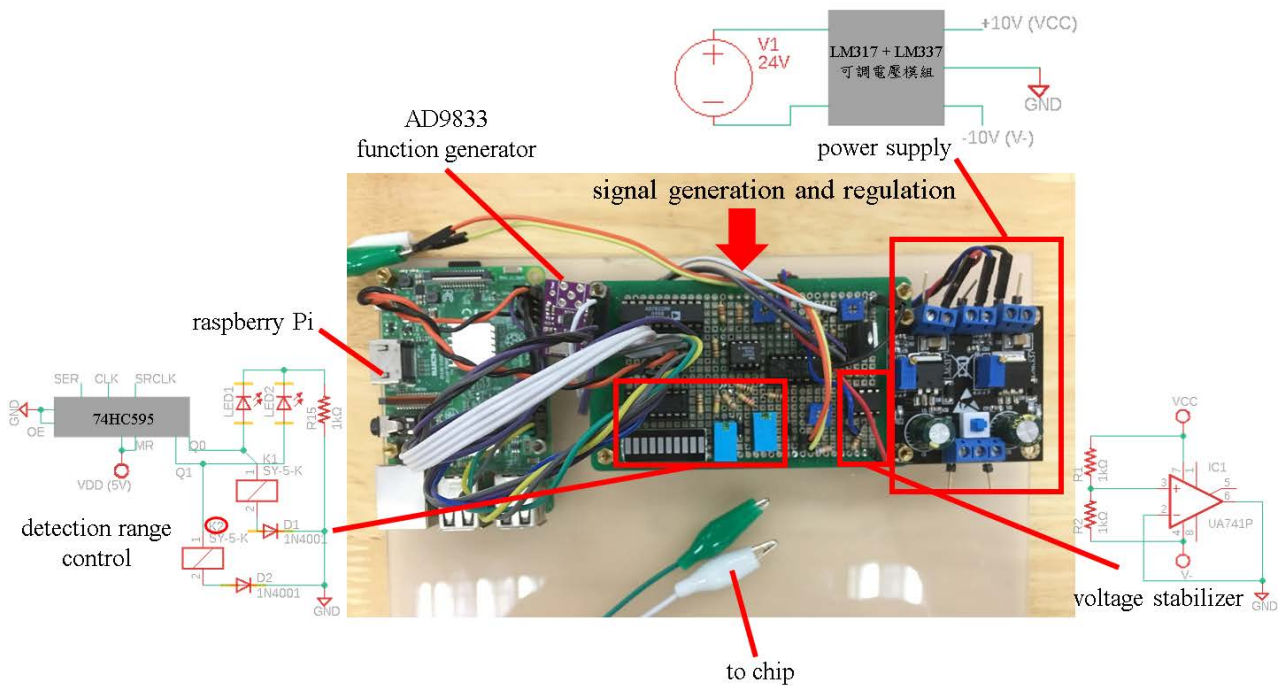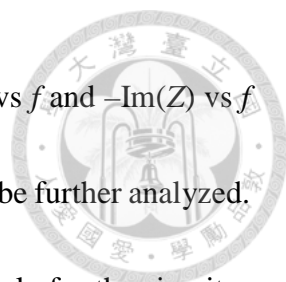

Figure S17 Photograph of Z_GENβ impedance detection system.

The website shows |Z| vs *f*, phase vs *f*, Im(Z) vs Re(Z), Re(Z) vs *f* and –Im(Z) vs *f* at the same time. The data collected can be saved to a csv file and can be further analyzed. A mobile power supply can be simultaneously used as the power supply for the circuitry and raspberry Pi, and smartphone-controlled impedance detection can also be achieved.
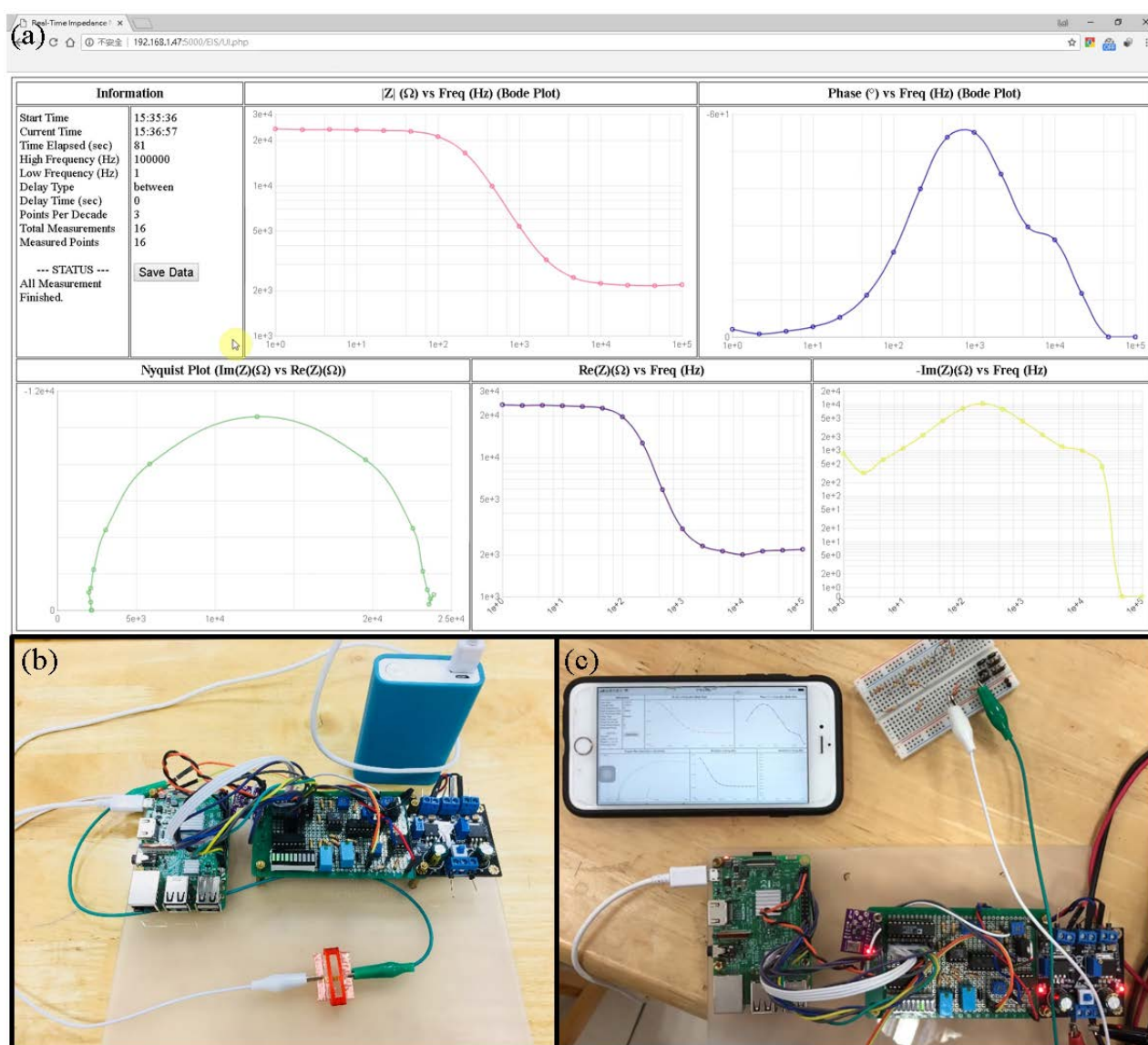

Figure S18 (a) Screenshot of the user interface website, (b) Z_GENβ powered by a mobile power supply, and (c) smartphone controlled Z_GENβ system.

159

S.8.3.2 Microfluidic Impedimetric Detection of Bare IDA Electrodes

The repeatability of EIS detection in a microfluidic integrated IDA chip system is

tested using Z_GENβ as the measuring device. In Figure S19, it can be seen that a fairly

stable measurement of |Z| can be achieved within a frequency range of $1 \sim 10^5$Hz and an

absolute impedance range of about $0.1 \sim 30$kΩ. However, at high frequencies, the phase

angle does not have a reasonable and repeatable value. This reason is due to the larger

noise of sampling values at high frequencies. A red line is drawn at 90° on the phase vs f

plot. Normally, phase angles wouldn't exceed this value because that would give rise to

a negative Re(Z), and does not correspond to any familiar electrochemical mechanism.

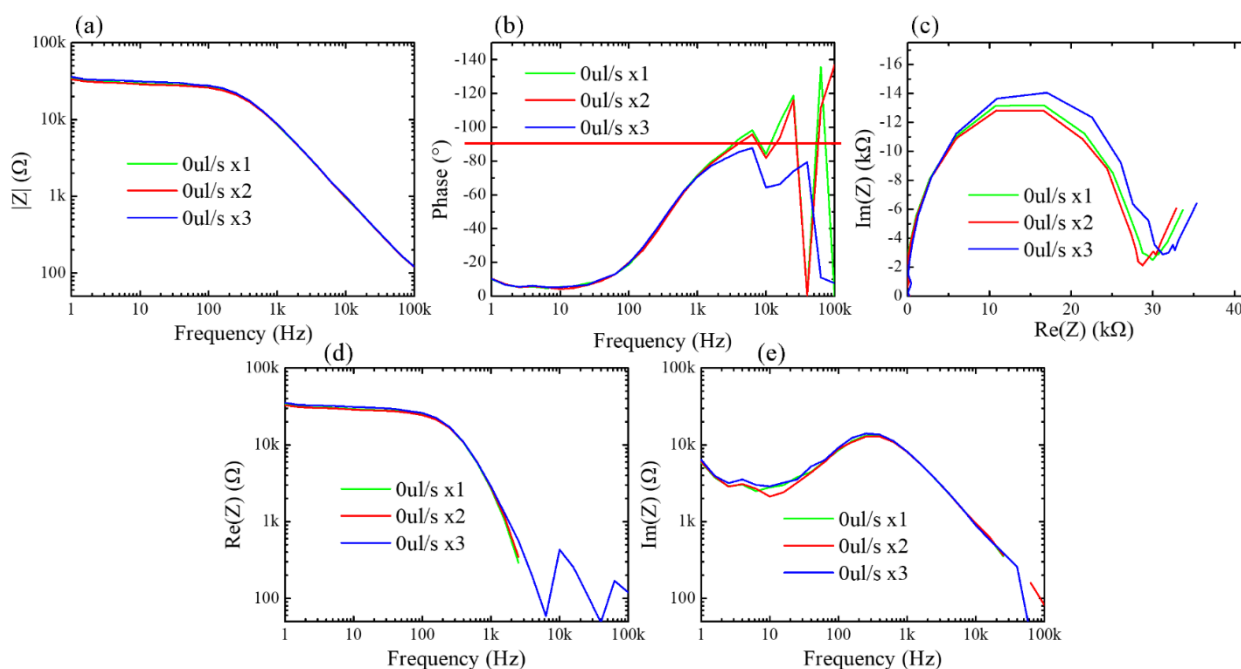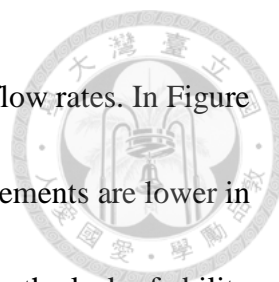Such sampling errors and data processing are needed to be improved.

Figure S19 (a) |Z| vs f, (b) phase vs f, (c) Im(Z) vs Re(Z), (d) Re(Z) vs f and (e) Im(Z) vs f
for single EIS detection of IDA chip at 0μL/s flow speed using Z_GENβ. The channel
width is 0.5mm. $V_{amp} = 50$mV. Running buffer: PBS + 5mM Fe(CN)$_6^{3-/4-}$.

160

The repeatability of measurements is also verified at different flow rates. In Figure S20, one can see that at higher flow rates, the repeatability of measurements are lower in a qualitative manner. The author presumes that the reason arises from the lack of ability for current stabilizing of Z_GENβ.
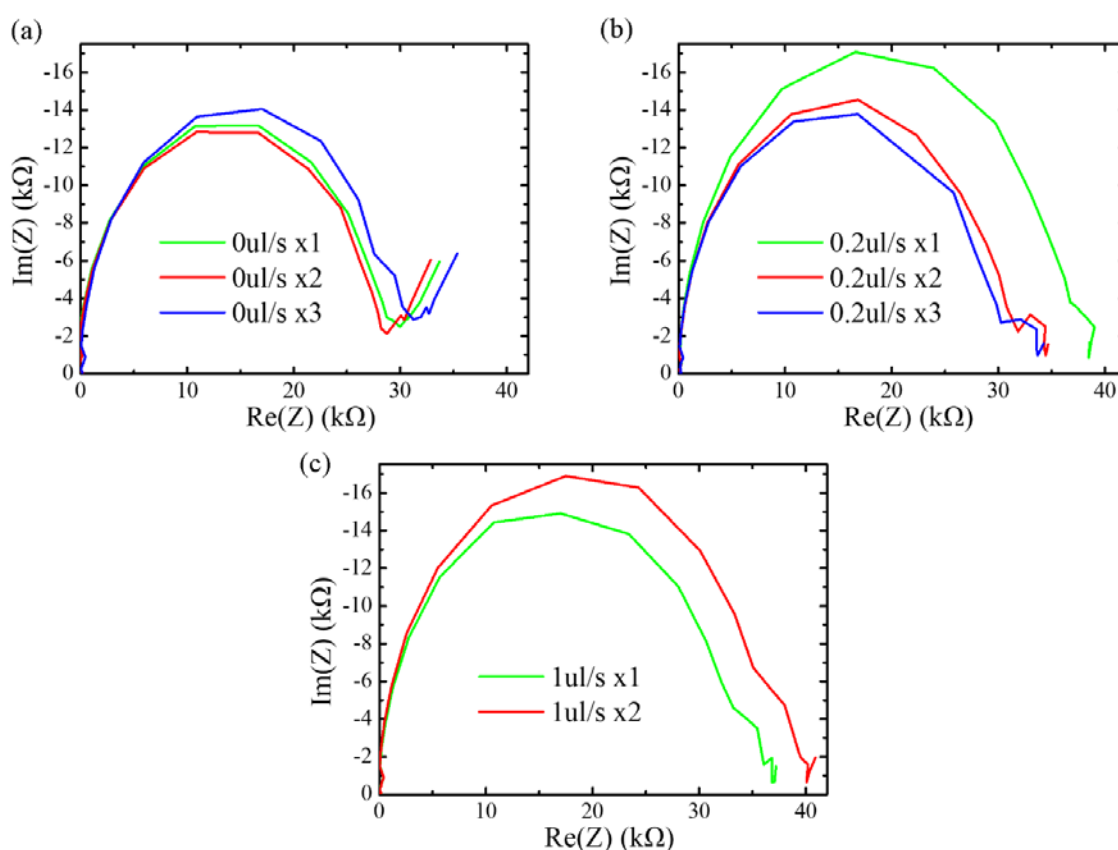

Figure S20 Nyquist plots of impedance detections using Z_GENβ at (a) 0μL/s, (b) 0.2μL/s and (c) 1μL/s. The numbers after x in the legend indicate the sequential order of detection.